ISSN: 0000-0000 (Online)
VOLUME 1, ISSUE 1, 2026

Journal of
Surface Engineering and Coating Technology

www.jsect.kz

ISSN 0000-0000 (Online)

Journal of
Surface Engineering and Coating Technology

2026

Volume 1 · Issue 1

PlasmaScience LLP
Ust-Kamenogorsk, 2026

Postal address: Gogol Street 7G., 070018, Ust-Kamenogorsk, Kazakhstan
E-mail: editir@jsect.net
Web-site: https://jsect.kz/

Journal of Surface Engineering and Coating Technology – 2025. – Vol. 1, Iss. 1 – 74 p. – ISSN xxxx-xxxx (Online).
Proprietary: PlasmaScience LLP.
Registered with the Ministry of Information and Social Development of the Republic of Kazakhstan. Certificate of re-registration No. KZ64VPY00112270 dated 13.02.2025.

CONTENTS

ORIGINAL STUDY

STUDY OF THE EFFECT OF PRELIMINARY ULTRASONIC SURFACE MODIFICATION OF TI-6AL-4V ALLOY SUBSTRATE ON THE FORMATION OF A NITRIDED LAYER

Aringozhina Z[1], Magazov N[1], Amanov A[2], Askhatov A[1], Batanov E[1]

[1] D. Serikbayev East Kazakhstan Technical University, 69 Protozanov Street, Ust-Kamenogorsk, Kazakhstan;
[2] Faculty of Engineering and Natural Sciences, Tampere University, FIN-33014 Tampere, Finland
*Corresponding author: zaringozhina@edu.ektu.kz

Abstract. *This study examined how ultrasonic nanocrystalline surface modification (UNSM) influences the formation of nitride layers in Ti-6Al-4V alloy during ion-plasma nitriding (IPN). We systematically varied UNSM parameters-specifically vibration amplitude, static load, and processing temperature-to assess their impact on the material's microstructure, hardness, elastic modulus, and tribological behavior. Our findings indicate that an optimized UNSM pre-treatment significantly boosts nitrogen diffusion, resulting in the creation of dense and uniform* TiN/Ti_2N *layers. Notably, samples subjected to UNSM under high-load and elevated-temperature conditions showed the most substantial improvements. These included a surface hardness increase of up to 25%, an elastic modulus rise of up to 18%, and enhanced wear resistance with a more stable and reduced friction coefficient (around 0.55). Further scanning electron microscopy (SEM) and X-ray diffraction (XRD) analyses corroborated these results by confirming microstructural densification, grain refinement, and a heightened intensity of nitride phases. These findings underscore the scientific value and practical applicability of UNSM as an effective surface activation method. Consequently, the hybrid UNSM + IPN approach emerges as a promising strategy for prolonging the service life of critical load-bearing components like biomedical implants and other engineering parts exposed to severe wear.*

Keywords: Ti-6Al-4V, elastic modulus, hardness, coefficient of friction, ion-plasma nitriding, UNSM.

1. Introduction

The push in contemporary materials science is towards innovative approaches for strengthening materials, particularly those vital for sectors like aerospace, medicine, and automotive [1]. Much effort is directed at surface modification techniques designed to boost critical material properties, including wear resistance, hardness, and corrosion resistance. While Ti-6Al-4V titanium alloy is a top choice for structural applications due to its remarkable specific strength, light weight, biocompatibility, and environmental resilience [2], its relatively soft surface remains a challenge, hindering its performance in high-friction and wear environments [3]. Overcoming these limitations often involves surface engineering. A popular approach, ion-plasma nitriding (IPN), improves surface characteristics by forming hard titanium nitrides (TiN, Ti_2N), which significantly boost hardness (up to 2000 HV), chemical stability, and resistance to wear and corrosion [4,5]. Despite these benefits, achieving deep, uniform nitrided layers remains challenging due to the inherent passive oxide film, low surface defect density, and slow nitrogen diffusion in titanium alloys [6]. These factors often lead to thin, brittle, or weakly adherent layers with compromised mechanical properties [7]. A promising strategy to enhance nitrogen uptake during nitriding is surface pre-activation. Among the most advanced methods is ultrasonic nanocrystalline surface modification (UNSM), which generates a nanostructured surface with high dislocation density and refined grains via high-frequency mechanical impacts [8,9]. This surface architecture facilitates nitrogen diffusion, leading to thicker, more uniform nitrided layers during subsequent ion-plasma nitriding (IPN) [10]. Additionally, UNSM improves layer adhesion and reduces the risk of in-service delamination or cracking. Despite recognizing the benefits of combining UNSM and IPN, existing

---

Received 2 August 2025; revised 17 December 2025; accepted 5 January 2026.

(https:doi.org/……)

literature lacks a systematic analysis of how UNSM parameters (vibration amplitude, static load, processing temperature) affect the nitrided layer's structural evolution, phase composition, and tribomechanical performance. Conventional surface treatments like shot peening, PVD coatings, and laser shock peening offer limited control over surface grain structure modification or activation of chemical diffusion [11–13]. Unlike these methods, UNSM allows for precise parameter control and produces a dense, defect-rich surface that works synergistically with nitrogen plasma during IPN, leading to enhanced final performance. Despite the recognized benefits of combining Ultrasonic Nanocrystalline Surface Modification (UNSM) and Ion-Plasma Nitriding (IPN), current literature lacks systematic studies on how specific UNSM parameters - such as vibration amplitude, static load, and processing temperature - affect the structural evolution, phase composition, and tribomechanical performance of the nitrided layer. Traditional surface treatment methods, including shot peening, PVD coatings, and laser shock peening, show limited capabilities in modifying the surface grain structure or activating chemical diffusion [11–13]. In contrast, UNSM provides precise parameter control and creates a dense, defect-rich surface that synergistically interacts with nitrogen plasma during IPN, leading to improved final performance.

2. Materials and methods

In this work, we aim to investigate how pre-treatment with ultrasonic nanocrystalline surface modification (UNSM) impacts the formation and characteristics of a nitrided layer on Ti-6Al-4V alloy during ion-plasma nitriding. Our primary focus will be a detailed analysis of the layer's microstructure and tribo-mechanical properties, including its hardness, elastic modulus, and wear resistance. During the UNSM process, we adjusted key parameters: amplitude, static load, and temperature (refer to Table 1 for specifics). These settings were chosen based on our earlier research [14], which showed they effectively refine the grain structure and boost both the microhardness and elastic modulus of the Ti-6Al-4V alloy. After UNSM, the specimens naturally cooled to room temperature. The UNSM-treated surfaces were then subjected to ion-plasma nitriding (IPN). The IPN process was carried out using a specialized laboratory setup (Model LDMC-20, Tianman Industrial Furnace). A schematic representation of the equipment is shown in Fig. 1. The treatment was performed at a temperature of 500 °C for 2 h. The pressure in the chamber was maintained at 400 Pa. A glow discharge was initiated between the anode (the vacuum chamber body) and the cathode (the metal specimen) upon application of voltage. This discharge ionizes nitrogen atoms by knocking out electrons, forming nitrogen ions. These ions bombard the metal surface and penetrate into it, leading to the formation of a nitride lattice (Fig. 2).

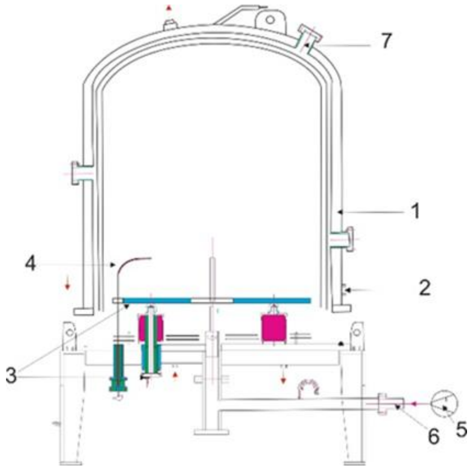

Fig. 1. Schematic diagram of the ion nitriding equipment: 1-vacuum chamber; 2-anode; 3-cathode (specimen holder); 4-vacuum chamber temperature sensor; 5-pumping system; 6-pressure relief plug; 7-vacuum viewing window.

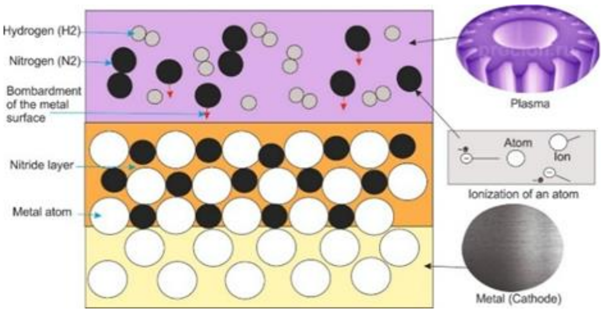

Fig. 2. The process of gas ion diffusion into the metal surface.

Table 1. Processing conditions for Ti-6Al-4V alloy specimens.

Samples	Sample Designation	Processing Conditions
S0	initial	initial
S1	UNSM-only	UNSM (20 μm,30 N, RT)
S2	UNSM-only	UNSM (30 μm,30 N, RT)
S3	UNSM-only	UNSM (30 μm,50 N, 400 °C)
S4	UNSM-only	UNSM (30 μm,60 N, 400 °C)
S0N	nitrided	nitrided
S1N	Combined	S1+ nitrided
S2N	Combined	S2+ nitrided
S3N	Combined	S3+ nitrided
S4N	Combined	S4+ nitrided

To evaluate the tribo-mechanical characteristics of the specimens, their microhardness, elastic modulus, and tribological properties were investigated. Hardness measurements were performed using a Vickers indenter on a FISCHERSCOPE HM2000S device (Sindelfingen, Germany). The indenter was a four-sided diamond pyramid with an angle of 136° between the opposite faces. Hardness was determined according to the Vickers scale (HV). The elastic modulus was calculated using the instrumented indentation method on the same device. All measurements were conducted according to the Vickers scale (HV), and each test was repeated five times to ensure accuracy. Tribological properties were evaluated in accordance with the ASTM G99 standard using a TRB3 tribometer (Anton Paar GmbH, Graz, Austria). A ball-on-disc configuration was used, where a 6.00 mm diameter 100Cr6 steel ball served as the counter body. The tests were conducted in ambient air at a laboratory temperature of 21.33 °C and relative humidity of 31.05%. The sliding radius was 2.00 mm, and the linear sliding speed was set to 10.0 cm/s. A constant normal load of 2.00 N was applied, and data were recorded at an acquisition rate of 10 Hz. The total sliding distance was 300.00 m. The test was conducted in a single-pass mode without pause, with initial homing enabled and no unloading at the end. The Ti-6Al-4V specimens were used as substrates without additional cleaning prior to testing. The phase composition was analyzed using an X'Pert Pro X-ray diffractometer (Panalytical, Amsterdam, Netherlands) with Cu-Kα radiation, operating at 40 kV and 30 mA. The scanning parameters were set to $35° < 2θ < 85°$, with a step size of 0.02° and an exposure time of 5 s. The microstructure of the specimens was analyzed using a scanning electron microscope (TESCAN Vega, Tescan, Brno, Czech Republic). Prior to examination, cross-sectional samples were prepared through a series of standard metallographic procedures. First, the specimens were mechanically sectioned using silicon carbide cutting wheels. After sectioning, the surfaces were sequentially ground and polished using diamond paste to achieve a flat and deformation-free finish. To reveal the microstructural features, the polished samples were chemically etched for 10 s using Kroll's reagent, which consists of 100 mL distilled water, 1-3 mL hydrofluoric acid, and 2-3 mL nitric acid.

3. Results and discussion

3.1. Tribology Evaluation Results

Based on the analysis of the coefficient of friction (Fig. 3) and the wear surface morphology (Fig. 4), it was established that the parameters of UNSM significantly affect the tribological performance of the nitrided Ti-6Al-4V alloy. All samples exhibited two distinct stages: a running-in phase, during which the coefficient of friction (μ) increased rapidly, followed by a steady-state phase with stabilized friction behavior. The S4N sample (amplitude of 30 μm, load of 60 N, temperature of 400 °C) showed the lowest and most stable friction coefficient (~0.55) after a short running-in period (~40 m). SEM analysis revealed a uniform and dense wear track with minimal signs of plastic deformation, indicating high wear resistance and the presence of a protective nitride layer. The dominant wear mechanism is identified as mild abrasive wear. The S3N sample exhibited a slightly longer running-in phase and a steady-state of ~0.60-0.65. SEM images showed localized craters, micro-scratches, and indications of fatigue wear. Although the nitride layer was formed, its local heterogeneity led to selective degradation during prolonged contact. The S2N and S1N samples, treated at room temperature, displayed less stable friction behavior and a prolonged running-in period. Their coefficients of friction reached up to ~0.75 and exhibited fluctuations. SEM images revealed pronounced grooves, microcracks, and delamination zones. The prevailing wear mechanisms in these samples were abrasive and delamination wear, resulting from weak adhesion and insufficient depth of the nitrided layer. The S0N reference sample, without UNSM treatment, exhibited the most unstable friction behavior. After a short running-in phase, the coefficient of friction rapidly rose to ~0.80 and showed sharp fluctuations. SEM analysis indicated severe surface degradation, including plastic deformation and material detachment, consistent with intensive adhesive wear due to the lack of a reinforced surface layer. In summary, pre-treatment UNSM with optimized parameters enhances the formation of a dense and uniform nitrided layer, significantly improving wear resistance and stabilizing the frictional response. The S4N mode, in particular, proved to be the most effective, delivering superior tribological performance due to the combined effect of high amplitude, load, and temperature. In comparison to laser shock-peened and PVD-coated Ti-6Al-4V alloys, which typically exhibit coefficients of friction in the range of 0.65-0.80 under similar dry sliding conditions, our samples achieved more stable friction behavior and lower steady-state values (e.g., 0.55 for S4N), highlighting the tribological advantage of the combined UNSM and IPN approach [15].

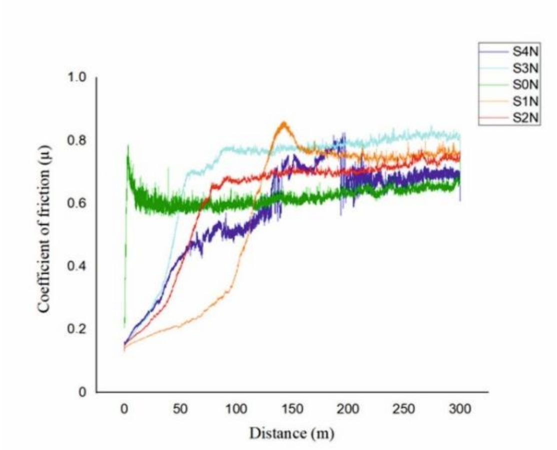

Fig. 3. Results of tribological tests under various UNSM treatment parameters after nitriding.

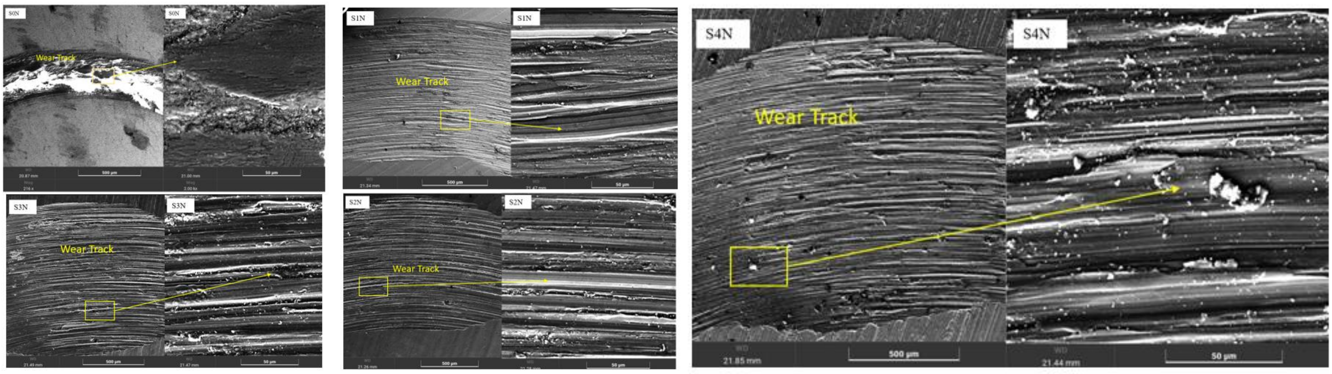

Fig. 4. SEM images of the wear surfaces of Ti-6Al-4V specimens after combined treatment by UNSM and nitriding.

3.2. X-Ray Phase Analysis

Fig. 5 presents the XRD patterns of Ti-6Al-4V specimens subjected to ion-plasma nitriding after UNSM treatment with varying parameters, as well as a reference sample S0N that was nitrided without prior ultrasonic treatment. In the S0N sample, prominent peaks of the α-Ti matrix dominate the pattern, accompanied by weak reflections corresponding to the $AlTi_3N$ and Ti_2N phases, indicating a relatively thin and less developed nitride layer. In contrast, the S1N sample (processed with minimum UNSM parameters) also shows dominant α-Ti peaks and only minor TiN signals, confirming limited nitrogen diffusion. The S2N pattern demonstrates a slight increase in the TiN peak intensity due to enhanced plastic deformation; however, the formation of the nitride layer remains insufficient without applying an elevated temperature. A significant increase in TiN peak intensity is observed in the S3N sample, alongside broader peaks that indicate a denser and more refined nitride layer. This result is attributed to the higher static load and processing temperature during UNSM. The S4N sample exhibits the highest intensity and sharpness of TiN and Ti_2N peaks, suggesting the formation of a thick, uniform, and nanocrystalline nitride layer. These findings confirm that pre-treatment by UNSM plays a crucial role in promoting phase transformations during nitriding. The combination of higher mechanical impact and thermal energy during UNSM, particularly in the S4N mode, provides optimal conditions for the TiN phase formation, as also supported by previous studies [9]. Thus, the XRD results confirm that preliminary ultrasonic surface modification plays a decisive role in phase transformations during ion-plasma nitriding, providing favorable conditions for the intensive formation of TiN phases. The most pronounced effect is achieved when high temperature and static load are combined during the UNSM process, as demonstrated in the S4N mode.

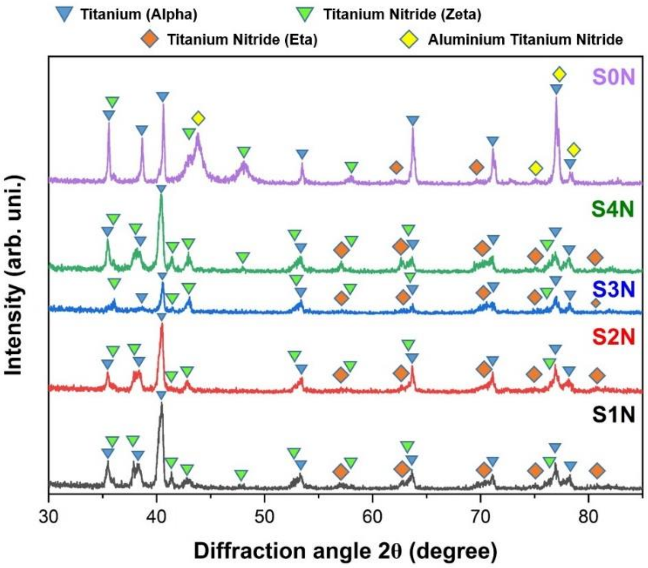

Fig. 5. X-ray diffraction (XRD) patterns of Ti-6Al-4V alloy after IPN with various UNSM treatment parameters.

3.3. Hardness

The parameters of the ion-plasma nitriding process were selected based on experimental data, which showed that the maximum surface microhardness of the Ti-6Al-4V alloy was achieved at a temperature of 500 °C and a duration of 2 h (Fig. 6). When the treatment time was increased to 3 h, a decrease in hardness was observed, which was likely associated with grain coarsening, possible recrystallization, relaxation of internal stresses, the formation of defects (such as cracks and delamination), and the homogenization of the nitrogen concentration gradient due to extended diffusion saturation. Similar effects were reported by Minoru Umemoto [13], where excessive nitriding time resulted in a reduction in hardness due to grain growth and the release of residual stresses. Therefore, the temperature of 500 °C provides active nitrogen diffusion without structural degradation of the material, making it optimal for the treatment of the Ti-6Al-4V alloy. The results presented in Fig. 7 clearly demonstrate the pronounced effect of the combination of UNSM and subsequent nitriding on the enhancement of surface hardness. Specifically, the combined treatment under the S1N regime resulted in more than a 25% increase in microhardness compared to the specimen subjected to nitriding alone (S0N). This indicates that preliminary UNSM treatment facilitates the active diffusion of nitrogen atoms into the material and the formation of hard nitride phases [20]. Such an enhancement is consistent with the findings of Sun et al. [21] and Mogucheva [22], which emphasize the significant role of prior plastic deformation in improving the conditions for nitrogen diffusion and the formation of the nitride layer. The S2N specimen, processed under similar conditions but with an increased amplitude (30 µm), exhibited a 17% increase in microhardness, further confirming the effectiveness of more intense surface deformation. In the S3N regime, at a temperature of 400 °C, the microhardness increased by 23%, confirming the activation of nitrogen diffusion processes due to enhanced atomic mobility. This effect has been reported in several studies, which have also emphasized the role of thermal activation in increasing the thickness and density of the nitride layer [23]. The least pronounced effect was observed for the S4N specimen, where UNSM was performed at 400 °C with a load of 60 N. The increase in microhardness was only 9.6%, which may be attributed to partial recrystallization, a reduction in defect density, or local overheating that diminished the plastic deformation effect [13].

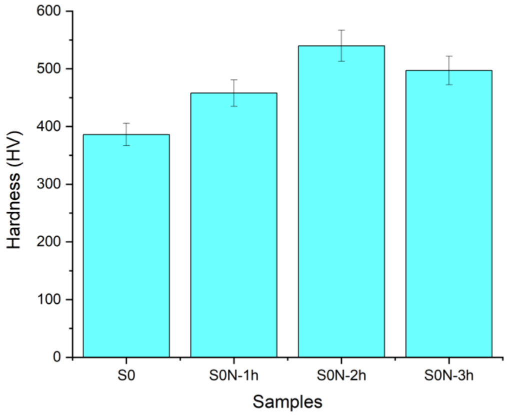

Fig. 6. Variation in the hardness of Ti-6Al-4V specimens at 500 °C with different nitriding durations.

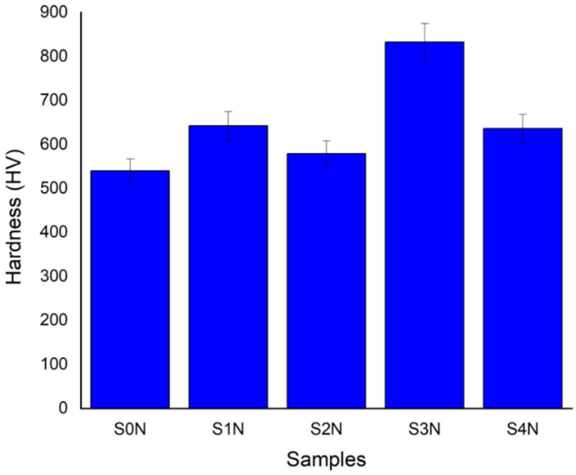

Fig. 7. Effect of different UNSM regimes on the hardness of Ti-6Al-4V alloy after nitriding.

The greatest improvement in microhardness (over 25%) was achieved under moderate UNSM conditions (amplitude of 20 µm, load of 30 N, RT), which provided an optimal degree of plastic deformation that enhanced nitrogen diffusion. Although increasing the UNSM temperature combined with high loads may further activate diffusion processes, in some cases it leads to reduced hardening efficiency, likely due to recrystallization or the partial relaxation of internal stresses [13,23]. Preliminary UNSM treatment prior to nitriding contributes to an increase in both the elastic modulus and microhardness due to the activation of diffusion processes and the formation of a nanostructured subsurface layer. Repeated high-frequency impacts induce intense plastic deformation, increase dislocation density, and generate crystal lattice defects (dislocations, sub-boundaries, vacancies), which create internal resistance to deformation and thus enhance resistance to elastic strain. This phenomenon, known as dislocation hardening, effectively increases the apparent elastic modulus during surface-sensitive localized measurements [17]. In addition, the presence of a greater number of high-angle grain boundaries and the formation of nanostructures further restrict atomic movement, contributing to localized stiffness enhancement [24]. The experimental results obtained in this study confirm this effect. As shown in Fig. 8, the maximum values of microhardness and elastic modulus were achieved under UNSM parameters that provided controlled plastic deformation without overloading the surface (amplitude of 20 µm, load of 30 N, RT). Such treatment promotes a uniform distribution of residual stresses and the formation of a structurally active surface favorable for nitride phase formation during subsequent ion nitriding. Thus, a clear correlation was established between the parameters of the preliminary treatment and the mechanical properties of the modified layer, enabling the targeted design of surface structure and properties for the development of wear-resistant functional coatings [25]. The microhardness values obtained in this study (e.g., up to 25% increase after UNSM + IPN treatment) demonstrate a noticeable improvement compared to those reported for Ti-6Al-4V alloys treated using conventional PVD, plasma ion implantation, and laser nitriding methods, where hardness enhancement typically ranges from 10% to 15% [22]. This suggests that the pre-treatment by UNSM significantly enhances nitrogen diffusion and contributes to the formation of a more hardened surface layer.

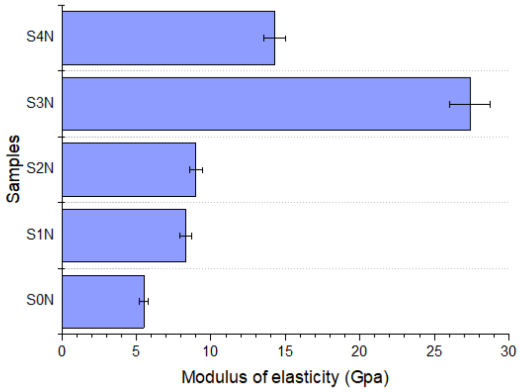

Fig. 8. Elastic modulus of Ti-6Al-4V specimens under different UNSM treatment parameters after nitriding.

4. Conclusion

UNSM pre-treatment boosts microhardness by up to 25% and the elastic modulus by 18% compared to samples without this initial activation. Moreover, UNSM improves the tribological performance of the nitrided layer. The most favorable outcomes were observed in samples treated at an amplitude (A) of 30 µm, a static load (F) of 60 N, and a temperature (T) of 400 °C, which exhibited a stable coefficient of friction of approximately 0.55. SEM and XRD analyses confirmed that UNSM promotes the formation of a more uniform and dense nitride layer. This indicates that UNSM is an effective method for enhancing both the structural integrity and functional performance of nitrided layers on Ti-6Al-4V alloy. Given the improved surface hardness, refined microstructure, and enhanced wear resistance, UNSM-treated Ti-6Al-4V alloy is poised for use in advanced industries. This includes biomedical engineering (e.g., hip implants, dental screws), aerospace systems, and precision mechanical components that face high contact stresses and corrosive environments.

Funding

This research was funded by the Committee of Science of the Ministry of Science and Higher Education of the Republic of Kazakhstan (Grant No. AP19680457).

Conflict of interest

The authors declare that they have no competing interests.

References

1 Peters M. (2003) Titanium Alloys for Aerospace Applications. *Advanced Engineering Materials*. 5(6), 419-427. https://doi.org/10.1002/adem.200310095

2 Geetha M., Singh A.K., Asokamani R., Gogia A.K. (2009) Ti Based Biomaterials, the Ultimate Choice for Orthopaedic Implants-A Review. *Progress in Materials Science.* 54(3), 397-425. https://doi.org/10.1016/j.pmatsci.2008.06.004

3 Niinomi M. (2008) Mechanical Biocompatibilities of Titanium Alloys for Biomedical Applications. *Journal of the Mechanical Behavior of Biomedical Materials.* 1(1), 30-42. https://doi.org/10.1016/j.jmbbm.2007.07.001

4 Zhang L., Shao M., Zhang Z., Yi X., Yan J., Zhou Z., Fang D., He Y., Li Y. (2023) Corrosion Behavior of Nitrided Layer of Ti6Al4V Titanium Alloy by Hollow Cathodic Plasma Source Nitriding. *Materials*. 16(8), 2961. https://doi.org/10.3390/ma16082961

5 She D., Yue W., Fu Z., Gu Y., Wang C., Liu J. (2013) The Effect of Nitriding Temperature on Hardness and Microstructure of Die Steel Pre-Treated by Ultrasonic Cold Forging Technology. *Materials & Design*. 49, 392-399. https://doi.org/10.1016/j.matdes.2013.01.003

6 Samanta A., Bhattacharya M., Ratha I., Chakraborty H., Datta S., Ghosh J., Bysakh S., Sreemany M., Rane R., Joseph A. (2018) Nano- and Micro-Tribological Behaviours of Plasma Nitrided Ti6Al4V Alloys. *Journal of the Mechanical Behavior of Biomedical Materials.* 77, 267-294. https://doi.org/10.1016/j.jmbbm.2017.09.013

7 Farè S., Lecis N., Vedani M., Silipigni A., Favoino P. (2012) Properties of Nitrided Layers Formed during Plasma Nitriding of Commercially Pure Ti and Ti–6Al–4V Alloy. *Surface and Coatings Technology*. 206(8-9), 2287-2292. https://doi.org/10.1016/j.surfcoat.2011.10.006

8 Wang N., Zhu J., Liu B., Zhang X., Zhang J., Tu S. (2021) Influence of Ultrasonic Surface Rolling Process and Shot Peening on Fretting Fatigue Performance of Ti-6Al-4V. *Chinese Journal of Mechanical Engineering*. 34(1), 90. https://doi.org/10.1186/s10033-021-00611-1

9 Amanov A., Karimbaev R., Li C., Wahab M.A. (2023) Effect of Surface Modification Technology on Mechanical Properties and Dry Fretting Wear Behavior of Inconel 718 Alloy Fabricated by Laser Powder-Based Direct Energy Deposition. *Surface and Coatings Technology*. 454, 129175. https://doi.org/10.1016/j.surfcoat.2022.129175

10 Ozturk M., Husem F., Karademir I., Maleki E., Amanov A., Unal O. (2023) Fatigue Crack Growth Rate of AISI 4140 Low Alloy Steel Treated via Shot Peening and Plasma Nitriding. *Vacuum.* 207, 111552. https://doi.org/10.1016/j.vacuum.2022.111552

11 Wang T., Zhang X., Chen J., Li Z. (2019) The effect of ultrasonic nanocrystal surface modification on low temperature nitriding of ultra-high strength steel. *Journal of Materials Research and Technology*. 8(5), 4284-4291. https://doi.org/10.1016/j.jmrt.2019.07.042

12 Rahmani H., Rastegari S., Mirdamadi S. (2015) Effective Parameters on Microstructure and Properties of EB-PVD NiCrAlY Coating. *Surface Engineering.* 31(3), 156-165. https://doi.org/10.1179/1743294414Y.0000000371

13 Umemoto M. (2003) Nanocrystallization of Steels by Severe Plastic Deformation. Materials Transactions. 44(10), 1900-1911. https://doi.org/10.2320/MATERTRANS.44.1900

14 Smyslova M.K., Valiev R.R., Smyslov A.M., Modina I.M., Sitdikov V.D., Semenova I.P. (2021) Microstructural Features and Surface Hardening of Ultrafine-Grained Ti-6Al-4V Alloy through Plasma Electrolytic Polishing and Nitrogen Ion Implantation. *Metals.* 11(5), 696. https://doi.org/10.3390/met11050696

15 He Y., Zhang Z., Wei Z., Liu D., Zhao C., Zhang Y., Li Z. (2024) Laser Shock Peening: Fundamentals and Mechanisms of Metallic Material Wear Resistance Improvement. *Materials.* 17(4), 909. https://doi.org/10.3390/ma17040909

16 Liu Z., Ren S., Li T., Chen P., Hu L., Wu W., Li S., Liu H., Li R., Zhang Y. (2024) A Comparison Study on the Microstructure, Mechanical Features, and Tribological Characteristics of TiN Coatings on Ti6Al4V Using Different Deposition Techniques. *Coatings.* 14(2), 156. https://doi.org/10.3390/coatings14020156

17 Farokhzadeh K., Qian J., Edrisy A. (2014) Effect of SPD Surface Layer on Plasma Nitriding of Ti-6Al-4V Alloy. *Materials Science and Engineering*: A. 589, 199-208. https://doi.org/10.1016/j.msea.2013.09.077

18 Liu G., Leng K., He X., Tang L., Gao W., Fu Y. (2022) Microstructure Evolution of Ti-6Al-4V under Cold Rolling + Low Tem-perature Nitriding Process. *Progress in Natural Science: Materials International.* 32(4), 424-432. https://doi.org/10.1016/j.pnsc.2022.06.004

19 Zha X., Yuan Z., Qin H., Xi L., Guo Y., Xu Z., Dai X., Jiang F. (2024) Investigating the Dynamic Mechanical Properties and Strengthening Mechanisms of Ti-6Al-4V Alloy by Using the Ultrasonic Surface Rolling Process. *Materials.* 17(6), 1382. https://doi.org/10.3390/ma17061382

20 Aringozhina Z., Magazov N., Rakhadilov B., Uazyrkhanova G., Amanov A. (2025) Effect of Ultrasonic Nanocrystalline Surface Modification on Hardness and Elastic Modulus of Ti-6Al-4V Alloy. *AIMS Materials Science.* 12(1), 101-117. https://doi.org/10.3934/MATERSCI.2025008

21 Sun W., Song Z., Liu H., Wang J., Liu C., Si C. (2025) Effect of Surface Nanocrystallization Pretreatment on the Microstructure and Fretting Wear of Ti-6Al-4V Titanium Alloy Plasma Nitrided Layer. *Materials Characterization.* 223, 114884. https://doi.org/10.1016/j.matchar.2025.114884

22 Mogucheva A., Yuzbekova D., Lebedkina T., Lebyodkin M., Kaibyshev R. (2017) Influence of Severe Plastic Deformation on Mechanical Properties of an AA5024 Alloy. *Materials Science Forum*. 879, 1317-1322. https://doi.org/10.4028/www.scientific.net/MSF.879.1317

23 Vasylyev M.A., Chenakin S.P., Yatsenko L.F. (2012) Nitridation of Ti6Al4V Alloy under Ultrasonic Impact Treatment in Liquid Nitrogen. *Acta Materialia*. 60(18), 6223-6233. https://doi.org/10.1016/j.actamat.2012.08.006

24 Amanov A. (2021) Advancement of Tribological Properties of Ti–6Al–4V Alloy Fabricated by Selective Laser Melting. Tribology International. 155, 106806. https://doi.org/10.1016/j.triboint.2020.106806

25 Reshadi F., Faraji G., Baniassadi M., Tajeddini M. (2017) Surface Modification of Severe Plastically Deformed Ultrafine Grained Pure Titanium by Plasma Electrolytic Oxidation. *Surface and Coatings Technology.* 316, 113-121. https://doi.org/10.1016/j.surfcoat.2017.03.016

26 Ongtrakulkij G., Kajornchaiyakul J., Kondoh K., Khantachawana A. (2022) Investigation of Microstructure, Residual Stress, and Hardness of Ti-6Al-4V after Plasma Nitriding Process with Different Times and Temperatures. *Coatings.* 12(12), 1932. https://doi.org/10.3390/coatings12121932

27 Hsu H.-C., Lin Y.-C., Chen J.-X. (2023) Wear and Corrosion Performance of Ti-6Al-4V Alloy Arc-Coated TiN/CrN Nano-Multilayer Film. *Metals*. 13(5), 907. https://doi.org/10.3390/met13050907

AUTHORS' INFORMATION

Aringozhina Zarina Erzhanovna - PhD candidate is a Researcher at the Scientific Center "Protective and Functional Coatings" at the D. Serikbayev East Kazakhstan Technical University, Ust-Kamenogorsk, Kazakhstan; SCOPUS ID - 58639928600, ORCID iD 0009-0001-8428-4033 (e-mail: zaringozhina@edu.ektu.kz , +77054178929)

Magazov Nurtoleu Magzumbekovich - PhD candidate is a Researcher at the Scientific Center "Protective and Functional Coatings" at the D. Serikbayev East Kazakhstan Technical University, Ust-Kamenogorsk, Kazakhstan, SCOPUS ID - 57220041350, ORCID iD 0000-0002-9941-9199 (e-mail: magazovn@gmail.com, +77474263019)

Amanov Auezhan - PhD, associate Professor, Tribology of MaterialsFaculty of Engineering and Natural Sciences, Tampere University, FIN-33014 Tampere, Finland; SCOPUS ID - 36447543900, ORCID iD 0000-0002-8695-7430 (e-mail: auezhan.amanov@tuni.fi, +358504012367)

Askhatov Arnur Nurzhanovich - Technician of the Scientific Centre "Protective and Functional Coatings" at the D. Serikbayev East Kazakhstan Technical University, Ust-Kamenogorsk, Kazakhstan; (e-mail: ashatovarnur@gmail.com, +77477291103)

Batanov Elaman Yermekovich - Master's student, Junior researcher at the Scientific Center "Protective and Functional Coatings" at the D.Serikbaev East State Technical University, Ust-Kamenogorsk, Kazakhstan; (e-mail: batanovelman1234@gmail.com, +77087509436)

ORIGINAL STUDY

THE EFFECT OF LAYERING ON THE PROPERTIES OF METAL-CERAMIC COATINGS OBTAINED BY DETONATION SPRAYING

Aiym Nabioldina[1], Balym Alibekova[1], Garip Erdogan[2], Aibek Alibekov[1]

[1]Research Center “Surface Engineering and Tribology”, Sarsen Amanzholov East Kazakhstan University, Ust-Kamenogorsk, Kazakhstan
[2]Sakarya University, Metallurgical and Materials Eng. Dept. Materials Under Extreme Conditions Lab., Sakarya Turkiye
*Corresponding author: anabioldina@vku.edu.kz

Abstract. *This work presents the results of a study of multilayer metal-ceramic coatings based on the NiCr/NiCr-Al_2O_3/ Al_2O_3 system obtained by detonation spraying. Coatings with different numbers of layers were obtained: three-layer (NiCr, 50% NiCr - 50% Al_2O_3, Al_2O_3), five-layer (NiCr, 75% NiCr - 25% Al_2O_3, 50% NiCr - 50% Al_2O_3, 25% NiCr -75% Al_2O_3, Al_2O_3) and six-layer (NiCr, Al_2O_3, NiCr, Al_2O_3, NiCr, Al_2O_3). The study aims to establish the influence of layering and gradient distribution of components on the microstructural, phase, mechanical, and tribological characteristics of coatings. The microstructural features of the coatings were studied using scanning electron microscopy in backscattered electron (BSE) mode and energy dispersive spectral analysis (EDS). The phase composition was analyzed by X-ray phase analysis. Microhardness and surface roughness measurements were performed, as well as tribological tests at a temperature of 700 °C. It was found that five-layer coatings with a gradient structure with a gradual transition from a metal layer to a ceramic layer demonstrate the best performance characteristics among all the samples studied. The five-layer coatings were characterized by high microhardness, uniform surface roughness, minimal counterbody penetration depth, and a stable friction coefficient in wear tests.*

Keywords: multilayer coating, metal ceramics, NiCr/NiCr- Al_2O_3/ Al_2O_3, detonation spraying, gradient structure, microstructure, X-ray phase analysis, tribological properties.

1. Introduction

The development of high-temperature anti-friction materials with low friction coefficients and high wear resistance is one of the key tasks for modern mechanical engineering, energy, and aerospace industries [1-3]. When operating under high mechanical and thermal loads, it is necessary to create coatings that can maintain stable performance characteristics over a long period of time, protecting parts from wear and thermomechanical damage. Among the various classes of materials, metal-ceramic coatings attract particular attention due to their combination of high mechanical properties, excellent wear resistance, and thermal and chemical stability when operating at high temperatures. These properties make metal-ceramic coatings promising candidates for the creation of high-temperature anti-friction systems [4-6].

Nickel (Ni) and nickel-chromium (NiCr) alloys are widely used as underlay materials in multilayer coatings due to their high heat resistance, corrosion resistance, and good adhesion to metal substrates [7]. The use of NiCr as a transition layer helps to effectively compensate for thermal stresses between the metal base and ceramic coatings, increasing the durability of the systems. One effective way to increase the wear resistance of coatings is to introduce ceramic phases such as aluminum oxide (Al_2O_3) [8]. Due to its high hardness, chemical inertness, and thermal stability, aluminum oxide has proven itself to be a promising component for creating tribological coatings that operate at elevated temperatures [9-11]. Earlier, Feng Liu and co-authors [12] investigated the mechanical and tribological properties of NiCr- Al_2O_3 composites at elevated temperatures. Their results confirmed the effectiveness of such systems for use in high-temperature friction conditions. However, most studies focused mainly on homogeneous composite materials. Unlike

---

Received 2 August 2025; revised 17 December 2025; accepted 5 January 2026.

(https:doi.org/……)

previous works, this study focuses on obtaining a gradient multilayer structure based on NiCr/NiCr-Al_2O_3/Al_2O_3. Gradient coatings provide a gradual change in composition between layers, which effectively reduces interlayer stresses arising from differences in the thermal and mechanical properties of the metal and ceramic phases. This approach improves adhesion between layers, increases crack resistance, and extends the service life of coatings during high-temperature operation [13,14].

The detonation spraying method is an effective technology for producing multilayer coatings with high density, low porosity, and high adhesion between layers. Due to the high particle velocity and rapid cooling, coatings with a specified structure and phase composition can be obtained. Of particular relevance is the creation of gradient multilayer systems, in which a gradual change in composition between layers reduces interlayer stresses and improves performance characteristics [15-17].

In this regard, the aim of this work is to obtain and study multilayer metal-ceramic coatings based on NiCr/NiCr-Al_2O_3/Al_2O_3, obtained by detonation spraying, with different numbers of layers (three-layer, five-layer, and six-layer structures). Particular attention is paid to analyzing the influence of the coating structure on the microstructural, phase, mechanical, and tribological properties during high-temperature operation.

2. Materials and methods

To conduct experiments on obtaining metal-ceramic coatings by detonation spraying, six samples were prepared from 12Kh18N10T steel rod (analogous to AISI 321; chemical composition, wt.%: Fe - base, Ni - 10, Cr - 18, Ti - 0.5, C - 0.12, Mn <2). The blanks were discs with a diameter of 50 mm and a thickness of 3 mm. Before applying the coatings, the surface of the 12Kh18N10T substrates was mechanically polished to ensure an average roughness Ra of less than 0.7 µm.

NiCr powder (Amperit 250.001) containing 80 wt% Ni and 20 wt% Cr with a particle size of about 63 µm (supplier - VIRS LLC, Kiev, Ukraine) was used as the metal component. White electrocorundum Al_2O_3 (grade 25A M40 Super, 87 wt% Al_2O_3, 13 wt% TiO_2, fraction 34 ±6 µm) supplied by INOKS LLC (Novosibirsk, Russia) was used as the ceramic component. The powder mixture was activated in a PULVERISETTE 23 planetary ball mill (FRITSCH, Germany). The mechanical activation time was 2 hours at a frequency of 30 Hz.

Multilayer metal-ceramic coatings based on NiCr/NiCr-Al_2O_3/Al_2O_3 were obtained by detonation spraying using the CCDS2000 installation (LICh SB RAS, Novosibirsk, Russia) [18]. Acetylene and oxygen were used as the combustible mixture during the spraying process. The Al_2O_3-based ceramic layer was sprayed at a gas mixture ratio of $O_2/C_2H_2 = 1.856$, with the detonation apparatus barrel filled to 63% with the explosive gas mixture. To obtain a NiCr metal layer, a gas ratio of $O_2/C_2H_2 = 1.063$ was used with a barrel filling degree of 54%. During the experiment, coatings with different numbers of layers were obtained: three-layer, five-layer, and six-layer.

The three-layer structure was obtained as follows: a NiCr metal layer was applied as the first layer to a pre-prepared surface of a 12Kh18N10T steel substrate; the second layer was a composite layer obtained by spraying a mixture of NiCr and Al_2O_3 powders in a mass ratio of 50:50; the final (third) layer was a ceramic layer of Al_2O_3. The five-layer coatings had a gradient structure, including the sequential application of the following layers: a NiCr metal layer, followed by three transitional composite layers obtained from powder mixtures of NiCr and Al_2O_3 with varying component ratios (75:25, 50:50, and 25:75 wt%), and, as the outer (fifth) layer, a ceramic layer of Al_2O_3. This gradient transition from the metal to the ceramic phase made it possible to reduce interlayer stresses and increase the adhesion of the coating. Six-layer coatings were created by sequentially alternating metal (NiCr) and ceramic (Al_2O_3) layers. The parameters of the technological mode for applying multilayer metal-ceramic coatings of the NiCr/NiCr-Al_2O_3/Al_2O_3 system are presented in Table 1.

Table 1. Technological parameters for obtaining multilayer gradient coatings based on NiCr/NiCr- Al_2O_3/ Al_2O_3.

Coating	Sprayed layers	Barrel filling volume, %	Number of shots
Three-layer	Al_2O_3	63	20
	NiCr(50%)-Al_2O_3(50%)	54	20
	NiCr	63	20
	Substrate	-	-

Table 1. (continued)

Coating	Sprayed layers	Barrel filling volume, %	Number of shots
Five-layer	Al_2O_3	63	10
	NiCr(25)-Al_2O_3(75)	63	10
	NiCr(50)-Al_2O_3(50)	54	10
	NiCr(75)-Al_2O_3(25)	54	10
	NiCr	54	10
	Substrate	-	-
Six-layer	Al_2O_3	63	5
	NiCr	54	5
	Al_2O_3	63	5
	NiCr	54	5
	Al_2O_3	63	5
	NiCr	54	5
	Substrate	-	-

The phase composition of multilayer metal-ceramic coatings was studied by X-ray diffraction using an X'Pert Pro diffractometer (Philips Corporation, Amsterdam, The Netherlands) in 2θ angle scanning mode in the range from 20° to 90°.

A TESCAN MIRA3 LMH scanning electron microscope (TESCAN, Brno, Czech Republic) equipped with an INCA ENERGY energy dispersive analysis attachment (Oxford Instruments, UK) was used to study the microstructure of multilayer metal-ceramic coatings.

Surface roughness (Ra) was determined using a 130 profilometer in accordance with GOST 25142-82. When determining the roughness of coatings, a speed of 0.25 mm/s, a measuring scale of 500 µm, and a travel distance of 5 mm were selected.

The microhardness of the coatings was determined using the Vickers method in accordance with GOST 9450-76 (ASTM E384-11) using a Metolab 502 microhardness tester (Metolab, Russia), with an indenter load of 0.1 N and an exposure time of 10 s.

High-temperature testing of tribological properties was carried out using a THT800 Anton Paar tribometer at a temperature of 700°C. During the tests, a load of 8 N, a sapphire ball with a diameter of 6 mm as a counterbody, and a linear sliding speed of 10 cm/s were used.

3. Results and discussion

The microstructural features of multilayer metal-ceramic coatings obtained by detonation spraying were investigated using cross sections with scanning electron microscopy in backscattered electron (BSE) mode, as well as elemental mapping using energy dispersive spectral analysis (EDS). Fig. 1 shows the obtained microstructure images illustrating the structure of coatings with different layer thicknesses (three-layer, five-layer, and six-layer structures).

Fig. 1a shows a cross-section of a three-layer metal-ceramic coating obtained by detonation spraying. Analysis of the microstructure shows clearly defined boundaries between the layers: metal (NiCr), composite (50% NiCr - 50% Al_2O_3), and ceramic (Al_2O_3). The resulting structure is characterized by density and the absence of defects in the form of pores and delamination, which indicates the high efficiency of the detonation spraying process. Fig. 1b shows the microstructure of a cross-section of a five-layer metal-ceramic coating (NiCr, 75% NiCr - 25% Al_2O_3, 50% NiCr - 50% Al_2O_3, 25% NiCr - 75% Al_2O_3, Al_2O_3). The structure of the coating demonstrates a gradual change in composition between layers, characteristic of gradient systems. The transition from the metal layer to the ceramic layer is achieved through intermediate layers with a smooth change in the concentration of components, which reduces stress and improves adhesion. The coating is characterized by a uniform structure and high-quality distribution of components throughout its thickness, with no signs of porosity or structural damage. Microstructural images of six-layer coatings (Fig. 1c) show a clear layered structure formed by alternating metal (NiCr) and ceramic (Al_2O_3) layers. The boundaries between the layers are clearly distinguishable. However, scratches and signs of interlayer delamination are observed in the structure. The presence of delamination may be due to the occurrence of significant internal stresses during the coating process. These stresses usually arise due to differences in the thermal expansion coefficients between the metal and ceramic layers. During cooling after deposition, such differences can lead to the formation of residual stresses at the interphase boundaries, which reduces the adhesive strength and contributes to local delamination.

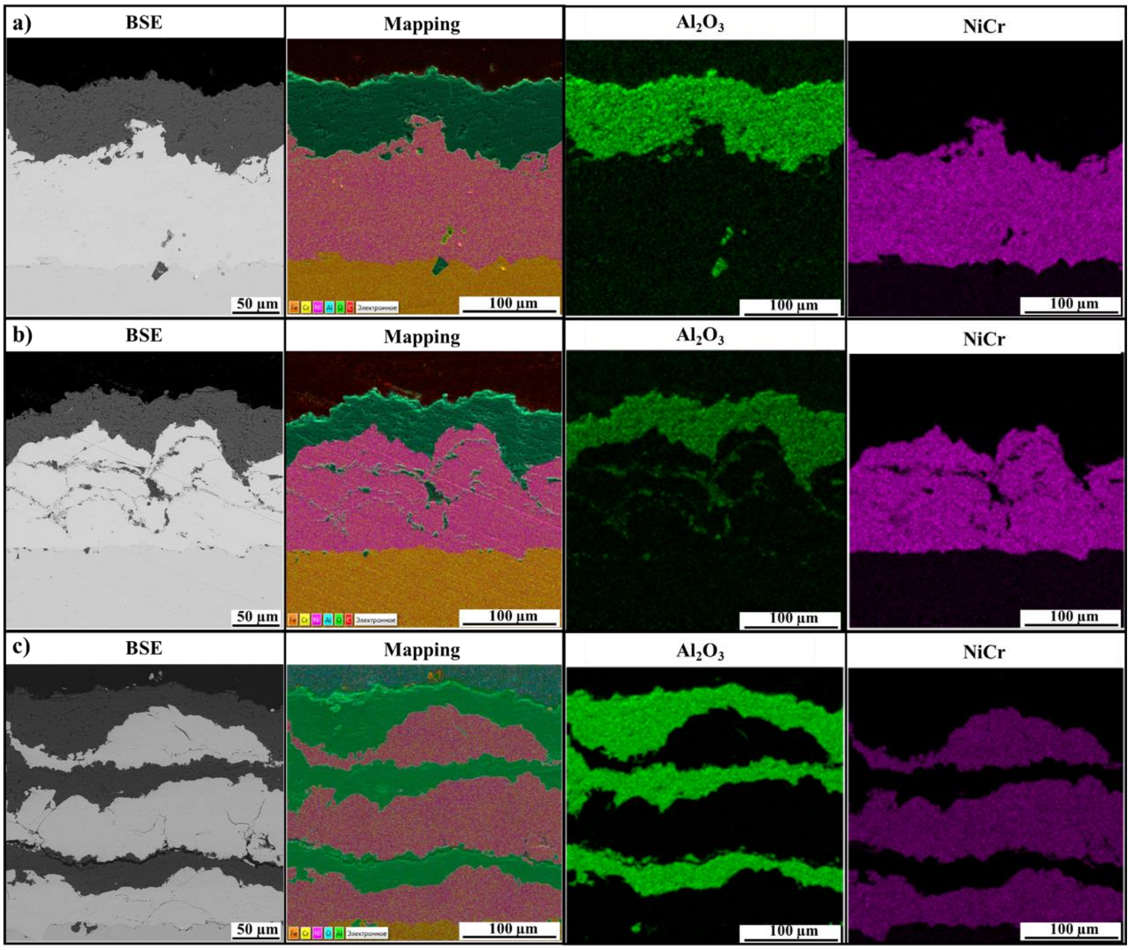

Fig. 1. Microstructure of the cross section of multilayer NiCr/NiCr - Al_2O_3/ Al_2O_3 coatings obtained by detonation spraying: a) three-layer; b) five-layer (gradient); c) six-layer (alternating metal and ceramic layers).

Based on X-ray phase analysis data (Fig. 2), NiCr, α-Al_2O_3, and γ-Al_2O_3 phases were identified in the composition of multilayer metal-ceramic coatings. For three-layer and five-layer coatings, the main phase of the surface layer is Al_2O_3, which indicates the predominance of the ceramic component in the upper layer. In the case of a six-layer coating, the main peaks on the diffractogram correspond to the NiCr phase, which may be due to the fact that the metal layer was closer to the surface. This is explained by the fact that X-rays penetrate to a depth of about 20-30 µm, and with a more complex structure, they capture not only the upper layers but also the inner layers. In addition, the presence of γ-Al_2O_3 phases in some areas of the coatings was observed in all the samples studied-both three-layer and five- and six-layer ones. The appearance of this metastable phase may indicate differences in the crystallization conditions that arise during the deposition process, in particular due to local overheating, uneven temperature distribution across the coating thickness, or changes in the cooling rate.

It should be noted that the thickness and phase composition of the coatings are significantly influenced by the number of detonation pulses (shots) used to obtain each layer. In particular, when obtaining three-layer coatings, each layer was created using 20 detonation shots, which contributed to the formation of layers with increased thickness and, accordingly, ensured a significant total thickness of the entire coating. In the case of five-layer coatings, the number of shots was 10 per layer, and for six-layer coatings, only 5 shots per layer. Thus, as the number of layers increased, the total number of pulses was divided among a larger number of layers, which probably led to a decrease in the individual thickness of each layer. As a result of the decrease in the thickness of the surface layers, especially in six-layer coatings, there is an increased contribution of the inner layers to the X-ray diffraction pattern. This explains the dominance of NiCr phase peaks in the diffractogram of six-layer structures. Nevertheless, it should be emphasized that the Al_2O_3 phase was detected in all types of coatings, including six-layer ones, but its reflection intensity was significantly lower compared to three- and five-layer structures. This indicates the presence of a ceramic component even in the case of thinner top layers, but in smaller quantities, which is confirmed by the reduced intensity of the corresponding diffraction peaks.

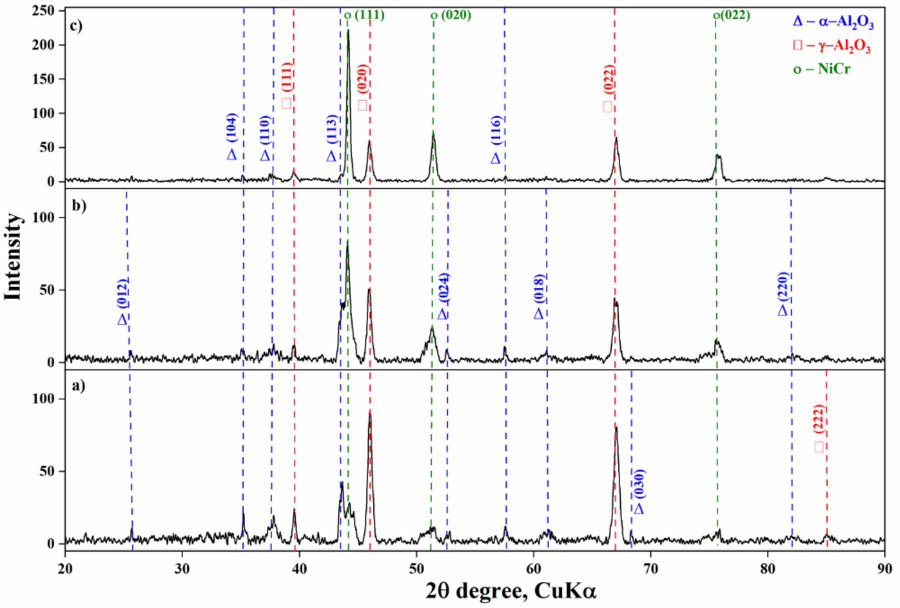

Fig. 2. Diffractogram of multilayer metal-ceramic coatings: a) three-layer coating; b) five-layer coating; c) six-layer coating.

Fig. 3 shows the results of hardness and surface roughness of multilayer metal-ceramic coatings based on NiCr/NiCr - Al_2O_3/Al_2O_3. The data obtained show that the values of these characteristics are within a similar range for all types of coatings studied. That is, despite differences in the number of layers, the behavior of hardness and roughness remains similar for coatings with different layer thicknesses, which indicates the stability of these properties for different structures.

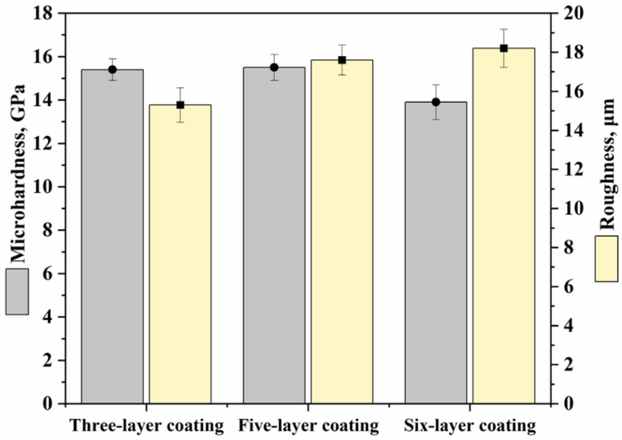

Fig. 3. Hardness and roughness values for multilayer metal-ceramic coatings based on NiCr/NiCr- Al_2O_3/Al_2O_3.

Fig. 4 shows the dependence of the friction coefficient on the distance traveled for three types of multilayer metal-ceramic coatings (three-layer, five-layer, and six-layer) obtained on the basis of NiCr/NiCr-Al_2O_3/ Al_2O_3 at a temperature of 700 °C. According to the results of our previous studies [18], five-layer coatings demonstrated the lowest friction coefficient value-about 0.45 - and were characterized by high wear resistance at room temperature. At the same time, three-layer coatings were characterized by a higher friction coefficient, close to 0.75. For six-layer coatings, a gradual increase in the friction coefficient was observed from an initial value of 0.15 to a stable level of about 0.75. In addition, when testing at room temperature, no significant noise was recorded on the friction coefficient graphs, which indicated the stability of the tribological behavior of the coatings. Analysis of the friction curves obtained in this work confirms that the coating structure and test temperature have a significant effect on its tribological properties.

Fig. 4a shows the dependence of the friction coefficient (red line) on the distance traveled for a three-layer metal-ceramic coating tested at a temperature of 700 °C. In the initial stage of the test, a sharp increase in the friction coefficient is observed, reaching a value of about 0.75, after which it remains at this level for most of the test, showing only slight fluctuations. Insignificant fluctuations in the coefficient may be due to periodic flaking or destruction of the upper ceramic layer of the coating. The green curve shows changes in the depth of penetration of the counterbody into the coating during the test. At the initial stage, a gradual increase in depth is recorded, indicating wear-in and partial destruction of the outer layer. Subsequently, the penetration depth reaches a stable level, indicating stabilization of the wear process. This detailed behavior is characteristic of coatings with a gradient or layered structure, where contact with a harder and more wear-resistant sublayer occurs after the surface layer is removed. The temperature stability reflected by the blue curve confirms the uniform thermal impact on the sample throughout the test, which excludes the influence of thermal fluctuations on the tribological behavior of the coating.

The friction coefficient for the five-layer coating shows more stable behavior compared to the three-layer coating (Fig. 4b). In the initial stage of the test, a smooth increase in the coefficient value to a level of about 0.6 is observed, after which the curve reaches a stable state with insignificant fluctuations. After a distance of about 60 m, a moderate increase in the friction coefficient is recorded, which is probably due to the wear of the top layer and the beginning of interaction with deeper layers of the coating, which have different tribological properties. The penetration depth of the counterbody (green curve) remains at a relatively low and stable level throughout the test, which indicates the high wear resistance of the coating. The temperature regime (blue curve) remains stable throughout the experiment.

For six-layer coatings, the friction coefficient (red curve) increases rapidly at the initial stage of the test and reaches a value of about 0.6. Significant fluctuations are observed in the interval from 20 to 70 m, which may indicate unstable friction associated with the heterogeneity of the upper layers of the coating and their gradual destruction. The peak intensity of the fluctuations is recorded at approximately 60-70 m, after which the curve stabilizes at a level of about 0.6, indicating the establishment of a more uniform mode of interaction with the hardened inner layers. The penetration depth of the counterbody (green curve) shows steady growth in the initial stage, and then reaches a stable level with local irregularities, probably due to the alternation of hard and softer intermediate layers in the coating structure. This indicates gradual wear throughout the entire thickness of the layered coating structure. The temperature regime (blue curve) also remains constant throughout the test.

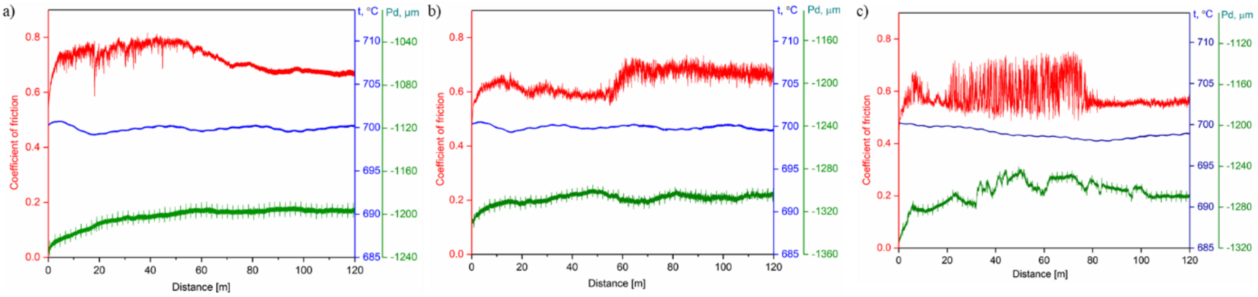

Fig. 4. Dependence of the friction coefficient on distance for multilayer metal-ceramic coatings at a temperature of 700 °C.

4. Conclusion

In this work, multilayer metal-ceramic coatings based on NiCr/NiCr - Al_2O_3/Al_2O_3 were successfully obtained by detonation spraying with a different number of layers - three-layer (NiCr, 50% NiCr - 50% Al_2O_3, Al_2O_3), five-layer (NiCr, 75% NiCr - 25% Al_2O_3, 50% NiCr - 50% Al_2O_3, 25% NiCr - 75% Al_2O_3, Al_2O_3) and six-layer structures (NiCr, Al_2O_3, NiCr, Al_2O_3, NiCr, Al_2O_3). A comprehensive analysis, including scanning electron microscopy, X-ray phase analysis, microhardness and roughness measurements, and tribological tests at 700 °C, allowed us to establish the influence of the coating structure on its performance characteristics.

It was found that the best results were demonstrated by five-layer coatings formed as a gradient structure with a smooth transition from the metal to the ceramic phase. This structure ensured a reduction in internal stresses and increased adhesion between the layers, which was confirmed by microstructural homogeneity, the absence of porosity, and defects at the interphase boundaries. X-ray phase analysis revealed the predominance of the Al_2O_3 ceramic phase in the upper layer of the coating. The microhardness and roughness of the five-layer coatings were comparable to other types of coatings, while demonstrating uniform distribution over the surface. Tribological tests showed that the five-layer coatings had the lowest and most stable coefficient of friction (~0.6) among all the samples studied, as well as the minimum penetration depth of the counterbody, which indicates high wear resistance.

Funding

This research was funded by the Science Committee of the Ministry of Science and Higher Education of the Republic of Kazakhstan (grant No. BR24992876).

Conflict of interest

The authors declare no conflict of interest.

References

1 Sreedhar, G., Alam, M. M., & Raja, V. S. (2009). Hot corrosion behaviour of plasma sprayed YSZ/Al_2O_3 dispersed NiCrAlY coatings on Inconel-718 superalloy. *Surface and Coatings Technology*, 204(3), 291-299. DOI: https://doi.org/10.1016/j.surfcoat.2009.07.026

2 Zhu, C., Javed, A., Li, P., Yang, F., Liang, G. Y., & Xiao, P. (2012). A study of the microstructure and oxidation behavior of alumina/yttria-stabilized zirconia (Al_2O_3/YSZ) thermal barrier coatings. *Surface and Coatings Technology*, 212, 214-222. https://doi.org/10.1016/j.surfcoat.2012.09.052

3 Liu, F., Jia, J., Yi, G., Wang, W., & Shan, Y. (2015). Mechanical and tribological properties of NiCr–Al_2O_3 composites at elevated temperatures. *Tribology International*, 84, 1-8.. https://doi.org/10.1016/j.triboint.2014.11.023

4 Ozgurluk, Y., Gulec, A., Ozkan, D., Binal, G., Karaoglanli, A. C. (2023). Structural characteristics, oxidation performance and failure mechanism of thermal barrier coatings fabricated by atmospheric plasma spraying and detonation gun spraying. *Engineering Failure Analysis*, 152, 107499. https://doi.org/10.1016/j.engfailanal.2023.107499

5 Vaßen, R., Jarligo, M. O., Steinke, T., Mack, D. E., Stöver, D. (2010). Overview on advanced thermal barrier coatings. *Surface and Coatings Technology*, 205(4), 938-942. https://doi.org/10.1016/j.surfcoat.2010.08.151

6 Oliker, V. E., Abdurashitova, S. A., Martsenyuk, I. S., Grechishkin, E. F., Bondarenko, A. A. (2013). Microstructure and properties of detonation-sprayed thermal barrier ZrO_2 coatings. *Powder Metallurgy and Metal Ceramics*, 52(1), 83-89. https://doi.org/10.1007/s11106-013-9498-6

7 Ak, N. F., Tekmen, C., Ozdemir, I., Soykan, H. S., & Celik, E. R. D. A. L. (2003). NiCr coatings on stainless steel by HVOF technique. *Surface and coatings technology*, 174, 1070-1073. https://doi.org/10.1016/S0257-8972(03)00367-0

8 Edlmayr, V., Moser, M., Walter, C., & Mitterer, C. (2010). Thermal stability of sputtered Al_2O_3 coatings. *Surface and Coatings Technology*, 204(9-10), 1576-1581. https://doi.org/10.1016/j.surfcoat.2009.10.002

9 Rakhadilov, B. K., Tyurin, Y. N., Kolisnichenko, O. V., Kakimzhanov, D. N., & Zhurerova, L. G. (2022). Structure and properties of multilayer coatings based on CoCrAlY/Al_2O_3 obtained by detonation spraying. *Eurasian Journal of Physics and Functional Materials*, 6(3), 234-243. https://doi.org/10.32523/ejpfm.2022060308

10 Rakhadilov, B., Kantay, N., Sagdoldina, Z., Erbolatuly, D., Bektasova, G., Paszkowski, M. (2021). Experimental investigations of Al_2O_3-and ZrO_2-based coatings deposited by detonation spraying. *Materials Research Express*, 8(5), 056402. https://doi.org/10.1088/2053-1591/abfbb7

11 Bye, G. C., Simpkin, G. T. (1974). Influence of Cr and Fe on Formation of α-Al_2O_3 from γ-Al_2O_3. *Journal of the American Ceramic Society*, 57(8), 367-371. https://doi.org/10.1111/j.1151-2916.1974.tb10925.x

12 Liu, F., Jia, J., Yi, G., Wang, W., Shan, Y. (2015). Mechanical and tribological properties of NiCr–Al_2O_3 composites at elevated temperatures. *Tribology International*, 84, 1-8. https://doi.org/10.1016/j.triboint.2014.11.023

13 Lima, R. S. (2020). Perspectives on thermal gradients in porous ZrO_2-7-8 wt.% Y_2O_3 (YSZ) thermal barrier coatings (TBCs) manufactured by air plasma spray (APS). *Coatings*, 10(9), 812. https://doi.org/10.3390/coatings10090812

14 Buitkenov, D., Rakhadilov, B., Nabioldina, A., Mukazhanov, Y., Adilkanova, M., Raisov, N. (2024). Investigation of Structural Phase, Mechanical, and Tribological Characteristics of Layer Gradient Heat-Protective Coatings Obtained by the Detonation Spraying Method. *Materials*, 17(21), 5253. https://doi.org/10.3390/ma17215253

15 Buitkenov, D., Sagdoldina, Z., Nabioldina, A., & Drenda, C. (2025). The Study of Tribological Characteristics of YSZ/NiCrAlY Coatings and Their Resistance to CMAS at High Temperatures. *Applied Sciences*. https://www.mdpi.com/2076-3417/15/14/8109 (accessed August 1, 2025)

16 Baizhan, D., Sagdoldina, Z., Buitkenov, D., Kambarov, Y., Nabioldina, A., Zhumabekova, V., Bektasova, G. (2023). Study of the Structural-Phase State of Hydroxyapatite Coatings Obtained by Detonation Spraying at Different O_2/C_2H_2 Ratios. *Crystals*, 13(11), 1564. https://doi.org/10.3390/cryst13111564

17 Poliarus, O., Morgiel, J., Pomorska, M., Korniewa-Surmacz, A., Trelka, A., Maj, Ł., Galtsov, K. (2024). Effect of HT cycling in air on Microstructure of Detonation Gun sprayed YSZ/NiCr Coating. *Journal of Thermal Spray Technology*, 33(1), 148-159. https://doi.org/10.1007/s11666-023-01709-9

18 Rakhadilov, B., Buitkenov, D., Sagdoldina, Z., Idrisheva, Z., Zhamanbayeva, M., Kakimzhanov, D. (2021). Preparation and characterization of NiCr/NiCr-Al_2O_3/Al_2O_3 multilayer gradient coatings by gas detonation spraying. *Coatings*, 11(12), 1524. https://doi.org/10.3390/coatings11121524

AUTHORS' INFORMATION

Aiym Nabioldina - junior researcher of Scientific Research Center "Surface Engineering and Tribology" at Sarsen Amanzholov East Kazakhstan University, Ust-Kamenogorsk, Kazakhstan; (e-mail: anabioldina@vku.edu.kz), SCOPUS Author ID: 58728375200, ORCID iD: 0000-0001-5581-2194

Balym Alibekova - engineer of Scientific Research Center "Surface Engineering and Tribology" at Sarsen Amanzholov East Kazakhstan University, Ust-Kamenogorsk, Kazakhstan; (e-mail: bailymalibekova304@gmail.com), ORCID iD: 0009-0001-7644-4527

Garip Erdogan - Sakarya University, Metallurgical and Materials Eng. Dept. Materials Under Extreme Conditions Lab., Sakarya Turkiye; (e-mail: gerdogan@sakarya.edu.tr), SCOPUS Author ID: 55505136500, ORCID iD 0000-0002-3924-9984

Aibek Erkebulanuly Alibekov - engineer of Scientific Research Center "Surface Engineering and Tribology" at Sarsen Amanzholov East Kazakhstan University, Ust-Kamenogorsk, Kazakhstan; (e-mail: aibek.alibekov.03@mail.ru), ORCID iD: https://orcid.org/0009-0008-4271-0170

ORIGINAL STUDY

NUMERICAL SIMULATION OF THE PROCESS OF COLD GAS-DYNAMIC SPRAYING OF COMPOSITE POWDER Al–Zn–TiO₂

Kaiyrzhan Berikkhan[1],[2], Zarina Satbayeva[1], Ainur Zhassulan[1], Aibek Shynarbek[1], Kuanysh Ormanbekov[1]

[1] Engineering Center, Shakarim University, st. Fizkulturnaya 4B, Semey, Kazakhstan;
[2]Department of Technical Physics and Heat Power Engineering, Research School of Physical and Chemical Sciences, Shakarim University of Semey, Republic of Kazakhstan
*Corresponding author: k.berikkhan@shakarim.kz

Abstract. *This paper presents a numerical simulation of the cold gas-dynamic spraying process of Al-Zn-TiO₂ composite powder onto a steel substrate. Using computational fluid dynamics (CFD) in COMSOL Multiphysics, the characteristics of the gas flow in a de Laval nozzle and the particle dynamics are obtained for various spraying parameters. Optimal conditions are determined: gas pressure of approximately 0.6 MPa, temperature of ~600°C, nozzle-to-substrate distance of 15 mm, spray angle of 90°. At these conditions, particles reach supersonic velocities of approximately 500-600 m/s, sufficient for their deposition on steel. It is shown that increasing gas pressure and temperature facilitates particle acceleration and increases their impact energy, while excessively small or large spraying distances reduce the efficiency of the process. Simulation of the impact interaction of particles with the substrate revealed intense plastic deformation of the powders under optimal parameters, ensuring strong adhesion of the coating to the base. The results of the numerical experiment are consistent with the observed characteristics of dense and adhesion-strong coatings. It has been established that the proposed CFD model can be used as an effective tool for optimizing the parameters of cold gas-dynamic spraying of composite powders.*

Keywords:cold gas-dynamic spraying; numerical modeling; CFD; composite coating; aluminum-zinc-titanium dioxide; particle velocity; critical velocity; plastic deformation.

1. Introduction

Cold Gas Dynamic Spray (CGDS) is a solid-phase coating application method in which powder particles are accelerated to high velocities by a heated, compressed gas stream and deposited onto a substrate by high-speed impact without melting [1, 2]. Since the particles are not heated to the melting temperature, the coating is formed without oxidation or other thermal damage to the base material [3]. The result is dense, low-porosity coatings with predominantly compressive residual stresses [4]. CGDS allows coating heat-sensitive materials without overheating and preserving the original powder microstructure [5].

Currently, the CGDN method is successfully used to deposit various materials-pure metals, alloys, and metal-matrix composites [6, 7]. The particles bond to the substrate through their strong plastic deformation upon impact, which leads to the formation of a strong interfacial bond without melting [8]. It is known that certain impact conditions are necessary for successful particle deposition-in particular, the particle velocity must exceed a critical value that ensures adhesion of a given material to the substrate [9, 10]. For example, for aluminum on steel, the critical velocity is approximately 500 m/s [9, 10]. If the particle moves more slowly, it will not adhere to the surface, so reaching and exceeding the critical velocity is a key factor in the process.

The velocity and energy of the particles are affected by the process parameters of the CGDN: gas pressure and temperature, nozzle geometry, nozzle-to-substrate distance (nozzle overhang), particle size, and spray angle [11, 12]. Increasing the gas pressure and temperature increases the flow velocity and particle acceleration due to an increase in the pressure gradient and a decrease in the gas density [13, 14]. Reducing the nozzle overhang (spraying too close) can lead to under-acceleration of the particles and their flattening against the

---

Received 5 December 2025; revised 17 December 2025; accepted 5 January 2026.

(https:doi.org/……)

substrate, while an excessively large overhang leads to dispersion and deceleration of the particles in the air [15, 16]. Each powder material has its own critical deposition velocity; for Al-Zn-TiO_2 composite particles, it is determined mainly by the properties of the aluminum matrix (about 500 m/s), since it is the ductile aluminum that ensures adhesion to the substrate. Zinc, being a softer metal, has a lower critical velocity. However, its presence promotes anodic protection and does not impair adhesion. Solid TiO_2 particles dispersed in aluminum increase coating hardness but have virtually no effect on adhesion once the matrix reaches the required velocity. Therefore, modeling requires taking into account the multicomponent nature of the powder, but critical deposition conditions are, as a first approximation, estimated for aluminum.

Experimental optimization of the CGDN process requires repeated parameter variations and coating quality analysis, which is time-consuming and resource-intensive. Therefore, numerical modeling plays an important role in predicting the behavior of the gas flow and particles under various spraying conditions [17, 18]. Computational fluid dynamics (CFD) and impact mechanics methods allow one to determine the velocity and temperature distribution in the jet, particle trajectories and velocities, their temperature, and the stresses upon collision with the substrate. Such models are used to estimate critical velocities and the boundaries of the "deposition window" - the ranges of parameters within which a high-quality coating is formed [19]. In this study, a comprehensive CFD modeling of the CGDN of Al-Zn-TiO_2 composite powder on steel was performed. The goal of the modeling is to determine the parameters at which maximum velocity and efficient particle deposition are achieved, and thereby substantiate the optimal process conditions.

2. Materials and methods

The numerical model was developed in COMSOL Multiphysics AB (v6.2) and includes a coupled analysis of gas flow, particle motion, and impact on the substrate. Deposition onto a flat steel substrate was considered using a 100 mm long de Laval nozzle (convergent-divergent) with a throat diameter of 2 mm and an outlet diameter of 6 mm. The calculations included the inner region of the nozzle and the outer section from the nozzle exit to the substrate surface (Fig. 1). The model is axisymmetric (3D with a degree of symmetry), which is justified by the axial nature of the flow.

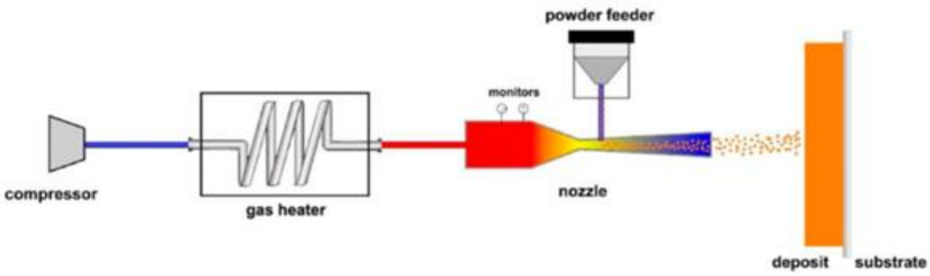

Fig. 1. Installation diagram and calculated setting of the gas turbine.

Turbulent compressible flow equations (RANS, k-ε model) were solved for air as the working gas. The total (stagnation) pressure P0 and temperature T_0 were specified at the nozzle inlet, and the atmospheric pressure of 0.1 MPa was specified at the nozzle outlet. The nozzle walls were assumed to be adiabatic and non-slip. Initial calculations were performed at P0 = 6×105 Pa and T0 = 600 °C (873 K), which corresponds to typical operating conditions.

When flowing through a convergent-divergent nozzle, the gas expands to supersonic speeds-in our case, the calculated exit flow reached ≈1200 m/s at P0 = 0.6 MPa and T0 = 600 °C. Due to adiabatic expansion, the gas temperature in the jet core decreased to approximately ~327 °C. The supersonic core region extended from the nozzle exit to the substrate, forming the so-called "patch" of the shock jet on the surface.

The composite powder particles were defined as a discrete Lagrangian phase (using the Particle Tracing module in COMSOL) in one-way coupling with the gas-that is, the effect of the particles on the flow was neglected due to their low concentration. For simplicity, all particles were assumed to be spherical (in reality, Al-Zn powder has an irregular shape, but for computational efficiency, an equivalent sphere was adopted). The particle diameter was assumed to be 20 μm as representative (fraction 20-50 μm); the material density was ~2700 kg/m^3 (close to aluminum, given that the composition is 80% Al + 15% Zn + 5% TiO_2).

Particles were introduced into the flow at the nozzle throat with initial velocities equal to the local gas velocity (zero slip during introduction). The particles were subjected to drag forces (aerodynamic drag), taking into account the Cunningham correction for small particles, as well as gravity, the effect of which is insignificant for a horizontal spray axis. Interparticle interactions were neglected (rarefied flow).

It was assumed that the particles would not melt or disintegrate during the process-which is justified, since the gas temperature, although high, has a short flight time, and aluminum begins to melt at 660°C; calculations show that the particle temperature does not reach the melting point.

The substrate was modeled as a stationary solid wall; upon particle contact with the substrate, the solution was transferred to the Solid Mechanics module to evaluate deformation. An elastoplastic impact model was used to evaluate the stress-strain state upon particle impact with the substrate: the particle material (primarily aluminum) was described by an elastoplastic model with a yield strength of ~100 MPa, and the substrate material (steel) was described by a yield strength of ~250 MPa. These values correspond to soft Al-Zn powder and St3 steel, respectively. Impact modeling allowed us to assess whether plastic deformations develop in the particle and substrate and whether they are sufficient to form an adhesion contact area.

To study the influence of spraying conditions, a series of calculations were performed with various parameters. The main variable values were: gas pressure P0 (0.4; 0.5; 0.6 MPa), temperature T0 (400; 500; 600 °C), and nozzle offset d (distance from the outlet section to the substrate: 5; 15; 25 mm). The spray angle remained perpendicular (90° to the surface) in all experiments. Each calculation was performed until a steady-state flow regime was established and the particles reached the substrate.

To ensure statistical reliability, the trajectories were modeled for a packet of 100 particles uniformly distributed across the flow cross-section at the inlet. A separate high-precision calculation was also performed for optimal parameters with a fine time step (0.1 μs) for a detailed impact analysis.

For computational stability and reproducibility, standard simplifications for cold spraying were adopted:

1. The sphericity of the particles (although real Al-Zn particles have an irregular shape and contain TiO_2 agglomerates) simplifies the calculation of aerodynamic drag and momentum transfer.
2. The 20 μm monofraction is used as a representative size (actually ~20-50 μm according to specification and SEM); the size distribution was not explicitly modeled.
3. Absence of interparticle collisions and agglomeration in flight; one-way connectivity (particles do not affect the gas).
4. Solid state of particles throughout the entire path (without melting/destruction) and constant properties of materials.
5. The initial particle velocity is equal to the local gas velocity at injection. These assumptions focus the analysis on the key physics of acceleration and impact and make the model computationally tractable.

3. Results and discussion

Computational fluid dynamics predicted that at a pressure of 0.6 MPa and 873 K, the nozzle forms a supersonic jet with a gas discharge velocity of up to ~1200 m/s (Fig. 2a). Under these conditions, Al-Zn-TiO2 particles accelerate to terminal impact velocities of approximately 600-700 m/s at a distance of 15 mm (Fig. 2c). Shorter distances (e.g., 10 mm) lead to underexpansion of the flow and excessive impact forces, while larger distances (>25 mm) allow the particles to decelerate, reducing the impact velocity below the critical threshold for bond formation.

The impact model showed that upon impact, the particles experienced severe plastic deformation and flattened into disc-shaped splats. The von Mises stress within the particle peaked at approximately 300 MPa, confirming localized plastic flow (Fig. 2b). To put an impact stress of 300 MPa in context, this level is an order of magnitude higher than the yield strength of pure aluminum (on the order of only tens of MPa) and comparable to or even higher than the yield strength of mild steel (approximately 250 MPa). This high von Mises stress confirms that the particle moves well beyond its elastic limit, experiencing severe plastic flow, while the substrate surface is also locally fluid. These extreme stress and strain rate conditions favor the formation of adiabatic shear instability (a localized shear band with thermal softening) at the impact boundary rather than bulk melting of the material [20]. In other words, bonding remains a solid-state process dominated by intense plastic deformation and interfacial heating, with no evidence of localized melting or uncontrolled shear failure. Thus, the observed deformation and interfacial loading state are consistent with metallurgical solid-state bonding via plastic deformation, rather than indicating any melting or adiabatic shear instability that compromises the integrity of the deposit. In the substrate region immediately beneath the particle, a stress field approaching the yield strength was observed, resulting in shallow indentation and minor plastic deformation, but without significant damage to the substrate. The high strain rate and localized heating facilitated the formation of an adiabatic shear layer, facilitating metallurgical bonding.

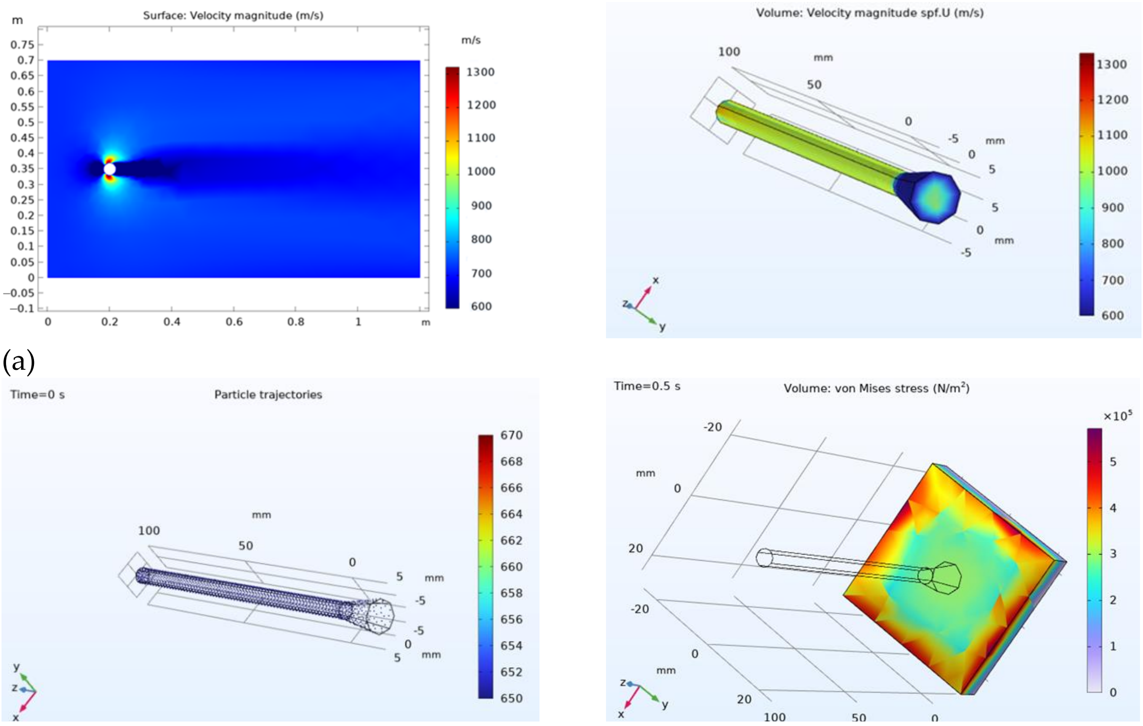

(a)

(b)

(With)

Fig. 2. (a) Surface plot and three-dimensional slice of the velocity magnitude in the midplane; (b) particle trajectories in the nozzle plume; (c) von Mises stress distribution in the substrate at the moment of particle impact.

The simulation results showed that the adhesion efficiency increased significantly with increasing gas pressure and temperature, reaching a stable regime at temperatures above ~0.6 MPa and 600 °C. Based on these data, the cold spraying process was carried out at a temperature of 600 °C, 0.6 MPa, and a distance from the surface of about 15 mm with a moderate powder feed rate (~0.5 g/s), since these parameters ensured sufficient particle velocity and deformation for metallurgical bonding. The resulting coatings had a dense lamellar structure without signs of delamination, which is consistent with the results of previous studies emphasizing the crucial role of impact conditions in ensuring adhesion [21, 22].

Numerical simulations in COMSOL Multiphysics provided a detailed understanding of the sputtering process. The gas jet reached supersonic speeds, creating a high-velocity core in which particles accelerated to 500-600 m/s under optimal conditions (0.6 MPa, 600°C, 15 mm standoff, 90° spray angle) (Fig. 2a). Impact simulations showed that these velocities generated sufficient plastic deformation and interfacial stress for effective adhesion. Curved surface simulations showed that particle impact velocities decreased slightly at the edges due to deflection, explaining the minor thickness variations. Numerical predictions matched experimental trends for deposition efficiency, roughness, and coating quality, confirming the model's reliability as a tool for process optimization.

Optimal deposition parameters were determined based on a comprehensive analysis of gas-dynamic modeling and experimental observations. Coatings deposited at a gas pressure of 0.6 MPa, a gas temperature of 600°C, and a distance from the electrode of 15 mm demonstrated the most favorable microstructural characteristics: dense particle packing, a uniform layered structure, and the absence of delamination.

To confirm the choice of optimal sputtering conditions, a series of computational fluid dynamics calculations were performed at a constant gas temperature of 800 K and a fixed nozzle-to-substrate distance of 0.01 m, while the working gas pressure varied from 4 × 105 Pa to 6 × 105 Pa. The gas and particle flow velocity fields were visualized for each condition (Fig. 3a-c). The simulation results clearly show that increasing the pressure leads to a significant increase in the particle velocity at the nozzle outlet.

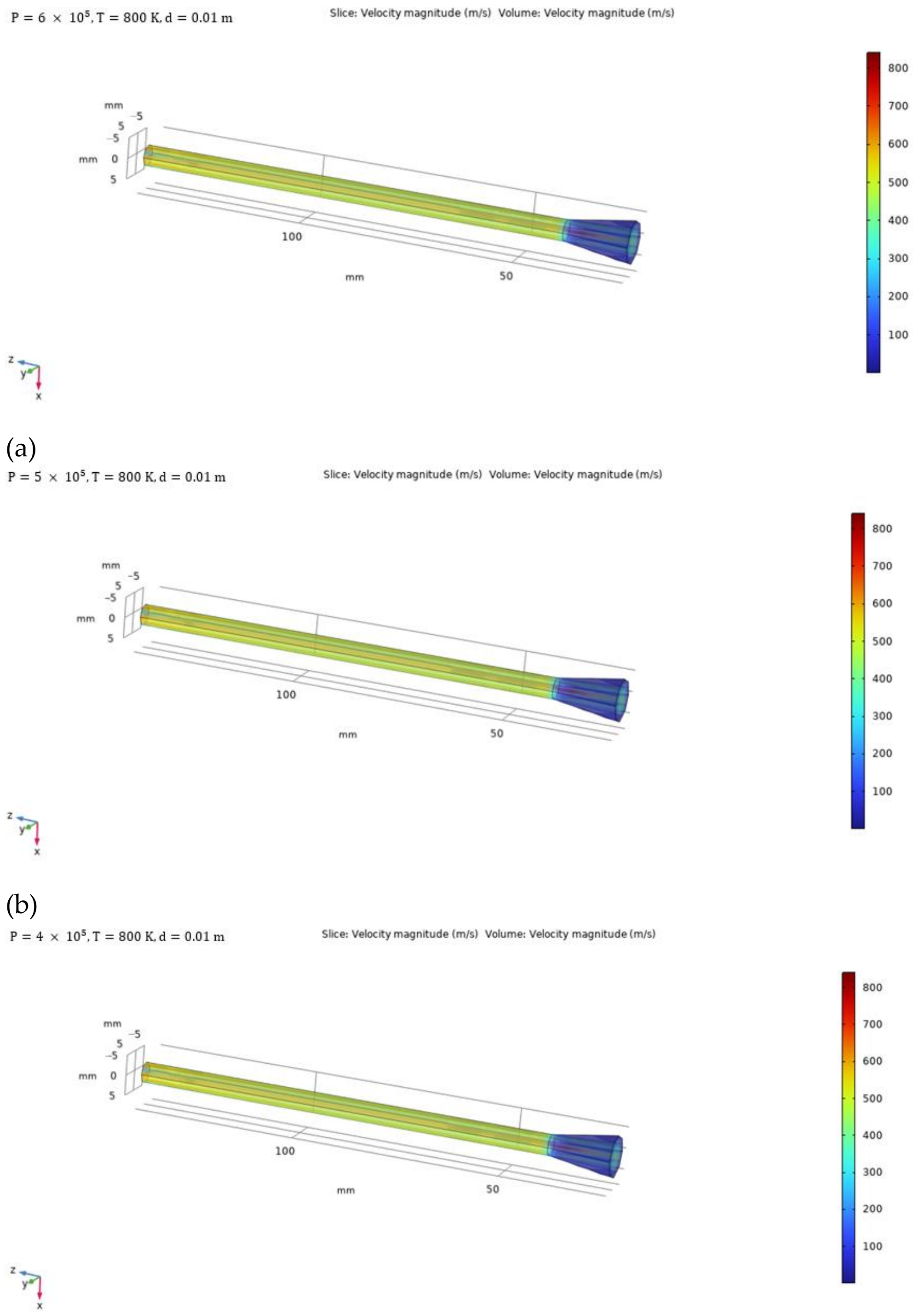

(a)

(b)

(With)

Fig. 3. (a) Velocity distribution at P = 6 × 105 Pa, T = 800 K, d = 0.01 m;(b) Velocity distribution at P = 5 × 105 Pa, T = 800 K, d = 0.01 m;(c) Velocity distribution at P = 4 × 105 Pa, T = 800 K, d = 0.01 m.

At a pressure of 4 × 105 Pa, the maximum particle velocity was approximately 620 m/s. At a pressure of 5 × 105 Pa, it increased to approximately 710 m/s. At a pressure of 6 × 105 Pa, the particle velocity exceeded 820 m/s. This indicates that higher chamber pressure leads to greater particle acceleration due to increased pressure gradients along the nozzle. Since particle velocity directly affects the deposition behavior (e.g., the degree of particle deformation upon impact and adhesion), the conditions P = 6 × 105 Pa and T = 800 K are considered optimal for producing high-quality coatings.

Fig. 4a and 4b show the temporal evolution of the gas temperature field inside the nozzle from t = 0 s to t = 0.05 s, simulated with a time step of 0.001 s. At the initial instant (t = 0 s), the temperature remains relatively uniform along the entire length of the nozzle and is ~800 K, indicating stable initial thermal conditions (Fig. 4a). As the simulation progresses, by t = 0.05 s (Fig. 4b), a pronounced temperature gradient arises, with higher temperatures concentrated near the nozzle walls and inlet, and cooler regions located downstream. This behavior indicates adiabatic expansion and energy dissipation of the working gas along the nozzle. Localized heating zones indicate the development of a boundary layer, which affects both the gas velocity and the thermal energy transfer by particles.

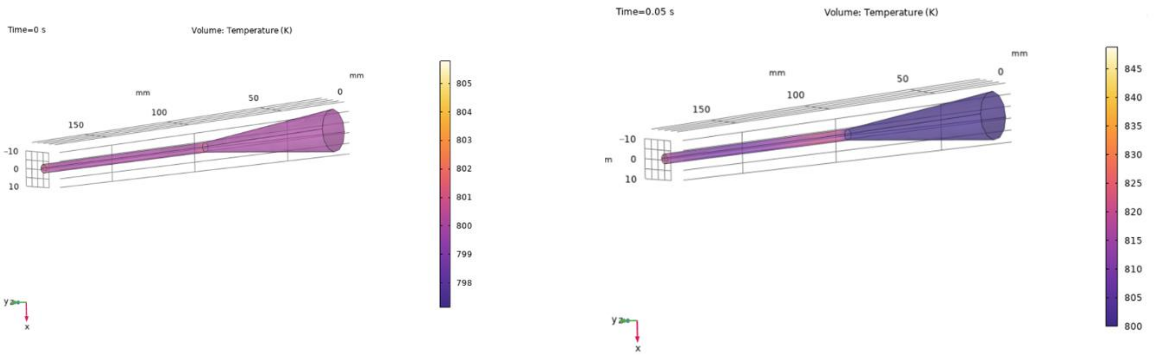

(a) (b)

Fig. 4. Temperature distribution in the spray jet at times (a) 0 s and (b) 0.05 s.

Fig. 5 shows the evolution of particle trajectories over the simulation interval from 0 to 0.05 s. The data was obtained with high temporal resolution (0.001 s step). The simulation reflects the behavior of particles under the influence of a supersonic gas jet during cold spraying.

At time = 0 s, the particles are densely grouped near the nozzle entrance, indicating their injection into the flow with an initially uniform spatial distribution (Fig. 5a). By time = 0.05 s, the particles have advanced significantly along the nozzle axis, forming a focused, high-speed flow (Fig. 5b). Convergence toward the centerline indicates effective particle acceleration and aerodynamic focusing, due to the nozzle geometry and gas flow dynamics.

This trajectory evolution is crucial, as it directly correlates with particle impact velocity and deposition efficiency. The highest particle density reaching the substrate is observed in the stagnation region near the nozzle exit, ensuring efficient coating formation under the simulated pressure and temperature conditions.

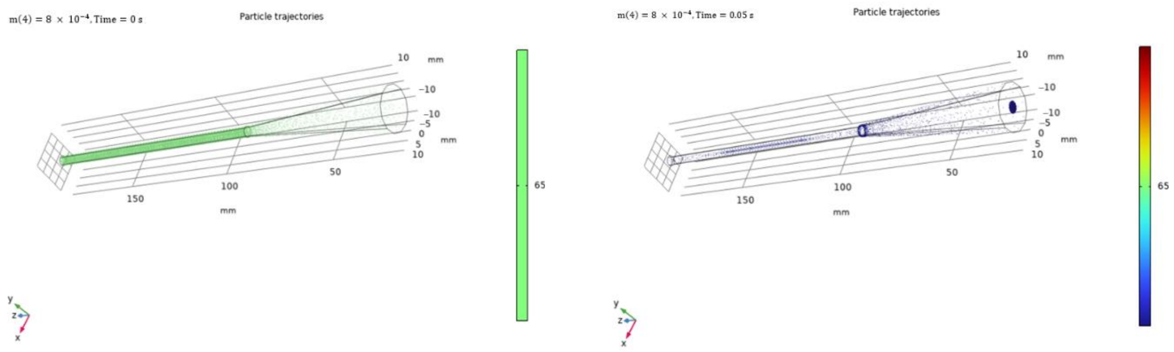

(a) (b)

Fig. 5. (a) Particle trajectories at t = 0 s; (b) Particle trajectories at t = 0.05 s.

Computational fluid dynamics (CFD) and thermal modeling calculations confirmed that increasing the gas pressure from 4 × 105 Pa to 6 × 105 Pa (at a gas temperature of 800 K) leads to a significant increase in particle exit velocity, exceeding 650 m/s at maximum pressure. This indicates increased deposition potential at elevated driving forces. Modeling also identified a distance of ~15 mm as favorable, where particles maintain high velocity and focus on the substrate surface, promoting efficient deposition and uniform coating growth. Thermal modeling showed that the gas temperature on the substrate after expansion remained around 500 K, significantly below the melting point of the materials, preventing thermal degradation.

The particle flight velocities predicted by the model were compared with experimental data to assess the model's validity. CFD simulations showed that under optimal spraying conditions (gas pressure of ~0.6 MPa, gas temperature of ~600°C, and a 15 mm offset), the particles would reach impact velocities of approximately 500-600 m/s. This predicted velocity range exceeds the typical critical velocity (~500 m/s) required for aluminum particles to adhere to a steel substrate. As predicted, coatings were successfully deposited at 0.6 MPa and 600°C with strong adhesion, indicating that the particles indeed achieved velocities high enough to exceed the adhesion threshold. In contrast, at lower stagnation pressures (0.4 MPa) or gas temperatures (400°C), the model predicted a significant reduction in particle velocity, and experiments under these conditions resulted in either very poor adhesion or no coating deposition, indicating that the particles did not reach critical velocity in these cases. Although direct measurement of particle velocity was not available in our setup, these qualitative results (the presence or absence of an effective coating) provide indirect confirmation of the modeling results. Furthermore, the model correctly captured the effect of standoff distance on particle velocity and deposition: it predicted an optimal standoff window of approximately 10-20 mm (with ~15 mm being ideal) and showed that extreme standoff distances would be detrimental (particles would experience excessive drag at large distances or incomplete acceleration at very short distances). This behavior was confirmed experimentally: for example, at a distance of 5 mm, the high-velocity gas jet caused particle splashing and substrate abrasion instead of effective deposition, while at a distance of 25 mm, the particles slowed down and led to insignificant coating buildup. Such close agreement between simulated particle velocities and experimental results convincingly confirms the accuracy of the COMSOL model. In particular, the model's ability to predict successful and unsuccessful deposition conditions (via velocity thresholds and trends) confirms its credibility as a reliable predictive tool for optimization and parameter selection in the cold gas dynamic spraying process.

4. Conclusion

Numerical modeling of the CGD process for Al-Zn-TiO_2 powder allowed us to identify the optimal parameters for efficient coating deposition. It was found that at a gas pressure of approximately 0.6 MPa, a temperature of approximately 600°C, a nozzle-to-substrate distance of approximately 15 mm, and a perpendicular spray angle (~90°), particles accelerate to supersonic velocities (~500-600 m/s), exceeding the critical deposition velocity of aluminum on steel (approximately 500 m/s). Achieving this velocity ensures intense plastic deformation of the particles upon impact and strong adhesion of the coating to the substrate without melting the material. It has been shown that increasing the pressure (up to ~0.6-0.7 MPa) and gas temperature (up to ~600-800 °C) leads to an increase in the particle velocity at the nozzle outlet and, consequently, to an increase in their impact energy, which contributes to an increase in the efficiency of forming a dense and adhesively strong coating. Conversely, deviations from the optimal spraying distance negatively affect the process: too small an extension (e.g., 5 mm) leads to insufficient particle acceleration and the effects of scattering and erosion of the substrate by the high-speed jet, while too large an extension (e.g., 25 mm) causes the particles to slow down in the air and reduce their ability to attach to the surface. Thus, the existence of a "spraying window" is confirmed – a range of distances of approximately 10-20 mm (for the given conditions) within which maximum deposition efficiency is achieved (with an optimum of approximately 15 mm), while going beyond this range sharply reduces the coating quality.

A key result is the identification of the particle adhesion mechanism: upon impact at supersonic speed, stresses and strains develop in the particle material that significantly exceed the yield strength (estimated equivalent stresses of ~300 MPa for aluminum), indicating severe plastic deformation without melting. Simulation confirmed the formation of a local adiabatic shear band upon impact, which facilitates the destruction of the oxide film and metallurgical adhesion at the interface without melting. Thus, the numerical model reliably describes the physics of the cold spray process and can serve as an effective tool for predicting and optimizing its parameters. The obtained results are consistent with literature data and experimental observations, and the developed model has practical significance for managing the quality of cold sprayed coatings.

Funding

This work does not receive any funding.

Conflict of interest

The authors declare no conflict of interest.

References

1 Klinkov SV, Kosarev VF, Rein M. (2005) Significance of particle impact phenomena in cold spray deposition. *Aerospace Science and Technology*. Vol.9, No.8. P.582–591

2 Alkhimov AP, Kosarev VF, Klinkov SV (2001) The features of cold spray nozzle design. *Journal of Thermal Spray Technology*. Vol.10, No.2. P.375–381

3 Papyrin A., Kosarev V., Klinkov S., Alkhimov A., Fomin V. (2006) Cold Spray Technology. *Amsterdam: Elsevier*, 336

4 Champagne VK (Ed.) The Cold Spray Materials Deposition Process: Fundamentals and Applications. *Cambridge: Woodhead Publishing*, (2007). 360

5 Villafuerte J. (Ed.) Modern Cold Spray: Materials, Process, and Applications. *Berlin: Springer*, (2015). 345

6 Hassani-Gangaraj S.M., Moridi A., Guagliano M. (2015) Critical review of corrosion protection by cold spray coatings. *Surface Engineering*. Vol.31, No.12. 803–815

7 Assadi H., Kreye H., Gärtner F., Klassen T. Cold spraying - A materials perspective. Acta materialia. (2016). Vol.116. 382–407

8 Assadi H., Gärtner F., Stoltenhoff T., Kreye H. Bonding mechanism in cold gas spraying. Acta materialia. (2003). Vol.51, No.15. 4379-4394

9 Moridi A., Hassani-Gangaraj S.M., Guagliano M., Dao M. Cold spray coating: review of material systems and future perspectives. *Surface Engineering*. (2014). Vol.30, No.6. P.369–395

10 Yin S., Cavaliere P., Aldwell B., Jenkins R., Liao H., Li W., Lupoi R. Cold spray additive manufacturing and repair: fundamentals and applications. *Additive Manufacturing*. (2018). Vol.19. 628-650

11 Irissou É., Legoux J.-G., Ryabinin A.N., Jodoin B., Moreau C. Review on cold spray process and technology: Part I - Intellectual property. *Journal of Thermal Spray Technology*. (2008). Vol.17, No.4. 495-516

12 Pattison J., Celotto S., Morgan R., Bray M., O'Neill W. Cold gas dynamic manufacturing: a non-thermal approach to freeform fabrication. *International Journal of Machine Tools and Manufacture*. (2007). Vol.47, No.3-4. 627-634

13 Dykhuizen RC, Smith MF Gas dynamic principles of cold spray. *Journal of Thermal Spray Technology*. 1998. Vol.7, No.2. 205-212

14 Gilmore DL, Dykhuizen RC, Neiser RA, Smith MF, Roemer TJ Particle velocity and deposition efficiency in the cold spray process. *Journal of Thermal Spray Technology*. (1999). Vol.8, No.4. 576–582

15 Stoltenhoff T., Kreye H., Richter H.J. An analysis of the cold spray process and its coatings. *Journal of Thermal Spray Technology*. (2002). Vol.11, No.4. 542-550

16 Schmidt T., Gärtner F., Assadi H., Kreye H. Development of a generalized parameter window for cold spray deposition. *Acta materialia*. (2006). Vol.54, No.3. 729-742

17 Grujicic M., Zhao CL, DeRosset WS, Helfritch DJ Adiabatic shear instability-based mechanism for particle bonding in the cold-gas dynamic-spray process. *Applied Surface Science*. (2003). Vol.219, No.3-4. 211-227

18 Meng XM, Zhang JB, Liang YL, Han W., Zhao J. Effect of gas temperature on deposition behavior in cold spray. *Surface and Coatings Technology*. (2008). Vol.202, No.18. 4470-4477

19 Yu T., Chen M., Wu Z. Experimental and numerical study of deposition mechanisms for cold spray additive manufacturing process. *Chinese Journal of Aeronautics*. (2022). Vol. 35, No. 2. 276-290

20 Li W.-Y., Zhang C., Guo XP, Zhang G., Liao HL, Coddet C. Deposition characteristics of Al-12Si alloy coating fabricated by cold spraying with relatively large powder particles. *Applied Surface Science*. (2007). Vol. 253, No. 17. 7124-7130

21 Wang, N.; Liu, C.; Wang, Y.; Chen, H.; Chu, X.; Gao, J Effect of process parameters on properties of cold-sprayed Zn-Al composite coatings. *Materials* (2022), 15, 7007

22 Wang, K.; Wang, S.; Xiong, T.; Wen, D.; Wang, G.; Liu, W.; Du, H. Protective performance of $ZnAlMgTiO_2$ coating prepared by cold spraying on marine steel equipment. *Coatings* (2019), 9, 339

AUTHORS' INFORMATION

Berikkhan Kaiyrzhan - PhD student in Technical Physics, Engineering Center, Shakarim University, Semey, Kazakhstan; ORCID: 0009-0009-2788-062X; (e-mail: k.berikkhan@shakarim.kz)

Satbayeva Zarina - Professor - researcher at the Department of Technical Physics and Thermal Engineering, Shakarim University, Semey, Kazakhstan; ORCID: 0000-0001-7161-2686; (e-mail: satbaeva.z@mail.ru)

Zhassulan Ainur - PhD student in Technical Physics, Senior Researcher, Engineering Center, Shakarim University, Semey, Kazakhstan; ORCID: 0000-0001-5166-4761; (e-mail: a.zhassulan@shakarim.kz)

Shynarbek Aibek - PhD student in Technological Machines and Equipment, Engineering Center, Shakarim University, Semey, Kazakhstan; ORCID: 0009-0001-5887-0135; (e-mail: a.shynarbek@shakarim.kz)

Ormanbekov Kuanysh - PhD student in Technological Machines and Equipment,Engineering center,University name Shakarima,Semey,Kazakhstan; ORCID: 0000-0001-6099-2812; (e-mail: k.ormanbekov@shakarim.kz)

ORIGINAL STUDY

CURRENT PROBLEMS OF EQUIPMENT WEAR IN THE MINING, OIL AND GAS, AND AGRICULTURAL INDUSTRIES

Yedilzhan Kambarov [1], Nurmakhanbet Raisov[1*], Aibek Alibekov[1], Gulim Tleubergenova[1]

[1]Research Center "Surface Engineering and Tribology", Sarsen Amanzholov East Kazakhstan University, Ust-Kamenogorsk, Kazakhstan
*Corresponding author: nurmakhanbetraisov@gmail.com

Abstract. *The article provides an overview of current issues related to equipment wear in the mining, oil and gas, and agricultural industries, and analyses the latest technologies for strengthening and restoring the surfaces of working parts. It examines the main types of mechanical and corrosion wear, typical components subject to premature failure, and the economic consequences of failures. Particular attention is paid to advanced surface treatment methods: laser and plasma hardening, gas-thermal and electric arc spraying, as well as new coatings based on nanomaterials and high-entropy alloys. A comparison of technologies is made based on key parameters (adhesion strength, particle temperature, productivity). The need to introduce multifunctional protective coatings with anti-friction and corrosion-resistant properties to increase the reliability and service life of equipment in aggressive operating conditions is emphasised.*

Keywords: Equipment wear and tear. mining industry, oil and gas industry, agricultural industry, strengthening and restoration technologies, modern coatings.

1. Introduction

The continuous improvement of the performance characteristics of modern machinery and equipment, associated with increased power and productivity, can only be achieved through the corresponding improvement of the operational characteristics of their main components and parts. This problem is most relevant for industries such as mechanical engineering, mining and metallurgy, agriculture, and oil, where equipment operates under difficult conditions of high temperatures and loads, as well as corrosive environments. Therefore, the improvement of surface hardening technologies is an important and relevant task for surface engineering, a new direction in materials science.

The widespread use of coatings for strengthening and restoring industrial parts is often limited by a lack of information about the possibilities and methods of applying coatings, their advantages and disadvantages, the requirements for equipment, and the selection of parts for coating. The feasibility of applying coating technology depends on the degree of complexity of its implementation and the economic efficiency of applying coatings in each industrial field.

Wear and tear of mining and metallurgical equipment parts. Wear and tear of mining and metallurgical complex equipment is a pressing issue that requires careful consideration using scientific and technical approaches based on the application of new technologies and materials for equipment repair, restoration and strengthening of parts at minimal cost. To comprehensively address these issues, it is necessary to analyse the methods currently used to restore parts in production conditions and the possibility of improving the technological and operational properties of equipment using promising materials and technologies. Today, the level of wear and tear of fixed assets in the country's mining industry is 63.8% [1].

The paper [2] presents calculations of global energy consumption due to friction and wear in the mining industry. A wide range of mining equipment used for extraction, transportation and enrichment in underground, open-pit mining and mineral processing was analysed. Total energy consumption in global mining activities, including the extraction of minerals and rocks, is estimated at 6.2% of total global energy consumption. About 40% of the energy consumed in mineral extraction (equivalent to 4.6 EJ annually on a global scale) is used to overcome friction. In addition, 2 EJ is used to repair and replace worn parts, as well as to stockpile and replenish spare parts and equipment needed in case of breakdowns due to wear and tear. The most energy-intensive mining operations are crushing (32%), transportation (24%), ventilation (9%) and digging (8%).

Received 5 August 2025; revised 17 December 2025; accepted 5 January 2026.

(https:doi.org/……)

One of the main problems associated with the short service life of mining and metallurgical equipment parts is intensive wear due to operation in aggressive environments, abrasive and hydroabrasive wear. According to research, more than 50% of the total volume of worn parts in the mining and metallurgical industry are rotating parts (shafts, bushings, bearing rings), and for various technological equipment, their wear is in the range of 0.1-1.5 mm [3]. Fracture, corrosion, wear and deformation are typical types of shaft failure. Among them, the predominant mechanism is fatigue failure, caused primarily by the effects of cyclic loads experienced by shafts during regular operation [4].

Rock crushing is the first mechanical grinding process after drilling and blasting in rock crushing. Equipment used in rock crushing processes, such as armour plates, armour cones, linings, beaters, hammers and hammer blades, is at high risk of premature wear. Premature wear of hammers causes the crushing process to stop after just one week of operation [5].

Drilling operations in quarries are the most labour-intensive process in mineral extraction technology. The most widespread method in open-pit mining (up to 82.5%) is roller cone drilling, with auger drilling accounting for about 17.5%, percussion-rotary drilling for up to 1%, and the remaining 0.8% for thermal and percussion-rope methods [6]. Three main types of drilling tools are used for drilling rock: roller cone bits, percussion drill bits and cutting bits. The ratio of different drilling methods depends on many factors (mining, economic), but mainly on the mining and geological conditions and the strength coefficient of the rock. Depending on geological conditions, the service life of rock-breaking tools can reach several hundred metres or more, and the average mechanical drilling speed is about 20-40 m/h [7]. Areas for improvement of rock-breaking tools include: increasing wear resistance, strength and thermal conductivity and, as a result, performance.

In mining operations, the service life of excavator equipment used in mining and tunnelling projects, as well as in oil and gas drilling, largely depends on the abrasiveness of the soil. In addition, underground mines contain CH4, CO, CO2, H2S, and SO2 in the air, and equipment parts operating in such an environment will be subject to both erosion and corrosion. The performance of tunnel boring machines (TBMs) is greatly affected by the wear of various parts, including disc cutters, expanders, bits, and facing plates [8]. Disc cutters with insert teeth are among the most commonly used cutters in TBMs. It should be noted that most studies focus primarily on the wear mechanisms of conventional disc cutters (dome-shaped and flat cutters). However, the teeth and body of disc cutters actually wear differently. The main mechanisms of wear of carbide teeth are abrasive wear, fatigue wear and adhesive wear, manifested in the form of pits and scratches formed by the penetration of solid rock particles during sliding. In contrast, the main mechanisms of wear on the cutter base are mainly abrasive wear and adhesive wear, characterised by numerous grooves formed as a result of rock particles sliding along the cutter base [9]. An analysis of failed disc cutters revealed that 53% of the alloy teeth failed, with breakage and chipping accounting for the highest proportions - 37% and 15%, respectively, Fig. 1.

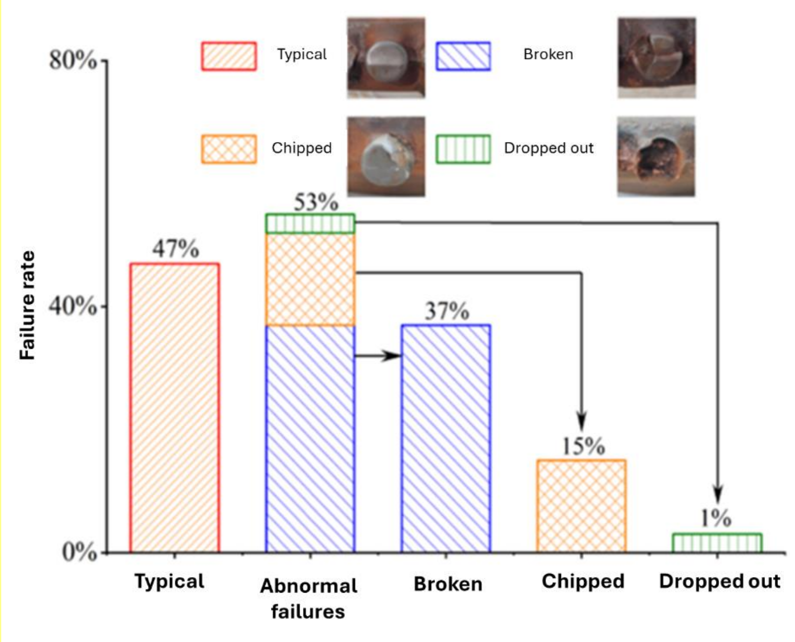

Fig. 1. Statistical distribution of each type of failure of disc cutters [9].

Wear and tear of oil and gas equipment parts. Centrifugal slurry pumps are widely used in various industrial production processes, including agricultural irrigation, deep-sea mining, oil extraction, molten salt energy storage, etc. In deep-sea mining, one of the serious technical problems is the destruction of the flow components of centrifugal slurry pumps due to erosion wear caused by the impact of solid particles [10]. In slurry pumps, the following elements are subject to the most intense wear: the front edge of the impeller blade inlet; the rear edge of the outlet of the impeller discharge surface; the spiral tongue (volute protrusion) of the pump casing, Fig. 2 [11].

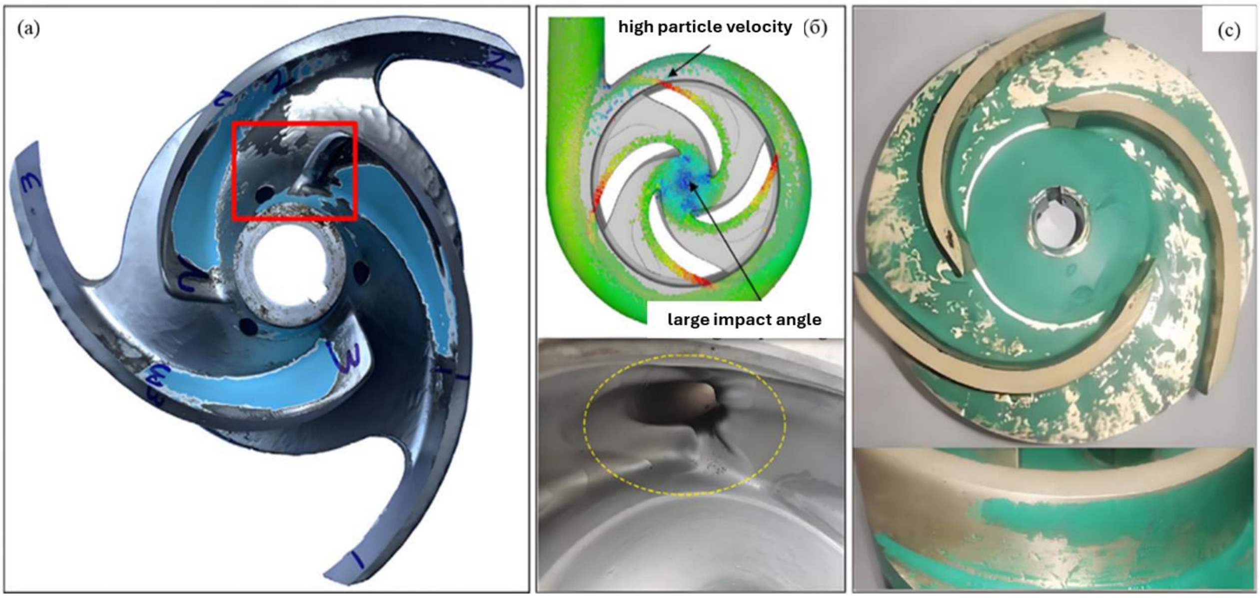

Fig. 2. Distribution of wear on a slurry pump: a) front edge of the blade; b) spiral tongue; c) rear edge of the blade [11].

In the oil and gas industry, the operational reliability and cost-effectiveness of the extraction, transportation and processing of hydrocarbon raw materials are determined by technologically advanced and fail-safe shut-off valves, which are subject to fairly high requirements: ensuring instant localisation of possible accidents, safety of technological systems in a wide range of operating environments, pressures, temperatures, and environmental conditions (seismic impact, humidity, low and high temperatures, etc.). Today, the following main types of shut-off valves have been developed and are widely used: valves, gate valves, butterfly valves and ball valves [12]. Gate valves have a number of advantages over other shut-off devices, including: simplicity of design, small dimensions, favourable cost characteristics and the ability to operate in a wide variety of conditions. During the operation of gate valves, a number of problems arise related to wear and corrosion. More than 50% of gate valve failures are caused by the destruction of sealing surfaces, which is associated with intense corrosion and erosion wear. These processes lead to a loss of tightness, increased repair costs and, in some cases, critical equipment failures. A particularly dangerous situation occurs when the sealing surfaces seize, making it impossible for the shut-off valve to operate at critical moments, such as in emergency situations. The cost of repairing the valve varies from 30-50% of the total cost of repairing the gate valve, which makes this problem important from an economic point of view. Studies have shown that the most vulnerable parts of gate valves are the mating surfaces of the ‘seat’ and “gate” parts, as well as the ‘spindle’. These elements are most susceptible to wear due to constant friction, exposure to aggressive working environments and cyclic loads. As a result, their wear becomes the main cause of valve failures, and it becomes necessary to surface harden the mating surfaces of the ‘seat-gate’s assembly to increase its service life. Based on this, it is important to identify the main factors affecting the reliability of the gate valve and seat, as well as to develop recommendations for improving their reliability under high loads and intensive operation.

One of the key factors determining the stability of fuel and energy resources supply to the regions of our country is the degree of reliability of oil and gas equipment and pipelines. The main factor contributing to the reduction in the reliability of oil and gas equipment and pipelines is the impact on the metal of their inner surface of the hydrocarbon media being pumped and processed, which contain corrosive components. During operation, the throughput capacity of pipelines gradually decreases due to the accumulation of paraffin deposits, increased roughness of the pipe walls as a result of internal corrosion and the accumulation of corrosion products and mechanical impurities. The decrease in throughput capacity leads to a sharp decrease in the efficiency of pipelines and a significant increase in the cost of pumping oil-containing liquids.

It is worth noting that the technological tasks of Kazakhstan's oil and gas industry enterprises, presented on the official platforms of the Samgau Centre for Scientific and Technological Initiatives Fund [13] and the National Academy of Sciences under the President of the Republic of Kazakhstan [14], are also related to improving the efficiency of oil and gas pipelines: optimising existing methods of combating complications and introducing advanced technologies to minimise the impact of negative factors in hydrocarbon production, while searching for solutions (Task No. 16 of the Samgau Centre for Scientific and Technological Initiatives); studying the conditions for the formation of salt deposits on the inner walls of production pipelines at the field and methods of combating their formation (Task No. 24 of the Samgau

Scientific and Technical Information Centre); cleaning paraffin deposits in the wellbore and pipelines (Task No. 13 of the National Academy of Sciences of Kazakhstan).

The main reasons for the formation of salt, paraffin, bitumen and hydrate deposits on the internal surfaces of production pipelines and oil heating furnace coils are the characteristics of the composition of the oil being extracted. This includes a high content of mineral salts, paraffin and asphaltene-resinous substances, as well as the presence of free water and gas. For example, when the temperature and pressure decrease during oil transportation, paraffin crystallises, which reduces the efficiency of pipelines and increases operating costs [15]. Low temperatures, pressure changes, uneven flow and stagnant zones also contribute to the formation of deposits. The evaporation of formation water and an increase in its salinity due to a decrease in temperature and pressure lead to the precipitation of salts (e.g., NaCl, $CaCO_3$) in the wellbore, which causes the formation of salt deposits. To prevent these phenomena, it is recommended to use salt deposit inhibitors, depressant and stabilising additives, maintain a temperature above the paraffin precipitation point, use gas and water drainage systems, and regularly clean pipelines using mechanical and chemical methods [16-17]. These measures increase the efficiency of equipment and reduce the negative impact on the operational performance of oil and gas pipelines.

The efficiency of oil and gas pipelines can be improved by using polymer coatings that prevent the formation of paraffin deposits in pipelines. Polymer coatings are widely used in extreme conditions, including deep-water pipelines, due to their high resistance to mechanical stress, chemical exposure and thermal changes. In [18], there is a proposal to use various polymer coatings with low surface energy applied to the pipeline to improve anti-fouling properties and reduce paraffin deposits. The results of the influence of eight coatings, including polyvinylidene fluoride (PVDF), silicone rubber, methyl acrylate-styrene copolymer (MAS), polyurethane (PU) and epoxy resin (EP), on flow resistance and paraffin deposition prevention using a rotational viscometer and the cold spot method. The most effective coating was S1 (silicone rubber vulcanisation at room temperature), which demonstrated the maximum reduction in flow resistance (21.7%) at a temperature of 26.0 °C and the most effective prevention of paraffin deposits (74.7%). Minimal deposits are observed on pipes coated with ethylene tetrafluoroethylene (ETFE), which is due to their smooth surface and low surface interaction energy [19].

Current research is focused on developing bio-inspired materials and multifunctional coatings that improve mechanical properties and provide reliable protection for pipelines in challenging operating conditions [20-21]. The authors of [22] presented the development of a superhydrophobic coating made of fluorinated silica (F-SiO2) Polydimethylsiloxane (PDMS) with high corrosion resistance, which was obtained by two-stage spraying. The highlight of this work was the formation of a microstructure that can create air pockets to form an air layer at the apparent solid-liquid interface. As a result, the coatings demonstrated a high ability to resist the effects of corrosion. In [23], multifunctional superamphiphobic coatings were presented using a simple spraying method. Highly fluorinated Palygorskite SiO2 (Pal SiO2-F) composite fillers were produced by in-situ growth of SiO2 on the surface of palygorskite and its chemical modification. These fillers were integrated into polyethersulfone (PES) and poly (vinylidene fluoride-co-hexafluoropropylene) (PVDF-HFP), which allowed the formation of unique micro-/nano-hierarchical structures with multiple papillary elements and intertwined networks. A stable air film was formed on the surface of the PES-PVDF-HFP/SiO2-F coating thanks to the chemical inertness and high adhesion of the polymers, as well as carefully designed structures. This air film was used as an anti-adhesion layer and an effective thermal barrier, which gave the coating pronounced anti-adhesion properties in the crude oil system.

Another important task for Kazakhstan's oil and gas industry is to increase the service life of pump and compressor pipes (Task No. 15 of the National Academy of Sciences of Kazakhstan). The service life of pump and compressor pipes (PCP) is currently reduced to two months, which causes significant economic losses. Frequent well shutdowns are associated with PCP leaks caused by deformation of drill pipes during drilling and constant mechanical contact between the pipe and the wellbore walls and equipment, leading to accelerated wear of the coating, defects and the occurrence of pitting, crevice and underfilm corrosion. High mechanical stresses and constant friction cause premature wear even of the most wear-resistant epoxy coatings. Stress corrosion occurs, which in turn leads to corrosion fatigue cracking and failure of the drill pipe. To solve this problem, a Kazakhstani company planned to conduct pilot industrial tests (PIT) in 2024 using an internal polymer coating to protect tubing from corrosion and equipping threaded connections with stemer. The success of the PILT will be assessed according to the following criteria: uninterrupted operation of the subsea pumping equipment without tubing leaks during the tests and preservation of the integrity of the internal coating and threaded connections. An alternative solution is to inject corrosion inhibitors directly into the wellhead of the subsea pumping equipment, which also helps to increase the service life of the tubing. This problem is relevant for work in aggressive environments and directly affects the economic efficiency of production.

An analysis of scientific works aimed at solving these problems has been carried out, and an overview of existing methods for their implementation has been formulated. Work [24] considers the use of a nanoparticle anti-friction coating (NPAF) as an alternative to traditional copper coatings for oil casing couplings. Copper coatings are highly resistant to scuffing, but their use is limited due to economic and environmental constraints. The NPAF anti-friction coating was manufactured using nanoparticles of polytetrafluoroethylene (nano-PTFE), polyacrylic resin, and a high-concentration ethanol colloid of nanocopper. The nano-copper colloid, with a solid particle concentration of 14–20% and an average particle size of about 95 nm, was obtained by liquid-phase reduction. The NPAF coating was successfully applied to the surfaces of threaded couplings of oil casing pipes, where it demonstrated a significant reduction in friction and wear. The authors noted that NPAF coatings are a promising solution for improving the performance of threaded connections of oil casing pipes under difficult operating conditions.

The authors of [25] proposed a different way to improve the performance characteristics of threaded connections in petroleum drilling tools (PDT) using an anti-friction coating based on nanocopper (NaCU-AFC). The coating was made of nanocopper and an epoxy resin-based binder. Experimental results showed that the use of NaCU-AFC reduces torque by 35.66% and significantly increases resistance to galling, which extends the service life of PDT. Tightening analysis also demonstrated an increase in the average number of tightening cycles to 2.5, which is 76.05% more than in the control group. The NaCU-AFC coating showed a significant improvement in the anti-friction properties and scuffing resistance of PDT threaded connections, indicating its high potential for use in oil drilling. However, additional research is needed to confirm the practicality and reliability of the coating, including studies of its chemical resistance and durability.

Thus, based on an analysis of the scientific literature, it can be said that among the innovative approaches, the use of superhydrophilic/underwater superoleophobic coatings stands out, which demonstrate anti-adhesion properties in an aqueous environment, significantly increasing the effectiveness of combating wax deposits. However, it has been noted that such coatings are mechanically fragile and susceptible to damage in aggressive environments, which limits their practical application in the harsh conditions of oil production. Thus, a durable and multifunctional superamphiphobic coating can be developed and may become an excellent option for coatings with anti-adhesive and anti-fouling properties, with enormous potential for application in the petrochemical industry and other harsh conditions.

Wear and tear of agricultural machinery parts. The efficiency of agricultural production is largely determined by the level of technical support and the use of high-quality agricultural machinery. Repair and maintenance account for a significant share of costs, amounting to 12% or more of the cost of agricultural products [26]. According to Energyprom.kz data from 2 April 2020, the development of the agricultural machinery manufacturing industry is a pressing issue in Kazakhstan. Despite the growth in production and the efforts of manufacturers, according to data from the Statistics Committee of the Ministry of National Economy of the Republic of Kazakhstan for 2019, Kazakh companies covered only 12.8% of the demand for tractors for agriculture and forestry, and in the segment of ploughs and disc harrows, Kazakh companies covered only 3.5% of the demand for these devices [27]. The average wear and tear of the entire fleet of agricultural machinery in the Republic of Kazakhstan reached 76%.

In agricultural machinery, abrasive wear is probably the most significant cause of mechanical damage to equipment components that come into contact with abrasive bodies. Abrasive wear critically affects production planning, soil cultivation quality, and energy consumption in the soil cultivation process each time an action is performed, so determining the wear losses of soil cultivation implements is important [28]. During the operation of soil cultivation machines and units, working surfaces are subject to uneven wear, which reduces the service life of parts and increases the cost of their replacement and renewal. The working parts of soil cultivation equipment, such as ploughshares, wear out particularly quickly, with their service life varying between 5 and 20 hectares, depending on soil and climatic conditions [29]. Ploughshares made of L53 and 65G steel lose about 40-60% of their service life on heavy soils if hardened coatings are not used. The total service life of mower cutting segments when working in fields that meet the agricultural requirements for harvesting should be 3.5 hectares/unit on average. [30]. The working parts of other soil cultivation machines also have a limited service life: discs of hullers and disc harrows from 5 to 25 hectares, cultivator tines from 5 to 15 hectares [31].

Against the backdrop of the above statistics, there is a technological need to increase the production capacity of repair and technical enterprises by introducing new technological processes for strengthening agricultural machinery parts. Such approaches will significantly increase the durability and wear resistance of parts and reduce overall operating costs.

2. Materials used to strengthen parts operating under conditions of wear

Modern approaches to reducing friction and wear include the use of innovative materials with improved strength and wear resistance characteristics, advanced surface treatment methods, highly effective coatings, advanced lubricants and additives. In the mining industry, hammers were made of high-chromium cast iron, especially in the production of mineral fillers. Numerous studies confirm that high chromium white cast iron (HCWCI) is an indispensable material in conditions where excellent resistance to abrasive, erosive and impact wear is required [32-33]. High chromium white cast iron is a suitable material for functional components of crushing machines, which are widely used in mineral processing to increase wear resistance and extend equipment life at lower production costs. Such wear resistance characteristics of high-chromium cast iron (C-Cr-Fe) are due to the presence of a hard eutectic carbide of the M7C3 type embedded in the austenitic matrix, which after heat treatment can be completely or partially transformed into a martensitic matrix [34].

The priority direction in the development of drilling equipment is the improvement of rock-breaking tools. Many achievements in this area are associated with the use of modern superhard materials, the creation of new composite materials, and the development of drilling tool designs with combined armament. The cutter of a rock-breaking tool (such as PDC-polycrystalline diamond cutters) is obtained by sintering polycrystalline diamond powder on a substrate under very high temperatures and pressures (HTHP high-temperature, high-pressure method). In [35], it is reported that the introduction of graphene under unchanged conditions of sintering PDC cutters leads to an improvement in electrical conductivity by approximately 42 times, an increase in thermal conductivity by 60%, and an improvement in the hardness and wear resistance of the cutter by 75% and 33%, respectively.

For the extraction of hard rock, the cutting head of tunnel boring machines is mainly equipped with a set of disc cutters and bits with carbide tips. The main body of the tools is made of inexpensive grades of steel. Hard alloys or cemented carbides are a metal-ceramic composite material widely used in various industries. As a composite material, they consist of a hard phase, usually WC, and a plastic and durable binder phase. Since its introduction, cobalt Co has established itself as the most common binder phase metal due to its excellent properties [36]. Although alternative binder elements such as Ni and Fe have long been studied alongside Co, Co remains the preferred choice due to its superior properties: high hardness, impact toughness, lower sintering temperature, and excellent wettability of WC grains compared to other metals. However, in recent years, the partial or complete replacement of Co has become an important part of hard alloy research. Since Co is considered an essential raw material that plays a key role in battery technology, which has gained worldwide recognition thanks to the production of electric vehicles and portable computers, this has led to a steady increase in Co prices in recent years [37].

2.1 Main technologies for strengthening parts operating under wear conditions

Laser hardening is gradually becoming one of the most common methods of surface hardening in modern mechanical engineering. The laser hardening process is very efficient, as the phase transformation of hardening is completed within one second. In addition, deformation after laser hardening is very limited, which guarantees the dimensional accuracy of the processed parts. Furthermore, the environmentally friendly laser hardening process also allows for the processing of complex shapes, including thin-walled and hollow structures. In their work, Zhenyu Chen et al. (2023) showed that by optimising the parameters of the laser process, it is possible to significantly improve the hardness and wear resistance of QT700-2 malleable cast iron [38]. Of great interest is the hardening of hard alloys based on tungsten carbide cobalt WC-Co by laser radiation, after which the microhardness of the surface layer increases by 10-14 GPa [39]. In the work of Tomohisa Kanazawa et al. (2023), it was shown that after laser hardening, the durability of the gear increased 3.8 times compared to untreated gears [38]. In [39], laser cladding technology was used to obtain FZNCr-60A nickel alloy coatings on the surface of balancing plates of slurry pumps used in underground mining, made of 1045 steel (analogous to structural steel 45). Currently, laser cladding is widely used in the repair of machine parts due to its advantages, such as lower dilution rate, small heat-affected zone, and good metallurgical bond between the coating and the substrate [40].

In industry, plasma hardening is most widely used for strengthening parts of agricultural machinery, chemical, petrochemical, metallurgical and other production equipment. An analysis of the results of industrial use of plasma hardening technology has shown that the average operational durability of heat-treated rolls per campaign increases by 20-60%, the average operating time in terms of the amount of rolled metal increases by 30-100%, and the specific consumption (in tonnes per tonne of rolled metal) decreases by 20-50% [43]. Currently, plasma hardening is used in production to harden large-sized equipment parts, such as hot rolling rolls, locomotive wheel tyres, railway wheel sets, trolley wheels, and crane wheels. Hardening small and thin-walled parts with plasma hardening is not always effective due to the difficulty of achieving the cooling rate required for hardening. In exceptional cases, spray or flow cooling may be used.

Due to its technological simplicity and accessibility, combined with high quality of the restored surface, the gas-flame spraying method is widely used for hardening and restoring various machine and equipment parts. Gas flame spraying is widely used to restore parts of agricultural machinery, pump and compressor equipment, covers and shafts of electric motors, etc. This method is most commonly used in the repair of agricultural and automotive equipment, for surfacing drill bits and quickly wearing parts of mining equipment. Gas-flame spraying is primarily suitable for restoring parts that are not subject to significant dynamic loads. Such parts include body parts of tractors and automobiles, where the mounting seats are subject to wear (sockets of the block for main bearing inserts; sockets of gearbox crankcases; support flanges, cylinder sleeve seating belts; the surface of the lower connecting rod head, etc.). A significant range of products includes shafts made of cast iron, 45 steel, alloy steels, with worn seating areas (gearbox shafts, machine running gear, etc.). Gas-flame spraying is not very effective when processing small parts. This is due to the high consumption rate of filler material.

An analysis of modern technologies for restoring worn surfaces shows that in practice there is a need to restore surfaces worn to a thickness of up to 2 mm, giving them wear-resistant properties when subjected to friction using oils. There are a number of modern technologies and methods for restoring worn friction surfaces, which require special equipment and expensive materials. Along with this, the electric arc spraying process stands out as advantageous. Practically the only disadvantage of coatings applied by electric arc spraying is their low adhesive strength, especially when applying coatings thicker than 3 mm, which is a consequence of high internal residual stresses, different elasticity modules, and linear expansion coefficients of the base metal and coating. One option for increasing the adhesive strength of the bond, as discussed in the literature, is to apply an intermediate plastic layer. In [41], it is reported that electric arc spraying technology has been introduced at OAO Azovstal MK Azovstal" to restore worn parts of metallurgical equipment, such as continuous casting machine roller necks, hydraulic cylinder pistons, etc. Due to their porosity and ability to retain lubricant, the sprayed coatings have shown improved performance, which has reduced the downtime of the repaired equipment.

Currently, supersonic gas-flame spraying methods (HVOF, HVAF) are becoming increasingly widespread. The velocity of the heated gas jet at the burner nozzle reaches 1700-2700 m/s, which allows for the creation of unique coatings with a bond strength of up to 100 MPa [35]. The porosity of the coating is 0.5% and is similar in its characteristics to coatings obtained by detonation spraying. In the work of Payank Patel et al. (2024) studied the potential of high-entropy AlCoCrFeMo alloys for new-generation tribological interfaces obtained by three methods, namely low-pressure cold spraying (LPCS), flame spraying (FS) and high-velocity oxygen-fuel spraying (HVOF) [35]. HVOF coatings showed higher hardness values compared to FS and LPCS coatings, which can be explained by their fine-grained microstructure, lower porosity and oxide inclusions compared to the other two coatings. A number of studies [38-39] have concluded that the HVAF method is effective for producing carbide-based coatings (WC-17Co, Cr3C2), since the use of compressed air results in a lower spraying temperature and, consequently, less carbide decomposition.

The advantage of the electric arc spraying (metallisation) method is the high productivity of the process and the possibility of significantly reducing the time required for spraying. For example, at a current of up to 700 A, a steel coating can be sprayed at a rate of 30-35 kg/h, which is several times higher than the productivity of gas-flame spraying. Electric arc spraying is used to restore the following parts: engine crankshafts, brake drums, brake discs, clutch discs, cylinder heads, engine connecting rods, cylinder liners, rotor shafts and electric motor starters, cylinder blocks, etc. Metallisation is used to apply an anti-friction layer of lead and aluminium, zinc and aluminium, or bronze to bushings and bearings. Recently, electric arc spraying has come to be used in several industries as the most suitable and effective method of protecting high-performance equipment, such as boiler tubes, from corrosion, thanks to its economic benefits in terms of maintenance and production [38]. The widespread introduction of the electric arc metallisation process is hampered by the lack of systematic solutions to prevent the burnout of alloying elements from the metal and reduce the oxide content in the coating. Royanov V.A. et al. (2019) proposed using a pulsed air supply by introducing an additional element into the spray head of the arc metalliser in order to reduce the oxidative effect of the air spray jet on the liquid metal of the electrode ends [41]. Thus, despite the extensive research carried out on electric arc spraying, some problems remain unresolved, such as the speed and oxidation of dispersed metal in a heterophase flow, etc.

In fact, air plasma spraying is a diffusion metallisation process that allows for the effective formation of protective coatings and the restoration of worn parts of metal products. Plasma spraying has a number of advantages over gas-flame and arc spraying: it allows coatings to be applied from a wide range of materials; the use of inert gases that do not contain oxygen in plasmatrons helps to reduce the oxidation of the sprayed material and the surface of the part; coatings obtained by plasma spraying are superior in physical and mechanical properties to coatings obtained by gas-flame and arc spraying. Plasma spraying has a high energy density, and particles can reach high temperatures and speeds, which allows many refractory materials to be melted [39-40]. The authors of [41], after searching the Web of Science database for keywords related to plasma spraying and analysing articles published on this topic over the past 20 years, report that air-plasma spraying is mainly used to obtain wear-resistant coatings.

Table 1 presents a structured comparative analysis of modern strengthening technologies that are actively used in industrial production to increase the wear resistance and durability of parts and structures. These data allow us to assess the suitability of technologies for various industries and propose optimal solutions for specific operating conditions.

Table 1. Characteristics of surface treatment and coating technologies.

Technology	Particle velocity of material, m/s	Plant capacity, kg/h	Spray material utilisation ratio	Adhesion strength to substrate, MPa	Temperature of material particles, °C	Reference
1	2	3	4	5	6	7
Detonation spraying	350-1000	0,1-6	0,3-0,6	up to 200	up to 3000	[54-55]
High-velocity air-fuel spraying (HVAF)	300-600	5-10	0,6-0,8	50-100	up to 1500	[56]
High-velocity oxygen fuel spraying (HVOF)	400-900	5-20	0,5-0,7	80-150	up to 2000	[57]
Plasma spraying	50-400	0,5-8	0,7-0,9	up to 60	up to 4000	[58]
Gas flame spraying	до 300	До 2	-	up to 30	2500	[59]
Laser cladding	-	0,5-12	0,8-0,95	100-200	up to 3000	[60]
Plasma powder cladding	-	До 25	85	80-300	up to 2000	[61]
Physical vapour deposition (PVD)	-	1-10	-	30-60	200 - 500	[62]
Magnetron spraying	200	300	30–50	50–100	500–800	[63]

Thus, the development and implementation of resource-saving technologies for the restoration and strengthening of equipment parts is one of the pressing issues that has not yet been fully resolved for the Kazakh market. The widespread use of wear-resistant coatings for strengthening and restoring parts in industry is often limited by a lack of information about the possibilities and methods of applying coatings, their advantages and disadvantages.

3. Conclusion

An analysis of current equipment wear problems in key industries has shown that increasing the service life and reliability of machines is only possible with a comprehensive approach to the selection of materials and surface hardening technologies. The parts most susceptible to wear are those operating under intense mechanical, abrasive and corrosive loads: shafts, sealing elements, ploughshares, discs, cutting tools and pump working parts. Among the effective methods of restoration and protection, the most promising are laser and plasma treatment technologies, electric arc and detonation spraying, HVOF/HVAF methods, as well as the use of innovative coatings based on nanocomposites, high-entropy alloys and polymer matrices. Their correct application can significantly increase the service life of components and assemblies, reduce maintenance costs and equipment downtime. In the context of growing demands for reliability and economic efficiency, the integration of resource-saving strengthening technologies, taking into account the specific operating conditions and economic factors of a particular industry, is becoming a key area of development.

Funding

This research is funded by the Science Committee of the Ministry of Science and Higher Education of the Republic of Kazakhstan (Grant No. BR24992876).

Conflict of interest

The authors declare no conflict of interest.

References

1 *Extreme levels of equipment wear and tear are observed in Kazakhstan's mining industry*. [in Russian]. Available at: https://liter.kz/ekstremalnyi-uroven-iznosa-oborudovaniia-nabliudaetsia-v-gornodobyvaiushchei-otrasli-kazakhstana-1691023528/ (Oct10, 2024)

2 Holmberg K., Kivikyto-Reponen P., Harkisaari P., Valtonen K., Erdemir A. (2017) Global energy consumption due to friction and wear in the mining industry. *Tribology International*. 115. 116-139. DOI: https://doi.org/10.1016/j.triboint.2017.05.010

3 Ergashev M., Yakubov L.E., Sa"dullaev Z.Sh., Komilov I.R. (2024) Status and prospects of repair work to restore worn parts of mining and metallurgical equipment [in Russian]. *Universum: technical sciences.* 5(122). 59-64

4 Hou N., Ding N., Qu S., Guo W., Liu L., Xu N., Tian L., Xu H., Chen X., Zairi F., Lawrence W., C.-M. (2022) Failure modes, mechanisms and causes of shafts in mechanical equipment. *Engineering Failure Analysis*. 136(2). 106216. DOI: https://doi.org/10.1016/j.engfailanal.2022.106216

5 Kallel M., Zouch F., Antar Z., Bahri A., Elleuch Kh. (2017) Hammer premature wear in mineral crushing process. *Tribology International*. 115. 493-505. DOI: https://doi.org/10.1016/j.triboint.2017.06.025

6 Neskormnyh V.V., Liu B., Chzhaoran Ch., Petenev P.G., Popova M.S., Golovechenko A.E. (2021) Current trends in the improvement of PDC drilling tools. *Izvestiya Tomskogo politekhnicheskogo universiteta. Inzhiniring georesursov*. 332(5). 60-69. DOI: https://doi.org/10.18799/24131830/2021/05/3186

7 Abu Bakar M.Z., Majeed Y., Rashid M.A., Ahmed F. (2021) Wear mechanisms of LCPC rock abrasivity test impellers of materials equivalent to TBM cutter head face tools. *Tunnelling and Underground Space Technology*. 116. 104122. DOI: https://doi.org/10.1016/j.tust.2021.104122

8 Li X., Zhang M., Mo J. (2024) Wear and abnormal fracture failure mechanisms of alloy teeth in TBM insert tooth disc cutters. *Engineering Failure Analysis*. 167(3). 109051. DOI: https://doi.org/10.1016/j.engfailanal.2024.109051

9 Cheng W., Fan H., Cheng W., Chunlei Sh. (2024) Investigation on wear induced by solid-liquid two-phase flow in a centrifugal pump based on EDEM-Fluent coupling method. *Flow Measurement and Instrumentation*. 96 (3). 102542

10 Duan A., Lin Z., Chen D., Li Y. (2024) A review on the hydraulic performance and erosion wear characteristic of the centrifugal slurry pump. *Particuology*. 95. 370-392. DOI: https://doi.org/10.1016/j.partic.2024.10.006

11 Mirgorodskij S.I., Seraya N.V., Denisova O.K., Mirgorodskij L.S. (2018) Improvement of the manufacturing process and increase in wear resistance of shut-off valves for the oil and gas industry [in Russian].Vestnik Vostochno-Kazahstanskogo Gosudarstvennogo Tekhnicheskogo Universiteta Im. D. Serikbaeva. 4. 151-157

12 Samgau. Technological challenges. [in Russian]. Available at: https://www.csti.kz/ru/projects-ru/ (Nov 1, 2024)

13 National Academy of Sciences under the President of the Republic of Kazakhstan. Technological challenges facing enterprises. [in Russian]. Available at: https://ru.qazscience.gov.kz/science-kazakhstan/foresight-research/technological-tasks-enterprises/ (Nov 1, 2024)

14 Elkatory M.R., Soliman E.A., Nemr A.E., Hassan M.A., Ragab S., El-Nemr M.A., Pantaleo A. (2022) Mitigation and Remediation Technologies of Waxy Crude Oils' Deposition within Transportation Pipelines: A Review. *Polymers*. 14(16). 3231. DOI: https://doi.org/10.3390/polym14163231

15 Zhao D., Zhao Y., Zhong R., Yao L., Liang G. (2021) Analysis of the Influence of Wax Precipitation and Paraffin Control Technology on Environmental Protection // *Sustainable Development of Water and Environment*. 65-75

16 Obot I.B. (2021) Under Deposit Corrosion on Steel Pipeline Surfaces: Mechanism, Mitigation and Current Challenges *Journal of Bio- and Tribo-Corrosion*. 7. 49. DOI: https://doi.org/10.1007/s40735-021-00485-9

17 Zhang X., Tian J., Wang L., Zhou Zh. (2002) Wettability effect of coatings on drag reduction and paraffin deposition prevention in oil. *Journal of Petroleum Science and Engineering*. 36(1-2). 87-95. DOI: https://doi.org/10.1016/S0920-4105(02)00267-X

18 Bagdat M., Masoud R. (2015) Control of Paraffin Deposition in Production Operation by Using Ethylene–TetraFluoroEthylene (ETFE). *ICIPEG 2014*. 13-22. DOI: https://doi.org/10.1007/978-981-287-368-2_2

19 Bai J., Wu J-T. (2019) Multifunctional anti wax coatings for parafn control in oil pipelines. *Petroleum Science*. - 2019. - Vol. 16. - P. 619-631. DOI: https://doi.org/10.1007/s12182-019-0309-7

20 Varley R.J., Leong K.H. (2016) Polymer Coatings for Oilfield Pipelines. *Active Protective Coatings*. 233. 385-428. DOI: https://doi.org/10.1007/978-94-017-7540-3_14

21 Shen Y., Li K., Chen H., Wu Z., Wang Z. (2021) Superhydrophobic F-SiO2@PDMS composite coatings prepared by a two-step spraying method for the interface erosion mechanism and anti-corrosive applications. *Chemical Engineering Journal*. 413(1). 127455. DOI: https://doi.org/10.1016/j.cej.2020.127455

22 Peng J., Yuan S., Geng H., Zhang X., Zhang M., Xu F., Lin D., Gao Y., Wang H. (2022) Robust and multifunctional superamphiphobic coating toward effective anti-adhesion. *Chemical Engineering Journal*. 428. 131162. DOI: https://doi.org/10.1016/j.cej.2021.131162

23 Meng Z., Li Y., Yang Y., Xu Z-Q., Shi B., Zhao S-L. (2015) Effect of a nanoparticulate anti-friction coating on galling resistance of threaded oil-casing couplings // Journal of Petroleum Science and Engineering. 140-144. DOI: https://doi.org/10.1016/j.petrol.2015.02.008

24 Hongbo L., Yulin Z., Guanqi Z., Zechao W., Bo L. (2024) Finite element stress analysis of nano copper-based anti-friction coating for improved threaded connections in petroleum drilling tools. American Scientific Publishers. 14 (6). 892-899. DOI: https://doi.org/10.1166/mex.2024.2698

25 Website of LLP «ENERGYPROM.KZ» [in Russian]. Available at: https://www.energyprom.kz/ru/a/reviews/park-selhoztehniki-v-rk-moralno-ustarel-3-iz-4-selskohozyajstvennyh-mashin-starshe-10-let (Nov 19 2024)

26 Yazici A. (2011) Wear behavior of carbonitride treated ploughshares produced from 30MnB5 steel for soil tillage applications//Metal Science and Heat Treatment. - 2011. - Vol.53 (5 - 6). - P. 248 - 253. DOI: https://doi:10.1007/s110410119377z

27 Qi X., Jia Z., Yang Q., Yang Y. (2011) Effects of vanadium additive on structure property and tribological performance of high chromium cast iron hardfacing metal. *Surface and Coatings Technology*. 205(23-24). 5510-5514. DOI: https://doi.org/10.1016/j.surfcoat.2011.06.027

28 Kazdal Zeytin H., Yildirim H., Berme B., Duduoĝlu S., Kazdal G., Deniz A. (2018) Effect of boron and heat treatment on mechanical properties of white cast iron for mining application. *Journal of Iron and Steel Research International*. 18. P. 31-39. DOI: https://doi.org/10.1016/S1006-706X(11)60114-3

29 Neskoromnyh V.V., Baochang L., Chen Ch., Petenev P.G., Popova M.S., Golovchenko A.E. (2021) Current trends in the improvement of PDC drilling tools. *Izvestiya Tomskogo politekhnicheskogo universiteta. Inzhiniring georesursov*. 332(5). 60-69. DOI: https://doi.org/10.18799/24131830/2021/05/3186

30 Sapate S., Ramarao A. (2006) Erosive wear behaviour of weld hardfacing high chromium cast irons: effect of erodent particles. *Tribology International*. 39(3). 206-212. [in Russian] DOI: https://doi.org/10.1016/j.triboint.2004.10.013

31 Savinova E., Evans C., Lèbre É., Stringer M., Azadi M., Valenta R.K. (2023) Will global cobalt supply meet demand? The geological, mineral processing, production and geographic risk profile of cobalt. *Resources, Conservation and Recycling*. 190. 106855. DOI: https://doi.org/10.1016/j.resconrec.2022.106855

32 Chen Zh., Yu X., Ding N., Cong J., Sun J., Jia Q., Wang Ch. (2023) Wear resistance enhancement of QT700-2 ductile iron crankshaft processed by laser hardening. *Optics and Laser Technology*. 164. 109519. DOI: https://doi.org/10.1016/j.optlastec.2023.109519

33 Kanazawa T., Hayakawa M., Vinas D., Tahara Y., Hata N., Yoshimoto M. (2023) Sustainable technology for remanufacturing of carburized steels by laser hardening. *Journal of materials research and technology*. 24. 39-48. DOI: https://doi.org/10.1016/j.jmrt.2023.02.226

34 Wang P., Yang Y., Ding G., Qu J., Shao H. (1997) Laser cladding coating against erosion-corrosion wear and its application to mining machine parts. *Wear*. 209 (1-2). 96–100. DOI: https://doi.org/10.1016/S0043-1648(97)00018-5

35 Zhu L., Xue P., Lan Q., Meng G., Ren Y., Yang Zh., Xu P., Liu Z. (2021) Recent research and development status of laser cladding: A review. *Optics & Laser Technology*. 138. 106915. DOI: https://doi.org/10.1016/j.optlastec.2021.106915

36 Zaharov S.V., Royanov V.A., Serenko A.N. (2003) Restoration of metallurgical equipment parts by electric arc spraying. Bulletin of the Priazovsk State Technical University. Series: Technical Sciences. 13. 171-175

37 Patel P., Nair R.B., Supekar R., McDonald R., Chromik R.R., Moreau Ch., Stoyanov P. (2024) Enhanced wear resistance of AlCoCrFeMo high entropy coatings (HECs) through various thermal spray techniques. *Surface and Coatings Technology*. 477. 130311. DOI: https://doi.org/10.1016/j.surfcoat.2023.130311

38 Myalska-Głowacka H., Bolelli G., Lusvarghi L., Cios G., Godzierz M., Talaniuk V., (2024) Influence of nano-sized WC addition on the microstructure, residual stress, and tribological properties of WC-Co HVAF-sprayed coatings. *Surface and Coatings Technology*. 482. 130696. DOI: https://doi.org/10.1016/j.surfcoat.2024.130696

39 Alroy R.J., Kamaraj M., Sivakumar G. (2022) HVAF vs oxygenated HVAF spraying: Fundamental understanding to optimize Cr3C2-NiCr coatings for elevated temperature erosion resistant applications. Journal of Materials Processing Technology. 309. 117735. DOI: https://doi.org/10.1016/j.jmatprotec.2022.117735

40 Kumar S., Kumar M., Handa A. Comparative study of high temperature oxidation behavior and mechanical properties of wire arc sprayed Ni Cr and Ni Al coatings. *Engineering Failure Analysis*. - 2019. 106. 104173. DOI: https://doi.org/10.1016/j.engfailanal.2019.104173

41 Royanov V.A., Zaharova I.V., Kryuchkov N.S., Pugachev E.V. (2019) Reducing the impact of oxygen on the liquid metal of electrodes during electric arc spraying with a pulsating air spray jet. *World Science*. 5(45). 13-21. [in Russian] DOI: https://dx.doi.org/10.31435/rsglobal_ws/31052019/6508

AUTHORS' INFORMATION

Yedilzhan Kambarov - researcher of Scientific Research Center "Surface Engineering and Tribology" at Sarsen Amanzholov East Kazakhstan University, Ust-Kamenogorsk, Kazakhstan; (e-mail: anabioldina@vku.edu.kz), SCOPUS Author ID: 57947088900, ORCID iD: 0000-0002-0838-6724

Raisov Nurmakhanbet - junior researcher of Scientific Research Center "Surface Engineering and Tribology" at Sarsen Amanzholov East Kazakhstan University, Ust-Kamenogorsk, Kazakhstan; (e-mail: nurmakhanbetraisov@gmail.com), ORCID iD: 0009-0007-1698-957X

Aibek Alibekov - engineer of Scientific Research Center "Surface Engineering and Tribology" at Sarsen Amanzholov East Kazakhstan University, Ust-Kamenogorsk, Kazakhstan; (e-mail: aibek.alibekov.03@mail.ru), ORCID iD: 0000-0002-0838-6724

Gulim Tleubergenova - engineer of Scientific Research Center "Surface Engineering and Tribology" at Sarsen Amanzholov East Kazakhstan University, Ust-Kamenogorsk, Kazakhstan; (e-mail: gulh7748@gmail.com), ORCID iD 0009-0009-4064-5368

REVIEW ARTICLE

SPINEL-BASED MATERIALS FOR HIGH-PERFORMANCE SUPERCAPACITORS - A REVIEW ARTICLE

Zhangabay Turar[1], Ali Coruh[1], Arystanbek Kussainov[2], Rakhmetova Mairagul[3]

[1]Department of Physics, Sakarya University, Sakarya, Turkey;
[2]Protectivie and Functional Coatings Scientific Center, Daulet Serikbayev East Kazakhstan Technical University Ust-Kamenogorsk, Kazakhstan;
[3]Department of Plasma Physics and Computer Physics, Al-Farabi Kazakh National University, Almaty, Kazakhstan/ Department of Physics and Technical disciplines, Kh. Dosmukhamedov Atyrau University, Atyrau, Kazakhstan;
*Corresponding author: zhangabay.turar@ogr.sakarya.edu.tr

Abstract. *Spinel metal oxides (general formula* AB_2O_4*) have received strong research attention as electrode materials for supercapacitors because of their rich redox activity, stable structure, and low cost [1]. Their unique crystal arrangement, where metal ions sit in tetrahedral and octahedral sites, allows easy tuning of electrical, magnetic, and electrochemical behavior. In recent years, many spinels such as* $NiCo_2O_4$*,* $MnCo_2O_4$*,* $ZnFe_2O_4$*,* Co_3O_4*,* $FeCo_2O_4$*, and high-entropy spinels have been studied for fast charge storage. Researchers have shown that controlling the synthesis method, morphology, porosity, and particle size can significantly improve their capacitance, cycling stability, and rate performance. Spinel-carbon composites, conducting polymer hybrids, and asymmetric devices further enhance practical device performance. However, challenges remain, including moderate conductivity, structural degradation during cycling, and difficulties in achieving high mass loading for real devices [2]. This review summarizes the fundamentals of spinel structure, recent progress in synthesis and nanostructure design, electrochemical mechanisms, device-level performance, challenges, and future directions. The goal is to provide a clear and practical understanding of how spinels can contribute to next-generation, high-efficiency.*

Keywords: spinel oxides; supercapacitors; pseudocapacitive materials; nanostructured electrodes; energy storage review.

1. Introduction

The global demand for efficient energy storage technologies is rapidly increasing as renewable energy deployment, electric transportation, and portable electronics continue to expand worldwide [3]. Renewable sources such as solar and wind are clean but intermittent, meaning that harvested energy must be stored and supplied on demand to maintain grid stability and efficiency. Likewise, electric vehicles require energy-storage devices that can rapidly charge and release energy, delivering high power during acceleration and regenerative braking. In this context, supercapacitors, also called electrochemical capacitors, have emerged as highly promising devices because they store and release charge through fast surface redox reactions and rapid ion transport rather than slow bulk chemical processes typical of batteries. As a result, supercapacitors offer exceptional features including extremely high power density, fast charge-discharge capability, outstanding cycling stability, long operational life, and inherent safety, making them suitable for applications such as hybrid vehicles, emergency power backup, industrial power smoothing, and wearable electronics [4-6]. However, the major limitation that still restricts large-scale adoption is their comparatively low energy density. While supercapacitors can release energy very rapidly, their total stored energy remains lower than that of lithium-ion batteries. Therefore, improving the energy density of supercapacitors has become one of the most active directions in modern energy-storage research [7], and progress strongly depends on the development of

---

Received 1 December 2025; revised 17 December 2025; accepted 5 January 2026.

(https:doi.org/……)

advanced electrode materials capable of combining high capacitance, fast electrochemical kinetics, and long-term stability [8].

Among the many electrode materials investigated, spinel metal oxides with the general formula AB_2O_4 have received significant attention in recent years [9]. Numerous studies have highlighted the outstanding electrochemical behavior of spinel oxides such as $NiCo_2O_4$, Co_3O_4, $MnCo_2O_4$, $ZnMn_2O_4$, and Fe_3O_4 for high-performance supercapacitors [4,10-13]. These materials possess a three-dimensional face-centered cubic oxygen framework, where metal cations occupy both tetrahedral (A-site) and octahedral (B-site) crystal positions. This arrangement creates a robust and stable lattice capable of tolerating repeated ion insertion and extraction during cycling without structural collapse. Another major advantage of spinel oxides is the presence of multivalent metal ions, such as Ni^{2+}/Ni^{3+}, Co^{2+}/Co^{3+}, $Mn^{2+}/Mn^{3+}/Mn^{4+}$, and Fe^{2+}/Fe^{3+}, which provide multiple reversible redox pathways that contribute to strong pseudocapacitance and higher charge-storage capability than purely double-layer carbons. Recent works between 2024 and 2025 have demonstrated that nanostructured spinel electrodes can achieve very high capacitance values-often exceeding 1500 $F.g^{-1}$-when engineered into nanosheets, hollow spheres, and hierarchical porous structures, owing to improved electronic conductivity and accessible redox sites [11-14]. Spinel ferrites, including $NiFe_2O_4$ and $CoFe_2O_4$, have also shown excellent cycling stability, particularly when combined with conductive matrices such as graphene, carbon nanotubes, MXenes, and conductive polymers, which enhance electron transport and mitigate mechanical degradation during long-term cycling [10-12].

The goal of this review is to provide a clear, accessible, and well-organized discussion of recent progress in spinel-based materials for supercapacitors, written in a simplified and human-friendly style without losing scientific depth. The review first explains the structural characteristics and chemical diversity of spinel oxides that make them suitable for pseudocapacitive charge storage, followed by a detailed overview of the major spinel families, including cobalt-based, nickel-based, manganese-based, ferrite, zinc-based, and multicomponent systems, discussing their advantages, limitations, and performance trends. Various synthesis methods-such as hydrothermal synthesis, co-precipitation, solvothermal methods, electrospinning, microwave processing, spray pyrolysis, and template-assisted routes-are outlined, since they strongly influence the morphology, conductivity, and surface area of the resulting electrode materials [1]. The review also summarizes recent electrochemical performance achievements, analyzing key parameters such as specific capacitance, rate capability, ion diffusion, charge-transfer resistance, coulombic efficiency, and long-term durability. Mechanistic aspects, including redox processes, ion-transport pathways, electron conduction, and structural stability, are also discussed to provide a deep understanding of how spinel oxides function during repeated charge-discharge cycles. Finally, key challenges facing spinel-based materials-such as limited intrinsic conductivity, structural degradation at high current density, and difficulties in large-scale production-are addressed, and future research directions are proposed, including doping strategies, defect engineering, hybrid composites, multimetal substitution, and the development of flexible and solid-state supercapacitor devices. Through this comprehensive overview, the review aims to support both new researchers entering the field and experienced scientists working toward the rational design of next-generation spinel-based electrodes for high-performance energy-storage systems.

2. Background on Spinel Structure

Spinel is a versatile class of crystalline materials with the general formula AB_2O_4 (Fig.1), characterized by a well-defined three-dimensional cubic close-packed oxygen lattice that provides a stable and flexible framework for incorporating a wide range of metal cations, making it an important structural platform for electrochemical applications such as supercapacitors. In the typical spinel configuration, A-site cations occupy one-eighth of the available tetrahedral interstices, while B-site cations fill half of the octahedral interstices, though the exact cation distribution can vary depending on the electronic structure, ionic radii, electronegativity, and formation environment of the constituent metals [15]. Spinels are traditionally classified into three main types-normal spinels, inverse spinels, and mixed (partially inverse) spinels-according to the cation arrangement across tetrahedral and octahedral lattice sites; for example, in normal spinels such as $ZnAl_2O_4$, divalent A-site cations reside in tetrahedral positions and trivalent B-site cations in octahedral ones, whereas in inverse spinels like Fe_3O_4, half of the trivalent cations move to tetrahedral sites while the divalent and remaining trivalent ions share the octahedral sites [16]. This unique distribution results in rich defect chemistry and high variability in electronic properties, allowing spinels to exhibit metallic, semiconducting, or insulating behavior depending on the degree of cation ordering, electron hopping pathways, and charge compensation mechanisms. The presence of multivalent transition metals such as Mn, Co, Ni, and Fe further enhances redox activity, creating abundant energy storage sites that make spinel-based oxides particularly attractive for faradaic charge storage in supercapacitor electrodes, where reversible ion-electron transfer occurs during cycling [17]. Additionally, the robust cubic structure imparts high mechanical stability, thermal resistance, and tolerance to volume changes, allowing the materials to withstand repetitive redox cycling without structural degradation. Spinels also offer a large surface area when engineered into nanoscale morphologies, providing short ion diffusion distances and optimized electrolyte contact. Therefore, the spinel structure effectively combines structural integrity, chemical versatility, electronic tunability, and electrochemical responsiveness, explaining why AB_2O_4 oxides such as $MnCo_2O_4$, $NiCo_2O_4$, $CuCo_2O_4$, and $MnFe_2O_4$ have emerged as leading electrode materials in next-generation high-performance pseudocapacitors [18,19].

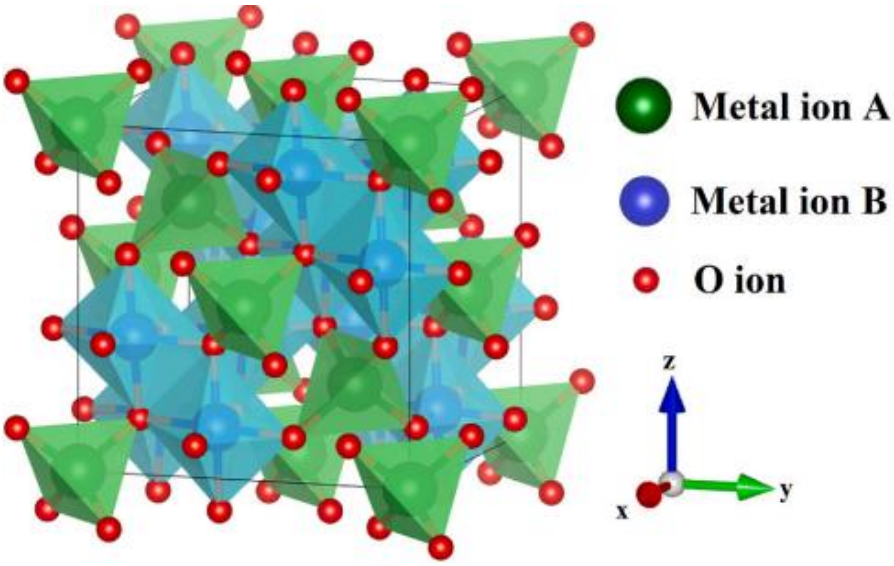

Fig. 1. AB_2O_4 spinel oxide structure [20].

3. Why Spinels Are Attractive for Supercapacitors

Spinel metal oxides (AB_2O_4) have become some of the most promising and widely studied electrode materials for supercapacitors because they combine several key characteristics that directly enhance charge storage performance and long-term stability [7]. One of the most important reasons for their strong performance is their rich redox activity. Unlike pure carbon materials, which store energy mainly through electrostatic ion adsorption, spinels contain transition metals such as Ni, Co, Mn, and Fe that can exist in multiple oxidation states [21], allowing them to participate in fast and reversible faradaic reactions. These redox processes significantly increase the amount of charge stored per unit mass, giving spinel-based electrodes much higher specific capacitance than traditional EDLC systems [22]. For example, materials like $NiCo_2O_4$ can undergo Ni^{2+}/Ni^{3+} and Co^{2+}/Co^{3+} transitions during cycling, which adds multiple electron-transfer pathways to boost pseudocapacitive behavior. Another important advantage is their higher electrical conductivity compared to many simple oxides. Binary oxides like Co_3O_4, NiO, or MnO_2 often suffer from limited conductivity, which restricts electron transport and reduces rate performance. In contrast, bimetallic spinels, particularly $NiCo_2O_4$, are known for their enhanced conductivity due to synergistic interactions between the two metal ions, which create additional charge carriers and facilitate faster electron movement within the lattice. This lower internal resistance helps the electrode deliver high power density and maintain stable operation even at high current loads. In addition to their electrochemical benefits, spinels also demonstrate excellent structural stability, which is essential for devices expected to withstand tens of thousands of charge-discharge cycles. The spinel structure has a robust three-dimensional framework where oxygen anions form a tightly packed cubic lattice, and metal cations occupy tetrahedral (A) and octahedral (B) sites. This well-organized arrangement can accommodate repeated ion insertion and extraction without severe distortion or collapse, making spinel materials much more resistant to mechanical and chemical degradation than many layered or amorphous oxides. Another appealing feature of spinels is their low cost and natural abundance, which is critical for the practical deployment of energy storage technologies. Elements like manganese, iron, cobalt, zinc, and nickel are relatively inexpensive and readily available, allowing the fabrication of low-cost electrode materials compared to noble-metal-based systems. Furthermore, spinels are highly tunable materials, which means their properties can be easily engineered for improved performance. They can be doped with other metal ions to modify electronic structure, substituted at the A or B sites to enhance conductivity or redox activity, and combined with conductive additives such as graphene, reduced graphene oxide, carbon nanotubes, or MXenes to overcome limitations in electron transport. This chemical flexibility allows researchers to design composite or hybrid materials with synergistic effects, resulting in improved mechanical strength, higher surface area, and more accessible active sites. Beyond chemical tuning, spinels can be synthesized into a wide range of nanostructures, including nanosheets, nanowires, nanoneedles, hollow spheres, nanocubes, core–shell structures, and hierarchical porous networks. These engineered shapes not only increase the surface area available for redox reactions but also shorten ion diffusion paths, enhance electrolyte penetration, and improve contact between the active material and the current collector [17]. This combination of intrinsic redox chemistry, good conductivity, structural robustness, low cost, compositional tunability, and versatility in morphology makes spinel oxides exceptionally well-suited for high-performance supercapacitors. As a result, they have become one of the leading classes of pseudocapacitive materials in recent research and continue to attract growing attention for both academic study and real-world energy storage applications.

3.1. Types of Spinels Used in Supercapacitors

Spinel oxides used in supercapacitors cover a wide family of materials (Fig. 2), and each type brings unique electrochemical advantages because of its cation configuration, redox activity, and conductivity. Among them, cobalt-based spinels [23] such as Co_3O_4 and $NiCo_2O_4$ are the most widely studied due to their high electrical conductivity and rich redox chemistry [24]. Co_3O_4 itself has good pseudocapacitance but suffers from moderate conductivity; however, when cobalt is combined with nickel to form $NiCo_2O_4$, the resulting bimetallic spinel exhibits superior performance because Ni^{2+}/Ni^{3+} and Co^{2+}/Co^{3+} pairs offer multiple electron-transfer pathways. This synergy also improves conductivity significantly, making $NiCo_2O_4$ one of the highest-performing spinel materials for supercapacitor electrodes. Another important family is manganese-based spinels [25], including $MnCo_2O_4$, $ZnMn_2O_4$, $NiMn_2O_4$, and $MnFe_2O_4$. Manganese has multiple oxidation states ($Mn^{2+}/Mn^{3+}/Mn^{4+}$), which provide abundant active sites for faradaic reactions. Manganese spinels are also attractive because manganese is low-cost, environmentally friendly, and available in large quantities. For example, $MnCo_2O_4$ often displays excellent cycling life due to manganese's structural stability, and $ZnMn_2O_4$ can offer high specific capacitance thanks to its mixed cation distribution, which improves electron hopping and ion diffusion. Nickel-based spinels [26], such as $NiFe_2O_4$ and $NiMn_2O_4$, are also promising. Nickel ferrite ($NiFe_2O_4$), for instance, has shown strong pseudocapacitive behavior due to the Fe^{2+}/Fe^{3+} redox pair and the Ni^{2+}/Ni^{3+} couple. Although ferrites generally have lower conductivity than cobaltites, this limitation can be overcome through compositing with conductive materials such as graphene or carbon nanotubes, leading to impressive energy density in hybrid supercapacitors [27]. Iron-based spinels [28], especially Fe_3O_4 and $CoFe_2O_4$, offer good electrochemical activity combined with very low cost and environmental safety. Fe_3O_4 is magnetic and provides a high theoretical capacitance, but it can suffer from cycling instability unless combined with carbon or engineered into stable nanostructures. $CoFe_2O_4$ has better conductivity and mechanical strength, making it more suitable for long-term cycling applications. Another useful group includes zinc-based spinels [29] like $ZnCo_2O_4$ and $ZnMn_2O_4$, which are known for their high porosity, abundant oxygen vacancies, and relatively low cost. Zinc also helps stabilize the spinel framework, reducing degradation during repeated charge–discharge cycles. $ZnCo_2O_4$ in particular has shown excellent rate performance in many studies because cobalt enhances the overall conductivity while zinc improves structural stability. Beyond these traditional systems, multicomponent spinels [31] containing three or more metal ions-such as $NiCuCo_2O_4$, $MnCoFe_2O_4$, or $ZnNiCo_2O_4$-are attracting growing attention. These materials combine the advantages of multiple metal ions, creating richer redox chemistry and improved conductivity through synergistic effects. For example, Ni-Cu-Co spinels often show better electron transport and superior capacitance compared to their binary counterparts. Researchers are also developing doped spinels [30] where small amounts of metal ions like Al^{3+}, Cr^{3+}, Mg^{2+}, or rare-earth elements are introduced into the lattice to tune conductivity, surface activity, and defect concentration. Doping can increase oxygen vacancies, enhance electron hopping, or strengthen structural stability, leading to improved long-term cycling performance. Overall, the wide variety of spinel oxides-including cobaltites, manganese-based spinels, ferrites, nickel-based spinels, zinc-containing systems, and multimetal/doped spinels-provides a rich library of materials for designing high-performance supercapacitors. Their tunable composition allows researchers to precisely adjust redox activity, conductivity, and morphology, making spinels one of the most flexible and powerful material families in the field of energy storage.

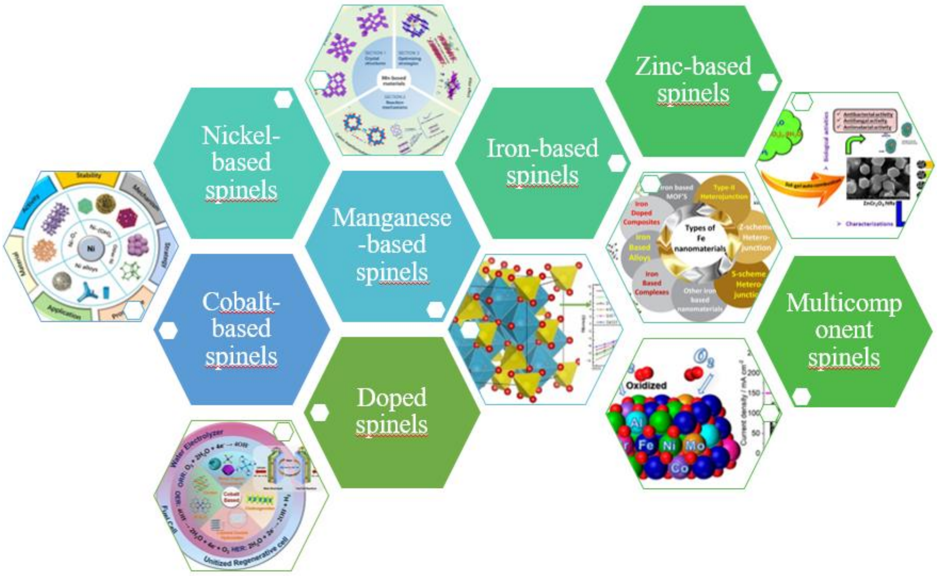

Fig. 2. Overview of different types of spinel materials used in supercapacitors, including cobalt-based, nickel-based, manganese-based, iron-based, zinc-based, doped, and multicomponent spinels, highlighting their structural diversity and potential applications.

3.2. Synthesis Methods

The choice of synthesis method directly governs the morphology, crystallinity, specific surface area, and electrochemical performance of spinel oxides, which is why a wide range of well-established techniques are currently used for (Fig. 3) supercapacitor electrodes: the most popular are hydrothermal and solvothermal routes, which provide precise control over particle size and shape under relatively mild conditions, enabling the fabrication of nanowires, nanosheets, hollow spheres, and hierarchical architectures with high accessible surface area [32,33]; a simple and easily scalable approach remains co-precipitation, in which a mixed hydroxide precursor is precipitated from metal salt solutions and then calcined; excellent compositional homogeneity is achieved via the sol-gel method; one-dimensional fibers are conveniently produced by electrospinning; spherical and hollow particles are obtained through spray pyrolysis; complex porous and core-shell structures are realized using soft or hard template-assisted methods; and when ultra-fast synthesis is required, microwave-assisted routes yield highly crystalline nanoparticles in minutes [34], while combustion synthesis and thermal decomposition can produce fine powders in seconds, albeit with less morphology control [35]. Ultimately, each method offers its own trade-off between structural control, cost, and scalability, and the choice depends on the target shape, conductivity, and electrochemical activity required from the final electrode.

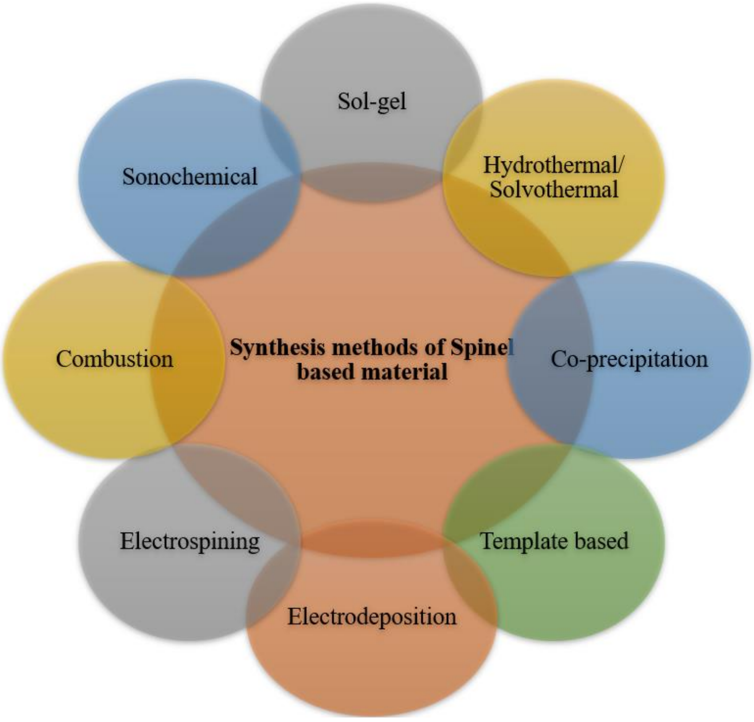

Fig. 3. Techniques involved in the synthesis of spinel-based material.

3.3. Morphologies and nanostructures

The way a spinel material looks at the nanoscale (Fig. 4) (wires, sheets, hollow balls, etc.) basically decides how well it will work in a supercapacitor: the more open the structure, the easier electrolyte to get inside, the shorter the paths for ions, and the faster electrons fly, all while the electrode doesn't fall apart after thousands of cycles. That's why everyone is trying to move away from simple bulky particles and make fancy nano-shapes: 1D nanowires and nanofibers give a highway for electrons straight along their length, 2D nanosheets and flakes expose tons of active surface and cut ion diffusion distance to almost nothing (especially when they're grown directly on nickel foam or carbon cloth so you don't need any binder), and 3D hierarchical stuff (flowers, urchins, nanosheets on wires) combines huge surface area with big open pores so the electrolyte soaks everything instantly, delivering sky-high capacitance even at crazy charging speeds [36,37]. Hollow spheres, core-shell, yolk-shell, and other porous designs take it further: they buffer mechanical stress during cycling and let the electrolyte attack the material from inside as well as outside. Simple nanoparticles and cubes are still around because they pack nicely, but they usually lag behind the more open architectures in rate performance. Bottom line: smart nanostructuring is the fastest and most reliable way to squeeze way more energy, power, and lifetime out of spinel electrodes compared to plain bulk powders.

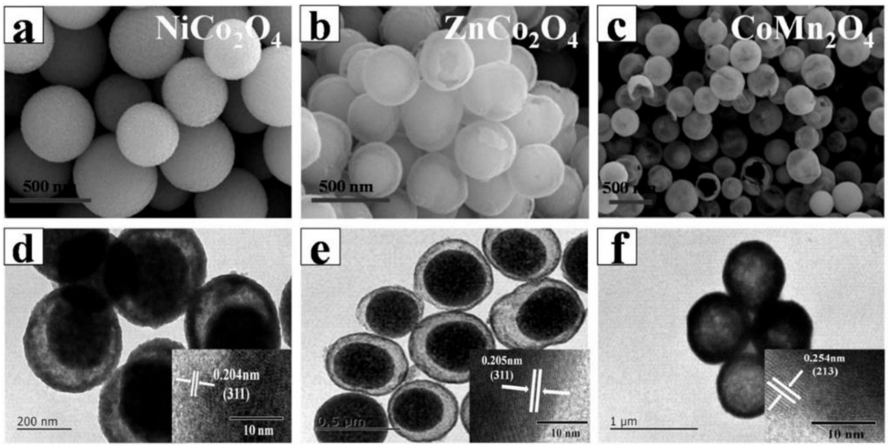

Fig. 4. SEM, TEM, and HRTEM of hollow $NiCo_2O_4$ (a, d), $ZnCo_2O_4$ (b, e), and $CoMn_2O_4$ (c, f) spheres [38,39].

3.4. Electrochemical Performance

Spinel electrodes rock in supercapacitors because they deliver real faradaic punch without sacrificing too much speed or lifetime: you typically see quasi-rectangular CV curves with fat redox peaks, specific capacitance from 800 up to 2000+ F g^{-1} at low currents, and after 5000-10000 cycles they still keep 85-95% of that capacity thanks to their tough 3D lattice that doesn't crumble when the material keeps expanding and shrinking. Charge-discharge curves are nicely sloped (classic pseudocapacitor style), rate capability stays strong even at 20-30 A g^{-1} if the nanostructure is open and conductive (especially with $NiCo_2O_4$ and $MnCo_2O_4$), and EIS shows tiny charge-transfer resistance plus almost vertical lines in the low-frequency zone, meaning ions and electrons fly fast. Put them into real asymmetric or hybrid devices, and you easily hit 40-60 Wh kg^{-1} energy density while still having power like a carbon supercapacitor [40]. Sure, some spinels are still a bit sluggish in pure form and can lose inner surface if the particles are too thick, but that's why everyone now mixes them with graphene, CNTs, or polymers, and the numbers just keep getting better.

3.5. Mechanisms of Charge Storage

The charge storage mechanisms in spinel-based supercapacitors are fundamentally governed by pseudocapacitive Faradaic reactions involving reversible electron transfer between transition-metal ions with multiple oxidation states, allowing significantly higher capacitance than purely electrostatic electric double-layer capacitors (EDLCs). The general spinel structure AB_2O_4 contains A-site cations in tetrahedral positions and B-site cations in octahedral positions, and both can host transition metals such as Ni, Co, Mn, Fe, Cu, and Zn [41], each capable of switching between oxidation states like Ni^{2+}/Ni^{3+}, Co^{2+}/Co^{3+}, Mn^{3+}/Mn^{4+}, or Fe^{2+}/Fe^{3+} during charge–discharge cycling, meaning multiple electrons per formula unit can participate in energy storage. Because of this rich redox chemistry, spinels rely mainly on surface and near-surface pseudocapacitive mechanisms (Fig. 5) where ions from the electrolyte, typically OH^- in alkaline solutions, rapidly adsorb and react at active metal sites according to reactions such as $NiCo_2O_4 + OH^- \rightleftharpoons NiOOH + CoOOH + e^-$, and the reversibility of these reactions ensures high coulombic efficiency and long cycle life. In addition to surface reactions, some spinel materials also support intercalation-based storage, where small ions like H^+, OH^-, or Na^+ insert into the crystal lattice without collapsing the 3D framework. This is possible because the spinel structure is mechanically stable and has spacious ion diffusion channels, allowing ion insertion and extraction with minimal strain, which enables higher energy density resembling battery-type electrodes while retaining fast kinetics suitable for supercapacitors. Electronic conductivity is another factor that enhances charge storage, because the mixed valence states of transition metals in spinels allow electron hopping between neighboring metal ions, making materials such as $NiCo_2O_4$ far more conductive than single-metal oxides like NiO or Co_3O_4. This conductivity ensures faster charge transfer and lower internal resistance, which translates into higher power density. Furthermore, the efficiency of the charge storage mechanism strongly depends on morphology and particle size [40]; nanosheets, nanowires, hollow structures, and porous frameworks greatly increase accessible surface area, reduce diffusion length for ions, expose more active metal sites, and make Faradaic reactions more rapid and complete. Tailoring the composition of spinels also enhances the mechanisms: doping with elements such as Cu, Fe, V, or Cr modifies the electronic structure, increases the number of redox centers, and lowers charge-transfer resistance, while combining spinels with conductive networks like graphene, carbon nanotubes, MXenes, or conductive polymers allows electrons to move quickly throughout the electrode and prevents particle aggregation. These hybrid configurations create multiple interconnected pathways for ion and electron transport, enabling higher specific capacitance, better rate capability, and improved cycling stability [8]. Ultimately, the charge storage behavior of spinel-based electrodes is the result of a synergistic combination of mixed-valence redox activity, fast ion diffusion channels, high electrical conductivity, and structural robustness. And by optimizing crystal chemistry, morphology, and composite design, researchers can tune spinels to balance high energy density, power density, and durability in next-generation supercapacitors.

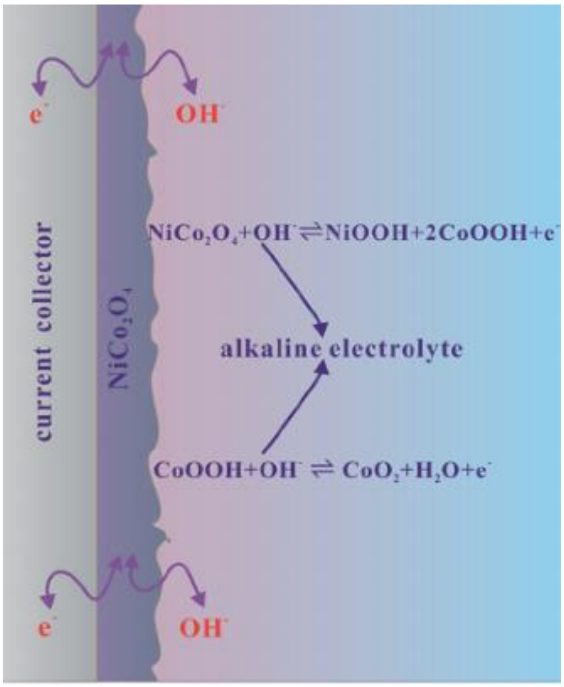

Fig. 5. A schematic of the charge storage mechanism of $NiCo_2O_4$ [40].

3.6. Composite and Hybrid Spinel Materials

Pure spinels are cool on paper with all their redox tricks, but in real life, they often choke on slow conductivity, particles stick together, and the structure slowly crumbles after a few thousand cycles-so the fix everyone uses now is to team them up with something that conducts like crazy and keeps everything in place. Throw graphene, CNTs, MXene, or carbon nanofibers in the mix, and you instantly get a super-highway for electrons, way less resistance, and the spinel nanoparticles stay nicely separated, so every redox site actually works. Add conducting polymers like PANI or PPy, and you get flexible electrodes that bend without breaking, plus extra pseudocapacitance on top. People also love making spinel-on-spinel combos ($NiCo_2O_4$ with $MnCo_2O_4$, $ZnCo_2O_4$ with Fe_3O_4, etc.) because each brings its own strength to the party-one gives huge capacity, the other keeps the juice flowing fast. All these hybrids are built as hollow balls, core shells, cages, or mesoporous jungles, so ions barely have to travel, and mechanical stress gets soaked up instead of cracking the material. The result? Capacitance jumps, rate capability stays solid even at brutal currents, and cycling life easily crosses 10-20k cycles without sweating. Bottom line: pure spinels are yesterday; today's winners are smart composites that take the redox power of spinels and turbo-charge it with conductive scaffolding for real-world, high-energy, high-power, long-life supercaps.

3.7. Device Configurations and Practical Supercapacitors

In practical applications, the performance of spinel-based materials depends not only on their intrinsic electrochemical properties but also on how they are integrated into real device configurations, which include electrode assembly, current collectors, separators, electrolytes, and packaging. Supercapacitors using spinel electrodes are commonly constructed in three main configurations: three-electrode systems, used primarily in laboratory testing to accurately evaluate electrode behavior; two-electrode coin or Swagelok-type cells, which more closely represent real device performance; and full packaged devices such as pouch cells, cylindrical cells, and flexible or wearable architectures designed for consumer electronics and portable energy storage. In laboratory research, the three-electrode setup-consisting of a working electrode coated with the spinel material, a reference electrode such as Ag/AgCl or Hg/HgO, and a counter electrode like platinum wire-allows precise measurement of redox behavior, specific capacitance, and kinetics without interference from other cell components [44]. However, real-world performance is better reflected in two-electrode systems where both positive and negative electrodes operate simultaneously, and losses related to internal resistance, electrode balancing, and charge-transfer efficiency are more accurately captured. For asymmetric supercapacitors, spinels are often employed as positive electrodes due to their pseudocapacitive behavior and high theoretical capacitance, paired with carbon-based negative electrodes providing fast EDLC-type charge storage, resulting in devices that achieve higher operating voltage and improved energy density compared to symmetric configurations. The choice of electrolyte also significantly influences device performance, with aqueous electrolytes (KOH, Na_2SO_4, Li_2SO_4) offering high ionic conductivity and low cost but limited voltage window (typically <1.8 V), while organic or ionic liquid electrolytes allow broader operating voltages of 2.5-3.5 V and greater overall energy density, though at higher cost and increased safety considerations. The interface between the spinel electrode and current collector (often stainless steel, nickel foam, titanium foil, or conductive carbon cloth) must ensure strong adhesion and minimal contact resistance; using 3D conductive scaffolds like nickel foam or carbon cloth provides mechanical support and fast electron transport, improving rate capability. For flexible and wearable energy-storage systems, spinels are increasingly deposited onto polymer substrates, textiles, carbon fibers, or hydrogels to create bendable, stretchable, and lightweight devices suitable for sensors, smart textiles, and portable electronics. Inkjet printing, spray coating, electrophoretic deposition, and roll-to-roll processing are emerging as scalable fabrication methods that support industrial production. Moreover, device-level packaging must ensure stability against electrolyte leakage, corrosion, and mechanical stress, especially for long-term cycling. In performance terms, practical cells using spinel-based electrodes can achieve specific capacitances exceeding 100-200 F g^{-1} in a two-electrode configuration, with areal and volumetric capacitances optimized for space-limited applications. Many systems also demonstrate long life spans, retaining more than 80-95% of initial capacitance after thousands of cycles [1]. As spinel synthesis, electrode design, and device engineering continue to improve, these materials are moving closer to commercial viability, offering high-power, fast-charging, and environmentally friendly energy-storage solutions for transportation systems, consumer electronics, renewable energy buffering, and next-generation wearable technologies [45].

3.8. Challenges and Limitations

Despite their rapidly growing popularity and promising electrochemical properties, spinel-based materials for supercapacitors still face several challenges and limitations that hinder their large-scale commercialization and real-world deployment, many of which arise from the inherent characteristics of transition-metal oxides and the complexities of device engineering. One of the primary challenges is the moderate intrinsic electronic conductivity of many spinels, which, although superior to single-metal oxides, remains lower than desired for high-power applications, especially when the material is used in thick electrode layers where electron pathways become longer and internal resistance increases, resulting in voltage drop, heat generation, and reduced rate capability. Another major limitation is ion transport within the electrode; while nanoscale spinels offer short diffusion distances, large or agglomerated particles can trap active sites within the crystal bulk, making them difficult for electrolyte ions to reach, thereby reducing capacity utilization. The electrochemical reactions in spinels also involve structural changes associated with ion insertion/extraction and redox transitions, and although the 3D spinel framework is generally robust, repeated volume fluctuation can cause microcracks, mechanical degradation, and loss of electrical contact over long-term cycling, particularly in high-capacity systems where multiple oxidation states are accessed. Additionally, achieving controlled morphology, particle size distribution, and defect concentration during synthesis can be challenging, and small variations in hydrothermal conditions, calcination temperature, or precursor composition can lead to major differences in performance, making reproducibility a limiting factor for industrial manufacturing. The cost and environmental impact of some spinel compositions also raise concerns; elements such as cobalt are relatively expensive and associated with supply-chain and sustainability issues, while complex multistep syntheses require energy and chemical use that can increase environmental burden. From a practical device perspective, many laboratory tests rely on three-electrode configurations that may overestimate performance compared to real two-electrode systems, leading to gaps between academic reporting and commercial reality. Scaling up electrode coatings for large-area production introduces additional limitations, such as maintaining strong adhesion between active material and current collector, ensuring uniform thickness, and preventing cracking or delamination during drying or cycling. Electrolyte compatibility is also critical, as aqueous systems are safe and conductive but limited in voltage window, while organic or ionic liquid electrolytes offer higher energy density but bring increased cost, stricter sealing requirements, and potential flammability. Another significant limitation is the difficulty in balancing energy and power performance within a single material; spinels can provide high power density due to fast redox reactions, but their energy density still lags behind some battery materials, meaning hybrid cell designs are often required to achieve competitive performance. Finally, the long-term reliability and thermal stability of spinel-based devices under real operating conditions-such as temperature swings, continuous charge/discharge use, or prolonged high-voltage operation-remain insufficiently tested, and further studies are needed to fully understand degradation mechanisms and improve lifetime. Addressing these challenges will require advances in synthesis control, nanostructure engineering, cost reduction, scalable processing, and realistic device testing to unlock the full commercial potential of spinel-based supercapacitors [39,40].

3.9. Future Outlook and Perspectives

Looking ahead, the future of spinel-based supercapacitors is extremely promising, with research trends increasingly focused on designing materials and devices that bridge the gap between high-power supercapacitors and high-energy batteries [40], aiming to meet the growing demands of electric vehicles, grid-level renewable energy storage, Internet-of-Things systems, and next-generation portable electronics. Continued advances in material engineering are expected to center on improving conductivity, increasing ion-accessible surface area, and enhancing long-term structural stability, with strategies such as controlled defect introduction, surface functionalization, multi-ion doping, and crystal facet engineering poised to significantly improve redox kinetics and electron transport. Hybridization and compositing will remain crucial, especially as researchers combine spinels with carbon nanomaterials, MXenes, conductive polymers, or other metal oxides to create synergistic charge-storage mechanisms that simultaneously enhance energy density and power delivery while suppressing structural degradation during thousands of cycles. At the same time, progress in understanding charge-storage mechanisms through operando characterization methods such as in situ XRD, XPS, Raman spectroscopy, TEM analysis, and electrochemical impedance tracking will offer valuable insight into ion migration pathways, lattice evolution, and charge-transfer dynamics, enabling predictive modeling and rational material design rather than trial-and-error development. Machine learning and computational simulation are expected to play a larger role as well [27], accelerating the discovery of novel spinel compositions with optimized electronic structures, reduced activation energies, and higher redox-site density, potentially unlocking new families of high-performance materials beyond the commonly studied $NiCo_2O_4$, $MnCo_2O_4$, and $ZnCo_2O_4$ systems. From a device engineering standpoint, future research will focus on scalable processing methods such as spray deposition, roll-to-roll coating, 3D printing, electrodeposition, and ink formulation that can translate laboratory electrodes into industrial manufacturing while maintaining uniformity, mechanical robustness, and electrochemical efficiency. Flexible and wearable supercapacitors represent another major direction, where ultrathin spinel films, textile-supported electrodes, stretchable polymer electrolytes, and integrated smart sensors may enable high-performance power sources for health monitoring, soft robotics, and smart clothing. Environmentally friendly systems will also gain importance, with efforts aimed at reducing the use of expensive or supply-critical metals like cobalt, developing aqueous or gel-based electrolytes with larger safe voltage windows, and improving recycling and green synthesis routes to reduce the environmental footprint. In real-world applications, improving volumetric energy density and safety will be key to making spinel-based devices competitive with Li-ion batteries, and asymmetric or hybrid capacitor configurations will likely dominate because they allow higher operating voltages and balanced performance. Finally, long-term reliability studies under realistic conditions-high temperature, mechanical stress, continuous cycling, and large current loads-will be necessary to guarantee that spinel-based devices can operate reliably in commercial systems such as electric buses, regenerative braking, solar-grid buffering, emergency backup systems, and compact consumer electronics. By combining innovation in chemistry, nanostructure design, advanced characterization, scalable manufacturing, and realistic device integration, spinel-based supercapacitors are expected to evolve into mature, commercial energy-storage solutions that offer fast charging, high power, long life, environmental sustainability, and cost-effective performance for the next generation of global energy applications.

4. Conclusion

In conclusion, spinel-based materials have rapidly emerged as one of the most promising classes of electrode materials for next-generation supercapacitors [35], offering a unique combination of high theoretical capacitance, structural robustness, rich redox chemistry, and broad compositional tunability that allows researchers to optimize performance for diverse energy-storage applications. Their AB_2O_4 crystal structure provides multiple redox-active transition-metal sites, fast electron transport via mixed-valence conduction, and sufficient structural tolerance to withstand repeated ion insertion/extraction without catastrophic lattice collapse, enabling high cycling stability that is critical for long-term operation. However, achieving high practical performance depends heavily on controlling nanoscale morphology, composition, and interface characteristics, as these directly influence ion diffusion paths, electron mobility, and the degree to which active sites participate in charge storage. Significant progress has been made in engineering spinels into hollow structures, nanosheets, nanowires, hierarchical porous frameworks, and other architectures that maximize accessible surface area and accelerate reaction kinetics, while doping and multi-metal substitution have proven effective in enhancing conductivity, increasing redox-site density, and stabilizing reaction intermediates during cycling. The development of composite and hybrid systems-including combinations with carbon nanotubes, graphene, MXenes, conducting polymers, and other metal oxides-has helped overcome limitations such as moderate conductivity and structural stress, producing electrodes that deliver high power density, improved rate capability, and outstanding cycle life [32]. At the device level, spinel electrodes have demonstrated strong operation in both asymmetric and symmetric configurations, with real-world performance continuing to improve as researchers optimize electrode balancing, electrolyte selection, manufacturing methods, and current collector integration. Yet, challenges remain, including scalability of synthesis, environmental and supply-chain concerns for certain metals, performance gaps between laboratory three-electrode testing and real device operation, and the need for improved volumetric energy density to compete with established battery technologies. Future progress will require interdisciplinary advances in material design, operando characterization, theoretical modeling, large-scale fabrication, and device engineering to ensure that laboratory breakthroughs translate into reliable commercial systems. With ongoing innovations in green synthesis, flexible and wearable device integration, solid- and gel-electrolyte systems, and cost-reducing material substitutions, spinel-based supercapacitors are well positioned to play a major role in high-power energy-storage sectors, including electric mobility, renewable energy buffering, industrial power stabilization, next-generation IoT devices, and portable electronics. In summary, while challenges remain, the rapid pace of development, combined with the inherent advantages of spinel chemistry, suggests that these materials are moving steadily from laboratory research toward practical implementation, holding strong potential to contribute meaningfully to cleaner, more efficient, and more sustainable global energy solutions.

Funding

This work does not receive any funding.

Conflict of interest

The authors declare no conflict of interest.

Acknowledgments

The researchers extend their thanks and appreciation for the collaboration and support of the Scientific Research Projects Coordination of the University of Sakarya (2024-25-54-151).

References

1 Jia X., Liu C., Neale Z.G., Yang J., Cao G. (2020) Active Materials for Aqueous Zinc Ion Batteries: Synthesis, Crystal Structure, Morphology, and Electrochemistry. *Chem. Rev.* 120, 7795–7866

2 Li S., Wang Q., Zhao X., Chen J., Zhang J. (2022) Multifunctional metal oxide nanostructures for advanced electrochemical devices. *Mater. Adv.* 3, 610–623

3 He L., Sun P., Hou X., Zhang Y. (2024) Interface-engineered metal oxide architectures for enhanced charge storage. *J. Colloid Interface Sci.* 670, 142–153

4 Li X., Zhang Y., Chen L. (2024) High-performance Co_3O_4@N-doped carbon electrodes for supercapacitors. *J. Alloys Compd.* 945, 177581

5 Kumar A., Singh P., Yadav R. (2025) Enhanced electrochemical performance of $MnCo_2O_4$ nanostructures for hybrid supercapacitors. *J. Alloys Compd*. 1025, 184960

6 Huang Y., Zhao J., Liu B. (2025) Recent advances in transition-metal-oxide-based supercapacitors. *Chin. Phys.* 34 ,100907

7 Ahmed A., Nassar M.Y., Shaker M.R. (2023) Metal oxide–based hybrid electrodes for advanced energy storage devices. *Energy Storage Technol.* 56. 107672

8 Kumar N.S., Rao V.R. (2025) High-entropy metal oxide thin films for next-generation electronic devices. *FlatChem.* 52, 100947

9 Abou-Hamad M.O., Al-Said F. (2025). Sol-gel synthesis and characterization of novel spinel oxide nanostructures *J. Sol-Gel Sci. Technol*

10 Multiple recent studies (2024–2025) report>1500 F g−1 spinel electrodes with optimized nanostructures.

11 Hybrid and composite spinel systems demonstrating improved cycling stability, conductivity, and structural integrity (2024–2025)

12 Ullberg R., Seaton R. (2024).*Advanced Transition-Metal Oxides for Catalytic and Energy Applications,* PhD Dissertation, University of Florida

13 Kumar S., Patel B., Das P. (2025) Structural and electronic behavior of spinel oxide lattices under high pressure. *Physica B.* 707. 417533

14 Vijayaraghavan K. (2023) Advances in Metal Oxides and Their Composites for Emerging Applications. *Elsevier,*

15 Kumar R., Sharma S. (2024) Spinel-structured transition metal oxides for electrochemical energy storage: Fundamentals and recent advances. *Adv. Energy Mater*. 14, 2205671

16 Huang L., Peng X. (2025) Structural diversity and electrochemical behavior of AB$_2$O$_4$ spinels for charge storage applications. *J. Mater. Chem. A.* 13, 1184–1207

17 Li M., Sun Y., Zhang J., Zhao S., Yang T. (2025) Design and fabrication of advanced AB$_2$O$_4$ spinel nanostructures for improved electrochemical energy storage. *Mater. Des.* 245, 114157

18 Michael A., Gupta S. (2020) Recent progress in metal-oxide nanomaterials for energy systems, in: Materials for Sustainable Energy Applications. *Elsevier,* 85–122

19 Kim J., Lee S., Park J. (2023) Energy storage enhancement using hierarchical mixed-metal oxides. *Energies.* 16, 5604

20 Zhong H., Campos-Roldán C.A., Zhao Y., Zhang S., Feng Y., Alonso-Vante N. (2018) Recent Advances of Cobalt-Based Electrocatalysts for Oxygen Electrode Reactions and Hydrogen Evolution Reaction. *Catalysts.* 8 (11), 559

21 Quilez-Bermejo J. (2021) *Electrochemical development of metal oxide nanostructures for hybrid energy devices*, PhD Thesis, University of Alicante

22 Guo Y., Zhang Y., Lu H., Li Z. (2022) Manganese-based materials as cathode for rechargeable aqueous zinc-ion batteries. *Battery Energy.* 1 20210014

23 Smith A., Lee B., Johnson C. (2024). Advanced separation and purification of nanostructured spinel oxides for energy storage, *Sep. Purif. Technol.* 345 130441

24 Hassan M., Rehman S., Nawaz F. (2024) Highly conductive metal oxide nano-architectures for supercapacitors. *Electrochim. Acta.* 492, 145395

25 Arif N., Zafar M.N., Batool M., Humayun M., Iqbal M. A., Younis M., Li L., Li K., Zeng Y.-J. (2024) Recent advances and perspectives on iron-based photocatalysts. *J. Mater. Chem. C.* 12, 12639-12652

26 . Ghotekar S, Pansambal S., Nguyen V.-H., Bangale S., Lin K.-Y. A., Ananda Murthy H. C., Oza R. (2023) Spinel ZnCr$_2$O$_4$ nanorods synthesized by facile sol-gel auto combustion method with biomedical properties. *J. Sol-Gel Sci. Technol.* 105, 176-185

27 Salleh N. F. M., Ismail A. M. (2017) New direct consecutive formation of spinel phase in (Fe, Co, Ni)Al$_2$O$_4$ composites. *Mater. Chem. Phys.* 204, 33-41

28 Zhang Q., Hu Y., Wu H., Zhao X., Wang M., Wang S., Feng R., Chen Q., Song F., Chen M., Liu P. (2023).Entropy-stabilized multicomponent porous spinel nanowires of NiFeXO$_4$ (X = Fe, Ni, Al, Mo, Co, Cr) for efficient and durable electrocatalytic oxygen evolution in alkaline medium, *Nano Research*

29 Tang R., Li W., Wen Y. (2025) Ultrahigh capacitance NiCo$_2$O$_4$ hollow structures for energy storage. *J. Power Sources.* 632, 238436

30 Wang L., Zhang Y., Liu M. (2024) Hierarchical MnCo$_2$O$_4$ nanoflowers synthesized by hydrothermal method for high-performance supercapacitors, Electrochim. *Acta.* 528, 145892

31 Kumar S., Jose R. (2024) Microwave-assisted rapid synthesis of spinel NiCo$_2$O$_4$ nanoparticles with superior electrochemical performance. *J. Alloys Compd.* 989, 172345

32 Chen H., Zhao X. (2025) Solution combustion synthesis of Co$_3$O$_4$/NiCo$_2$O$_4$ nanocomposites as efficient electrode materials for hybrid supercapacitors. *Ceram. Int.* 51, 4123-4135

33 Tang R., Li W., Wen Y. (2025) Ultrahigh capacitance NiCo$_2$O$_4$ hollow structures for energy storage. *J. Power Sources* 632, 238436

34 Wang L., Zhang Y., Liu M. (2024) Hierarchical MnCo$_2$O$_4$ nanoflowers synthesized by hydrothermal method for high-performance supercapacitors. *Electrochim. Acta.* 528, 145892

35 Zhang J., Cai Y., Zhao X., et al. (2021) Flexible mixed metal oxide hollow spheres/RGO hybrid lamellar films for high-performance supercapacitors. *Colloids Surf. A.* 609, 125902

36 Gopi S., Aravind V., Nagarajan R. (2020) Facile synthesis of spinel metal oxide nanostructures with enhanced surface activity for electrochemical applications, *Colloids Surf. A.* 6021,25902

37 Tang R., Li W., Wen Y. (2025) Ultrahigh capacitance NiCo$_2$O$_4$ hollow structures for energy storage. *J. Power Sources.* 632, 238436

38 Gondal M. A., Dastageer A., Khan M. A. (2020) Structural and electronic tuning of spinel ferrites for improved charge-storage behavior. *J. Solid State Chem.* 290, 121510

39 Zhang Z., Liu Q., Zeng H. (2021) High-performance hybrid electrodes based on transition-metal spinel oxides for next-generation supercapacitors. *J. Power Sources* 506, 230744

40 Lee J.-J., Lee K.-H., Yu S.-H., et al. (2014)$NiCo_2O_4$-based materials for electrochemical supercapacitors. *RSC Adv*. 4, 37517-37527

41 Salunkhe R. R., Tang J., Kamachi Y., Nakato T., Kim J. H., Yamauchi Y. (2013) Controlled synthesis of hierarchical porous spinel $ZnCo_2O_4$ structures for high-performance supercapacitors. *Nanoscale.* 5, 333–337

42 Singh S. K., Kumar R., Gupta A., et al. (2024) Rational Design of Asymmetric Spinel/Defect Spinel ($ZnMn_2O_4/Cu_{1.5}Mn_{1.5}O_4$) Nanocomposite-Based Supercapacitor Devices for Efficient Energy Storage with Improved Cycle Stability. *ACS Appl. Energy Mater*. 7, 7205–7219

AUTHORS' INFORMATION

Zhangabay Turar - MSc student, Department of Physics, Sakarya University; Researcher, PlasmaScience LLP, Ust-Kamenogorsk, Kazakhstan; ORCID iD: https://orcid.org/0009-0004-6202-112X (e-mail: zhangabay.turar@ogr.sakarya.edu.tr Phone: +905376890526)

Ali Coruh – Prof.Dr, Department of Physics, Sakarya University, Sakarya, Turkey; SCOPUS Author ID: 24460990900 ORCID iD: https://orcid.org/0000-0002-7362-6173 (e-mail: coruh@sakarya.edu.tr Phone: +905355594339)

Arystanbek Kussainov - Doctoral student D. Serikbayev East Kazakhstan Technical University; Institute of Composite Materials LLP, Ust-Kamenogorsk, Kazakhstan; SCOPUS Author ID: 59515031200. (e-mail: arys20055@gmail.com)

Rakhmetova Mairagul - Dr. Department of Plasma Physics and Computer Physics, Al-Farabi Kazakh National University, Almaty, Kazakhstan/ Department of Physics and Technical disciplines, Kh. Dosmukhamedov Atyrau University, Atyrau, Kazakhstan; ORCID iD: https://orcid.org/0000-0003-4529-0999 (e-mail: maira_12_05@mail.ru)

ORIGINAL STUDY

THERMODYNAMICS AND ELASTIC PROPERTIES OF TERNARY ALLOYS OF PD, PT, AND RH METALS: A MOLECULAR DYNAMICS SIMULATION STUDY

Yeshim Sarıbek[1], Zhangabay Turar[1], Arystanbek Kussainov[2], Rakhmetova Mairagul[3], Ali Coruh[1]

[1]Department of Physics, Sakarya University, Sakarya, Turkey
[2]Protectivie and Functional Coatings Scientific Center, Daulet Serikbayev East Kazakhstan Technical University Ust-Kamenogorsk 070010, Kazakhstan
[3]Department of Plasma Physics and Computer Physics, Al-Farabi Kazakh National University, Almaty, Kazakhstan/ Department of Physics and Technical disciplines, Kh. Dosmukhamedov Atyrau University, Atyrau, Kazakhstan;
*Corresponding author: coruh@sakarya.edu.tr

Abstract. *Thermodynamic and mechanical properties of multicomponent noble-metal alloys determine their performance in catalytic systems, energy-storage devices, and high-temperature structural materials. In the present work, temperature-dependent properties of four face-centered cubic ternary alloys of the Pd-Pt-Rh system with compositions* $Pd_{15}Pt_{10}Rh_{75}$, $Pd_{5}Pt_{25}Rh_{70}$, $Pd_{5}Pt_{70}Rh_{25}$, *and* $Pd_{75}Pt_{15}Rh_{10}$ *have been investigated by large-scale molecular dynamics simulations using the quantum Sutton-Chen potential. Calculations were performed for a supercell containing 1372 atoms in constant-enthalpy-constant-pressure, isothermal-isobaric, and microcanonical ensembles over a wide temperature range. It was found that the* $Pd_{5}Pt_{70}Rh_{25}$ *alloy exhibits the highest density, cohesive energy, and bulk modulus due to its high platinum content, which provides the strongest interatomic bonding. All studied compositions show negative enthalpy of formation, indicating thermodynamic stability; however, the* $Pd_{75}Pt_{15}Rh_{10}$ *alloy demonstrates the lowest miscibility. The heat capacity and thermal expansion coefficient calculated at 300 K are in good agreement with experimental data for pure palladium, platinum, and rhodium, confirming the validity of the chosen potential. Full sets of elastic constants and derived elastic moduli have been determined; all alloys satisfy mechanical stability criteria and exhibit ductile behavior, with* $Pd_{5}Pt_{70}Rh_{25}$ *being the most ductile. The results represent the first systematic molecular dynamics study of Pd-Pt-Rh ternary alloys and can be used for the design of next-generation catalytic and energy-related materials.*

Keywords: Molecular Dynamics, Quantum Sutton-Chen potential, ternary alloys, mechanical properties.

1. Introduction

Transition metals and their alloys constitute an essential class of materials underpinning numerous technological applications. Their remarkable mechanical strength, corrosion resistance, and catalytic performance make them indispensable in fields such as medicine, aerospace engineering, and micro-technologies. In particular, Pd, Pt, and Rh and their corresponding alloys are widely employed in automotive and space industries, medical devices, and dental applications. These metals have recently gained even greater prominence due to their critical role in automotive exhaust-gas catalysts, which are increasingly important as global efforts intensify to reduce CO_2 emissions and mitigate climate change [1]. Moreover, with the rapid expansion of hydrogen-based energy systems, Pd-, Pt-, and Rh-based materials have attracted substantial interest because of their exceptional hydrogen absorption and retention capacities [2]. The strategic importance of these elements has further stimulated advancements in recycling technologies, and the recovery of Pd, Pt, and Rh from spent automotive catalysts now represents a significant industrial sector [3,4].

Molecular dynamics (MD) simulations have played a central role in understanding metals and alloys at the atomic scale. MD allows for time-resolved analysis of thermodynamic, structural, and dynamical properties

---

Received 4 December 2025; revised 17 December 2025; accepted 5 January 2026.

(https:doi.org/……)

[5,6], providing access to interatomic forces derived from the gradients of appropriately chosen potential functions [7]. Classical MD simulations typically employ empirical many-body potentials; however, early formulations were often insufficient to capture the complex characteristics of metallic bonding. To address this, refined potentials incorporating local electronic density or volume-dependent many-body interactions were developed, enabling significantly improved representations of metallic cohesion [7-14].

Among these, the Sutton-Chen (SC) potential has been widely utilized due to its simple power-law functional form, computational efficiency, and ability to reproduce experimental lattice parameters, cohesive energies, and bulk moduli of FCC metals [15]. Nevertheless, the original SC potential was subsequently reparametrized by Kimura, Cagın, and colleagues to incorporate temperature-dependent physical properties more accurately. By fitting additional observables-including phonon frequencies at the X-point-and accounting for zero-point energy (ZPE), they formulated the Quantum Sutton-Chen (Q-SC) potential [16]. This enhanced potential has since been applied extensively to studies of glass formation, crystallization, surface energetics, cluster and nanowire behavior, and single-crystal plasticity in FCC metals [17-19].

Several notable investigations have highlighted the effectiveness of the Q-SC model. Kart H.H. et al. examined Pd, Ag, and their alloys, revealing distinct differences between predictions obtained from SC and Q-SC potentials [20]. Kart S.O. and collaborators further explored Pd-Ni systems in solid, liquid, and amorphous phases using both potentials, demonstrating superior accuracy with Q-SC [21]. Davoodi and Moradi investigated temperature effects on the mechanical behavior of ordered Pd_3Rh and $PdRh_3$ alloys [22], while Ning and Hu analyzed the strengthening induced by Ru and Ce in Pt-Pd-Rh systems [23]. Luyten et al. studied phase behavior in Pd-Pt-Rh alloys using MEAM potentials, reporting exothermic alloy-formation reactions across a range of compositions [24]. In addition, Sakamoto et al. examined hydrogen absorption thermodynamics in Pd-Pt-Rh ternary alloys, emphasizing their potential in hydrogen-storage applications [25]. Despite these efforts, studies focusing simultaneously on the thermal and mechanical behavior of Pd-Pt-Rh ternary systems remain limited compared to their binary counterparts.

To fill this gap, the present work provides a comprehensive theoretical investigation of four ternary alloys-$Pd_{15}Pt_{10}Rh_{75}$, $Pd_5Pt_{25}Rh_{70}$, $Pd_5Pt_{70}Rh_{25}$, and $Pd_{75}Pt_{15}Rh_{10}$-over a broad temperature range. We report detailed predictions of lattice parameters, cohesive energies, densities, enthalpies, heat capacities, thermal expansion coefficients, and elastic constants, along with derived quantities such as bulk, shear, and Young's moduli, Poisson's ratios, and G/B ratios. Furthermore, we evaluate ductility, brittleness, elastic response, and hardness for these compositions for the first time, providing new insights into the structure-property relationships of Pd-Pt-Rh ternary alloys.

2. Method of calculation

The empirical many-body Finnis-Sinclair force field includes a repulsive and an attractive term, proportional to the square root of the local density. Total potential energy of metals and alloys per atom in a system of N atoms is given by:

$$U_{tot} = \sum_i U_i = \sum_i \left[\sum_{j\neq i} \epsilon_{ij}\frac{1}{2}V\left(r_{ij}\right) - c_i\epsilon_{ij}\left(\rho_i\right)^{1/2}\right]. \qquad (1)$$

$V(r_{ij})$ is a pair wise repulsive term between the ith and jth atoms. Second term describes the many body cohesive term associated with atom i,

$$V\left(r_{ij}\right) = \left(\frac{a_{ij}}{r_{ij}}\right)^{n_{ij}}, \qquad (2)$$

and

$$\rho_i = \sum_{i\neq j} \emptyset\left(r_{ij}\right), \qquad (3)$$

$$\emptyset\left(r_{ij}\right) = \left(\frac{a_{ij}}{r_{ij}}\right)^{m_{ij}}. \qquad (4)$$

Where r_{ij} is the distance between the ith and jth atoms. a_{ij} is the length scale parameter leading to dimensionless arguments for $V(r_{ij})$ and ρ_i. Other parameters (namely c_{ij}, ε_{ij}, n_{ij}, and m_{ij}) are obtained by fitting the 0K properties, such as the zero-pressure condition, the cohesive energy, and the bulk modulus of the FCC pure metals. c_{ij} is a dimensionless parameter scaling the attractive term, ε_{ij} is an energy parameter obtained from experiments, and n_{ij}, m_{ij} are positive integer parameters with $n>m$. These integer parameters define the range of the two components of the potential. The values of the Q-SC potential parameters for Pd, Pt, and Rh are given in Table 1.

Table 1. The Q-SC potential parameters for Pd, Pt, and Rh pure metals [18,20].

Metal	Model	n	m	ε (eV)	c	a (A°)
Pd	Q-SC	12	6	0.32864E-2	148.205	3.8813
Pt	Q-SC	11	7	0.97894E-2	71.336	3.9163
Rh	Q-SC	13	5	0.24612E-2	305.499	3.7984

In this study, MD simulations are made for a supercell consisting of a 7x7x7 conventional unit cell. The algorithms of MD simulation are based on the extended Hamiltonian formalism, presented in the studies of Andersen [26], Parinello-Rahman [27], Nosé [28], Hoover [29], and Cagın and Pettitt [30]. The system is considered to be a cubic box with 1372 atoms, which is sufficient for statistics of the equilibrium properties, such as pressure, temperature, energy, etc. The simulation starts with atoms arbitrarily distributed on an FCC lattice subject to the periodic boundary conditions in three dimensions. A 5th-order gear predictor-corrector algorithm is used to integrate the equations of motion with a time step of 2 fs. The Parrinello-Rahman piston mass parameter is chosen as W=400, and the Nosé-Hoover parameter is set to Q=100. The cutoff distance for the interactions between the atoms is taken to be two lattice parameters to realize maximum capacity and speed of the calculations. However, the temperature effects are taken into account by extending the range an additional distance of half a lattice parameter. Three ensembles, namely HPN (constant enthalpy and constant pressure), TPN (constant pressure and constant temperature), and EVN (constant energy and constant volume), respectively, are used in the simulation. First, the system is heated from 0.1 K to the target temperature with increments of 200 K in the HPN ensemble. At each temperature, 2000 time steps are performed to equilibrate the system. In order to get more accurate values of the melting temperature, the system is heated up with increments of 10K near the melting temperature. Afterwards, the volume, density, and energy of the system are obtained in the TPN ensemble. 20000 additional steps are carried out for TPN dynamics. Finally, 50000 additional steps are performed in EVN ensemble conditions to obtain the elastic constants of the materials. The resultant zero-strain average matrix $\langle h_0 \rangle$ is used to obtain the pressure-dependent properties of the system in the EVN dynamics.

3. Results and discussion

3.1 Lattice parameters, cohesive energy, enthalpy, and density

Lattice parameters, cohesive energy, density, and enthalpy are evaluated in the TPN dynamics. The results for $Pd_{15}Pt_{10}Rh_{75}$, $Pd_5Pt_{25}Rh_{70}$, $Pd_5Pt_{70}Rh_{25}$, and $Pd_{75}Pt_{15}Rh_{10}$ alloys are given in Table 2. Since, to our knowledge, there exist no experimental data for ternary Pd-Pt-Rh alloys, we present the calculated results without comparison.

Table 2. Lattice parameter (a), density (ρ), cohesive energy (E_c), and enthalpy (H) for $Pd_{15}Pt_{10}Rh_{75}$, $Pd_5Pt_{25}Rh_{70}$, $Pd_5Pt_{70}Rh_{25}$, and $Pd_{75}Pt_{15}Rh_{10}$ alloys calculated from TPN ensemble at different temperatures using Q-SC potential parameters.

Metals	T (K)	a (Å)	ρ (g/cm^3)	H (kJ/mol)	E_c (kJ/mol)
$Pd_{15}Pt_{10}Rh_{75}$	0	3.813	13.49	-533.49	-533.28
	200	3.823	13.38	-528.24	-530.73
	400	3.834	13.27	-523.07	-528.06
	600	3.845	13.15	-517.84	-525.33
	800	3.856	13.04	-512.54	-522.52
	1000	3.868	12.91	-507.12	-519.60
$Pd_5Pt_{25}Rh_{70}$	0	3.826	14.95	-552.42	-552.18
	200	3.835	14.84	-547.22	-549.72
	400	3.845	14.73	-542.06	-547.05
	600	3.856	14.60	-536.84	-544.33
	800	3.867	14.48	-531.55	-541.54
	1000	3.878	14.35	-526.16	-538.63
$Pd_5Pt_{70}Rh_{25}$	0	3.879	19.05	-555.93	-555.68
	200	3.889	18.92	-550.78	-553.27

Table 2. (continued)

	400	3.899	18.77	-545.64	-550.63
	600	3.910	18.61	-540.44	-547.93
	800	3.921	18.45	-535.16	-545.14
	1000	3.933	18.29	-529.76	-542.24
$Pd_{75}Pt_{15}Rh_{10}$	0	3.868	13.69	-425.49	-425.32
	200	3.880	13.56	-420.31	-422.81
	400	3.893	13.42	-415.15	-420.15
	600	3.908	13.28	-409.90	-417.38
	800	3.923	13.13	-404.50	-414.49
	1000	3.939	12.97	-398.94	-411.42

In Fig. 1, one can notice that $Pd_5Pt_{70}Rh_{25}$ has the highest density depending on Pt concentration. Lattice parameters of $Pd_{75}Pt_{15}Rh_{10}$ and $Pd_5Pt_{70}Rh_{25}$ have nearly the same value at about 600 K, but the lattice parameter of $Pd_{75}Pt_{15}Rh_{10}$ slightly increases compared to $Pd_5Pt_{70}Rh_{25}$ alloy, depending on temperature. In Fig. 3, the enthalpy curve of $Pd_{75}Pt_{15}Rh_{10}$ has the highest values, which are in agreement with the information given in Fig. 2.

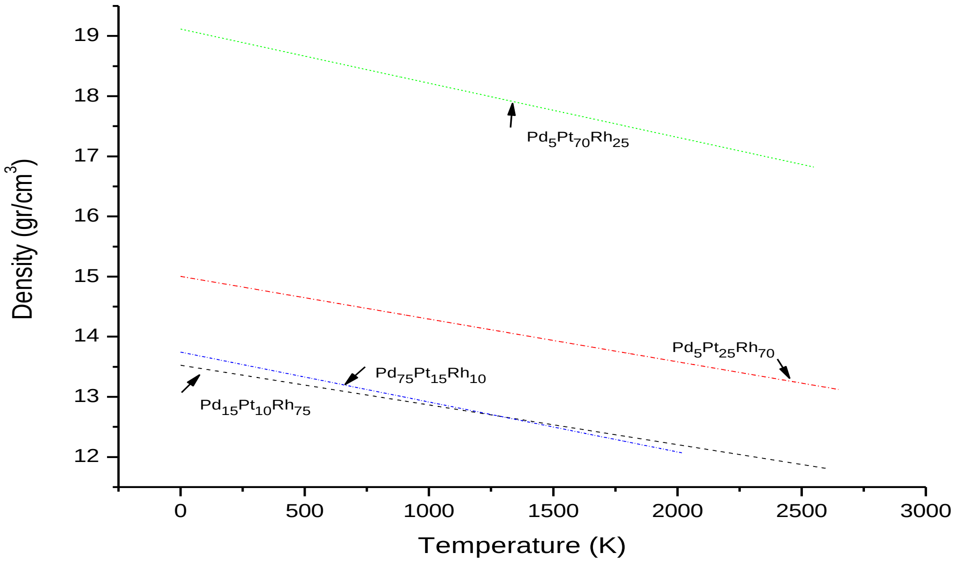

Fig. 1. Density of $Pd_{15}Pt_{10}Rh_{75}$, $Pd_5Pt_{25}Rh_{70}$, $Pd_5Pt_{70}Rh_{25}$ and $Pd_{75}Pt_{15}Rh_{10}$ alloys as a function of temperature for Q-SC potential parameters.

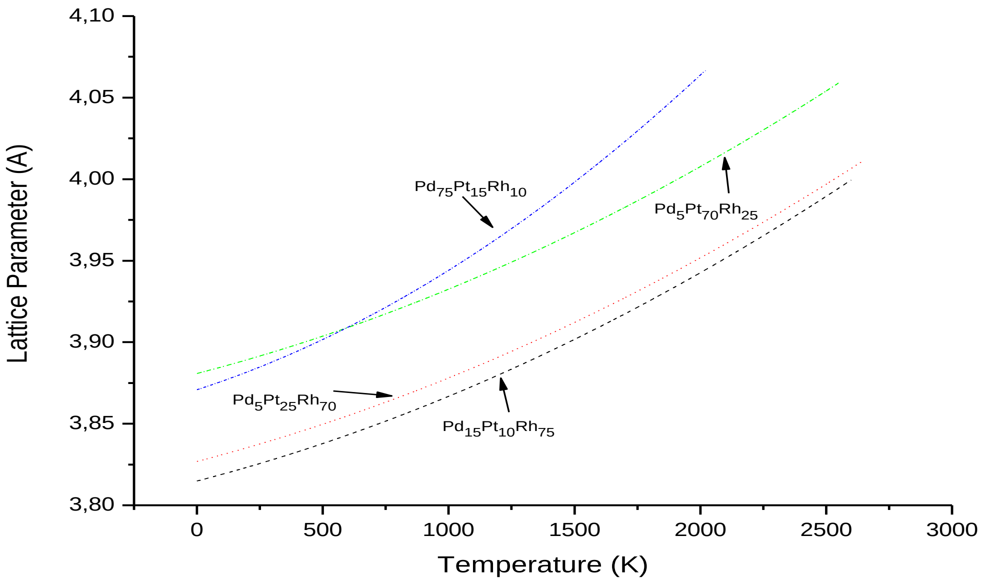

Fig. 2. Lattice parameters of $Pd_{15}Pt_{10}Rh_{75}$, $Pd_5Pt_{25}Rh_{70}$, $Pd_5Pt_{70}Rh_{25}$, and $Pd_{75}Pt_{15}Rh_{10}$ alloys as a function of temperature for Q-SC potential parameters.

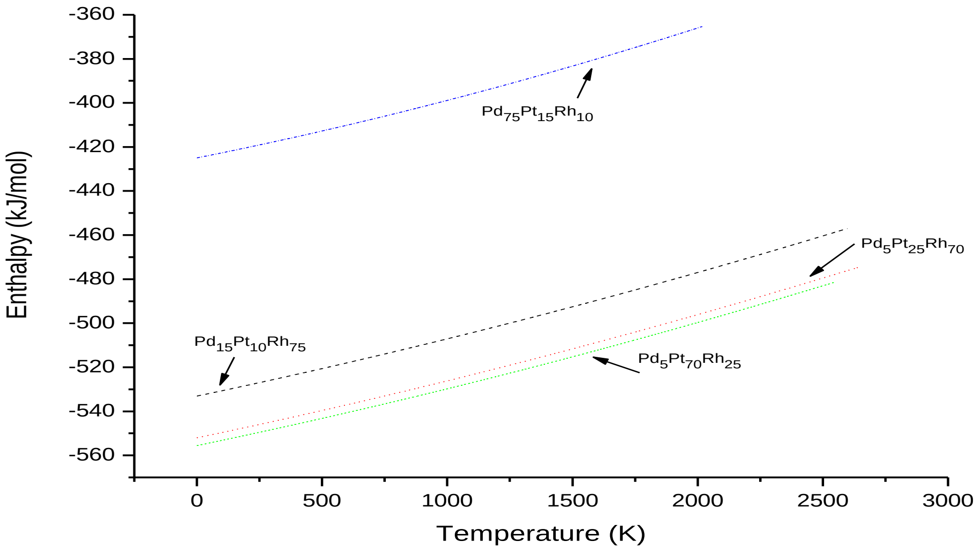

Fig. 3. Enthalpy of $Pd_{15}Pt_{10}Rh_{75}$, $Pd_5Pt_{25}Rh_{70}$, $Pd_5Pt_{70}Rh_{25}$, and $Pd_{75}Pt_{15}Rh_{10}$ alloys as a function of temperature for Q-SC potential parameters.

3.2 Specific heat capacity and thermal expansion coefficient

The calculated enthalpy results are fitted to a quadratic polynomial using the data below the melting temperature in order to investigate the specific heat capacity as a function of temperature. Fitted data lie between 200 and 2600 K for $Pd_{15}Pt_{10}Rh_{75}$, 200 and 2650 K for $Pd_5Pt_{25}Rh_{70}$, 200 and 2500 K for $Pd_5Pt_{70}Rh_{25}$, and 200 and 2020 K for $Pd_{75}Pt_{15}Rh_{10}$. The quadratic polynomial may be chosen as follows:

$$H(T) = a + bT + cT^2 \ (kJ\ mol^{-1}). \tag{5}$$

Where, T is the temperature. Specific heat capacity can be calculated by taking the first derivative of equation (5) as follows.

$$C_p(T) = \left(\frac{\partial H(T)}{\partial T}\right)_p. \tag{6}$$

We obtain a, b, and c from the fitted results of enthalpy data calculated from Q-SC potential parameters at each temperature. The coefficients of thermal expansion (a, b, and c) in Eq. (5), calculated by using the Q-SC potentials, are given in Table 3.

Table 3. Specific heat capacity calculated from Q-SC potential parameters for $Pd_{15}Pt_{10}Rh_{75}$, $Pd_5Pt_{25}Rh_{70}$, $Pd_5Pt_{70}Rh_{25}$, and $Pd_{75}Pt_{15}Rh_{10}$ alloys, and coefficients of the polynomial function used to find the heat capacity of alloys.

Metals	a	b x 10^{-4}	c x 10^{-6}	Potential Model	C_p (kJ mole $^{-1}$ K^{-1})
					Present Work
$Pd_{15}Pt_{10}Rh_{75}$	-533.079	239.200	2.064	Q-SC	0.0251584
$Pd_5Pt_{25}Rh_{70}$	-552.029	237.700	2.094	Q-SC	0.0250264
$Pd_5Pt_{70}Rh_{25}$	-555.560	236.300	2.156	Q-SC	0.0249236
$Pd_{75}Pt_{15}Rh_{10}$	-424.955	227.200	3.383	Q-SC	0.0247498

Experimental heat capacities of Pd, Pt, and Rh metals are 0.02598 kJ/mol K, 0.02586 kJ/mol K, and 0.02498 kJ/mol K, respectively [31]. It can be concluded from Table 3 that the simulated results for alloys and the experimental data given for metals are in good agreement at 300 K.

In order to examine the thermal expansion behavior, we have fitted the lattice parameter data below the melting temperature as a function of temperature to a quadratic polynomial similar to the heat capacity calculation:

$$a(T) = a + bT + cT^2 \,. \tag{7}$$

Thermal expansion coefficient is obtained by replacing the first derivative of Eq. (7) into Eq. (8),

$$\alpha_p(T) = -\frac{1}{a(T)}\left(\frac{\partial a(T)}{\partial T}\right)_p . \tag{8}$$

Table 4 includes the coefficients of Eq. (7), and the simulated results for thermal expansion coefficients (α) at 300 K. Experimental thermal expansion values of Pd, Pt and Rh metals are 1.18×10^{-5} K^{-1}, 0.88×10^{-5} K^{-1} and 0.82×10^{-5} K^{-1}, respectively [31], From Table 4, one can see that the simulated results for alloys and the experimental data given for metals are in good agreement.

Table 4. Thermal expansion coefficient calculated from Q-SC potential parameters for $Pd_{15}Pt_{10}Rh_{75}$, $Pd_5Pt_{25}Rh_{70}$, $Pd_5Pt_{70}Rh_{25}$, and $Pd_{75}Pt_{15}Rh_{10}$ alloys, and coefficients of the polynomial function used to find the thermal expansion coefficient of alloys.

Metals	a	b x 10^{-5}	c x10^{-8}	Potential Model	α_p x 10^{-5} (K^{-1})
					Present Work
$Pd_{15}Pt_{10}Rh_{75}$	3.81	4.00	1.19	Q-SC	1.2362
$Pd_5Pt_{25}Rh_{70}$	3.83	4.00	1.12	Q-SC	1.2208
$Pd_5Pt_{70}Rh_{25}$	3.88	4.00	1.17	Q-SC	1.2119
$Pd_{75}Pt_{15}Rh_{10}$	3.87	5.00	2.32	Q-SC	1.6520

3.3 Elastic constants, bulk modulus, shear modulus, and Young's modulus

The elastic constants of a solid provide information on the stability and stiffness of the material. We calculated the elastic constants by using the following fluctuation expression [32]:

$$C_{\alpha\beta\gamma\kappa} = \frac{\Omega_0}{k_B T}\left(\langle P_{\alpha\beta}P_{\gamma\kappa}\rangle - \langle P_{\alpha\beta}\rangle\langle P_{\gamma\kappa}\rangle\right) + \frac{2Nk_BT}{\Omega_0}\left(\delta_{\alpha\delta}\delta_{\beta\kappa} + \delta_{\alpha\kappa}\delta_{\beta\gamma}\right) + \langle \chi_{\alpha\beta\gamma\kappa}\rangle . \tag{9}$$

Here, the angular brackets symbolize averaging over time, and $\Omega_0=\det h_0$ is the reference volume for the model system. The first term indicates the contribution from the fluctuation of the microscopic stress tensor P_{ij}. The second term is the temperature correction term, which represents the kinetic energy contribution, and the last term denotes the contribution of the Born term to the elastic constants. Elastic constants are calculated by imposing an external strain on the crystal, relaxing any internal parameters to obtain the energy as a function of the strain, and numerically solving for the elastic constants as the curvature of the energy versus strain curve [32]. The largest contribution to the elastic constants comes from the Born term in Eq. (9).

In this work, we have calculated the elastic constants from EVN simulations of 50000 steps for each alloy below the corresponding melting point. Bulk modulus (B), shear modulus (G_v, G_R, and G), G/B ratio, Cauchy pressure (C_{12}-C_{44}), Cauchy's ratio (C_{12}/C_{44}), Poisson ratio (ν), and Young's modulus (Y) have been calculated by using C_{11}, C_{12}, and C_{44} elastic constants.

The bulk modulus can be determined from:

$$B = \frac{(C_{11}+2C_{12})}{3} \tag{10}$$

In addition, shear modulus, G_v, G_R and G are calculated from the Voigt-Reuss-Hill arithmetic approximation based on the Voigt and Reuss bounds [33]:

$$G_V = \frac{C_{11}-C_{12}+3C_{44}}{5} \tag{11}$$

$$G_R = \frac{5(C_{11}-C_{12})C_{44}}{4C_{44}+3(C_{11}-C_{12})}. \tag{12}$$

The arithmetic average of Voigt and Reuss bounds is called as Voigt-Reuss-Hill approximations. The Voigt-Reuss-Hill arithmetic approximation based on the Voigt and Reuss bounds have been used for G, ν and Y [34]:

$$G = \frac{G_V+G_R}{2}. \tag{13}$$

Poisson's ratio [35] can be determined from:

$$\nu = \frac{C_{12}}{C_{11}+C_{12}}. \tag{14}$$

From the calculated values of the bulk modulus and Poisson's ratio, we have also estimated the Young modulus:

$$Y = 3B(1-2\nu). \tag{15}$$

Results are listed in Tables 5, 6, 7, and 8 for all the alloys studied.

To our knowledge, no experimental data exist for the calculated properties in Tables 5, 6, 7, and 8 for $Pd_{15}Pt_{10}Rh_{75}$, $Pd_5Pt_{25}Rh_{70}$, $Pd_5Pt_{70}Rh_{25}$, and $Pd_{75}Pt_{15}Rh_{10}$ alloys. Therefore, our simulated results are given without comparison.

Table 5. Elastic constants C_{11}, C_{12}, and C_{44} (in GPa) calculated from Q-SC potential parameters and Bulk modulus (in GPa), (C_{12}/C_{44}) Cauchy's ratio, Cauchy pressure (C_{12}-C_{44}) (in GPa), G_v, G_R and G shear modulus (in GPa) based on using Voigt-Reuss-Hill arithmetic approximation, (ν) Poisson's ratio and (Y) Young modulus (in GPa) calculated by using elastic constants for $Pd_{15}Pt_{10}Rh_{75}$ alloy.

Alloys	$Pd_{15}Pt_{10}Rh_{75}$					
T(K)	C_{11}(GPa)	C_{12}(GPa)	C_{44}(GPa)	B(GPa)	C_{12}-C_{44}	C_{12}/C_{44}
0	262.009	183.327	118.781	209.554	64.545	1.543
200	296.911	197.603	130.472	230.705	67.131	1.515
400	285.347	192.37	123.469	223.362	68.901	1.558
600	274.278	186.234	116.93	215.582	69.304	1.593
800	263.22	180.022	109.507	207.754	70.515	1.644
1000	251.783	174.780	102.934	200.448	71.847	1.698

T(K)	G_v	G_R	G	G/B	ν	Y
0	87.005	65.708	76.357	0.364	0.4117	111.073
200	98.145	79.024	88.584	0.384	0.3996	138.991
400	92.677	74.273	83.475	0.374	0.4027	130.417
600	87.767	70.335	79.051	0.367	0.4044	123.649
800	82.344	66.248	74.296	0.358	0.4061	116.989
1000	77.161	61.659	69.410	0.346	0.4097	108.554

Table 6. Elastic constants C_{11}, C_{12}, and C_{44} (in GPa) calculated from Q-SC potential parameters and Bulk modulus (in GPa), (C_{12}/C_{44}) Cauchy's ratio, Cauchy pressure (C_{12}-C_{44}) (in GPa), G_v, G_R, and G shear modulus (in GPa) based on Voigt-Reuss-Hill arithmetic approximation, (ν) Poisson's ratio, and (Y) Young modulus (in GPa) calculated by using elastic constants for $Pd_5Pt_{25}Rh_{70}$ alloy.

Alloys	$Pd_5Pt_{25}Rh_{70}$					
T(K)	C_{11}(GPa)	C_{12}(GPa)	C_{44}(GPa)	B(GPa)	C_{12}-C_{44}	C_{12}/C_{44}
0	265.709	189.235	115.728	214.726	73.507	1.635

Table 6. (continued)

Alloys	$Pd_5Pt_{25}Rh_{70}$					
T(K)	C_{11}(GPa)	C_{12}(GPa)	C_{44}(GPa)	B(GPa)	C_{12}-C_{44}	C_{12}/C_{44}
200	307.852	207.829	131.716	241.170	76.114	1.578
400	297.161	202.092	125.242	233.781	76.850	1.614
600	285.585	196.206	118.029	225.999	78.177	1.662
800	273.969	190.150	111.249	218.089	78.900	1.709
1000	262.986	183.856	104.007	210.233	79.849	1.768

T(K)	G_v	G_R	G	G/B	V	Y
0	84.731	63.916	74.324	0.346	0.4160	108.284
200	99.034	79.659	89.347	0.370	0.4030	140.333
400	94.159	75.725	84.942	0.363	0.4048	133.552
600	88.693	71.255	79.974	0.354	0.4072	125.778
800	83.513	66.945	75.229	0.345	0.4097	118.160
1000	78.230	62.977	70.604	0.336	0.4115	111.688

Table 7. Elastic constants C_{11}, C_{12}, and C_{44} (in GPa) calculated from Q-SC potential parameters and Bulk modulus (in GPa), (C_{12}/C_{44}) Cauchy's ratio, Cauchy pressure (C_{12}-C_{44}) (in GPa), G_v, G_R, and G shear modulus (in GPa) based on Voigt-Reuss-Hill arithmetic approximation, (ν) Poisson's ratio, and (Y) Young modulus (in GPa) calculated by using elastic constants for $Pd_5Pt_{70}Rh_{25}$ alloy.

Alloys	$Pd_5Pt_{70}Rh_{25}$					
T(K)	C_{11}(GPa)	C_{12}(GPa)	C_{44}(GPa)	B(GPa)	C_{12}-C_{44}	C_{12}/C_{44}
0	276.975	204.986	103.884	228.982	101.102	1.973
200	301.515	213.337	116.799	242.730	96.538	1.827
400	290.902	206.82	110.93	234.847	95.89	1.864
600	273.661	194.736	104.091	221.045	90.645	1.871
800	255.470	182.23	98.076	206.643	84.154	1.858
1000	240.423	172.455	91.726	195.111	80.729	1.880

T(K)	G_v	G_R	G	G/B	V	Y
0	76.728	59.212	67.970	0.297	0.4253	102.607
200	87.715	70.375	79.045	0.326	0.4144	124.716
400	83.374	67.009	75.192	0.320	0.4155	119.021
600	78.240	62.891	70.566	0.319	0.4157	111.738
800	73.494	58.683	66.088	0.320	0.4163	103.732
1000	68.629	54.611	61.620	0.316	0.4177	96.358

Table 8. Elastic constants C_{11}, C_{12}, and C_{44} (in GPa) calculated from Q-SC potential parameters and Bulk modulus (in GPa), (C_{12}/C_{44}) Cauchy's ratio, Cauchy pressure (C_{12}-C_{44}) (in GPa), G_v, G_R, and G shear modulus (in GPa) based on Voigt-Reuss-Hill arithmetic approximation, (ν) Poisson's ratio, and (Y) Young modulus (in GPa) calculated by using elastic constants for $Pd_{75}Pt_{15}Rh_{10}$ alloy.

Alloys	$Pd_{75}Pt_{15}Rh_{10}$					
T(K)	C_{11}(GPa)	C_{12}(GPa)	C_{44}(GPa)	B(GPa)	C_{12}-C_{44}	C_{12}/C_{44}
0	215.041	152.953	87.581	173.649	65.372	1.746
200	231.425	159.166	94.968	183.252	64.198	1.676
400	216.725	149.594	88.115	171.971	61.479	1.698
600	199.845	137.633	81.724	158.370	55.909	1.684
800	185.034	128.664	74.491	147.454	54.173	1.727
1000	172.576	120.964	69.671	138.168	51.293	1.736

T(K)	G_v	G_R	G	G/B	V	Y
0	64.966	50.669	57.818	0.333	0.4156	102.607
200	71.433	57.507	64.470	0.352	0.4075	124.716
400	66.295	53.401	59.848	0.348	0.4084	119.021
600	61.477	49.502	55.489	0.350	0.4078	111.738
800	55.969	44.951	50.460	0.342	0.4102	103.732
1000	52.125	41.473	46.799	0.333	0.4121	96.358

Elastic constant and bulk modulus curves calculated from the Q-SC potential are given in Fig. 4, 5, 6, and 7. When we examine Fig. 4, 5, and 6, we identify that the elastic constants of $Pd_{75}Pt_{15}Rh_{10}$ are much weaker compared to those of other alloys.

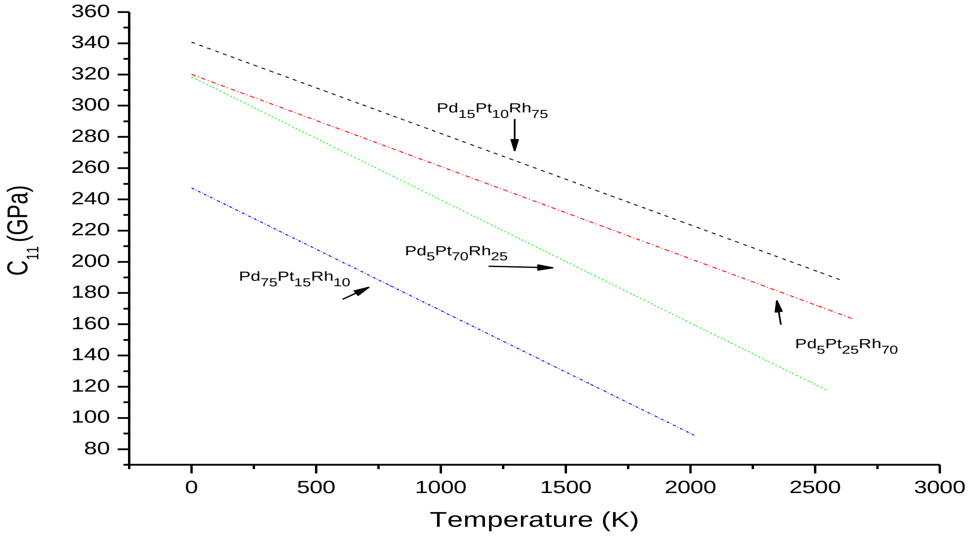

Fig. 4. Elastic constants C_{11} of $Pd_{15}Pt_{10}Rh_{75}$, $Pd_5Pt_{25}Rh_{70}$, $Pd_5Pt_{70}Rh_{25}$ and $Pd_{75}Pt_{15}Rh_{10}$ alloys as a function of temperature for Q-SC potential parameters.

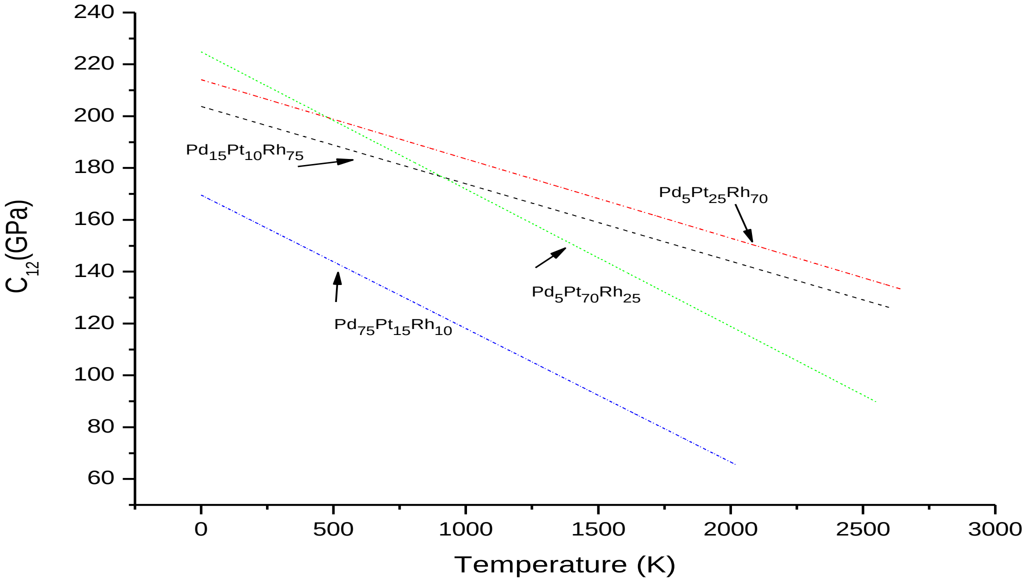

Fig. 5. Elastic constants C_{12} of $Pd_{15}Pt_{10}Rh_{75}$, $Pd_5Pt_{25}Rh_{70}$, $Pd_5Pt_{70}Rh_{25}$, and $Pd_{75}Pt_{15}Rh_{10}$ alloys as a function of temperature for Q-SC potential parameters.

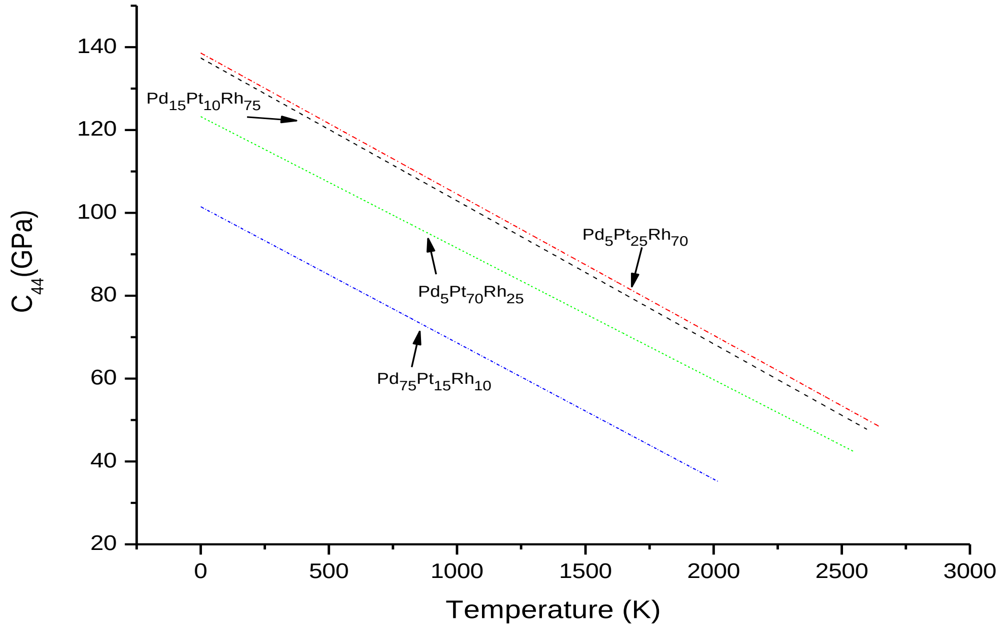

Fig. 6. Elastic constants C_{44} of $Pd_{15}Pt_{10}Rh_{75}$, $Pd_5Pt_{25}Rh_{70}$, $Pd_5Pt_{70}Rh_{25}$ and $Pd_{75}Pt_{15}Rh_{10}$ alloys as a function of temperature for Q-SC potential parameters.

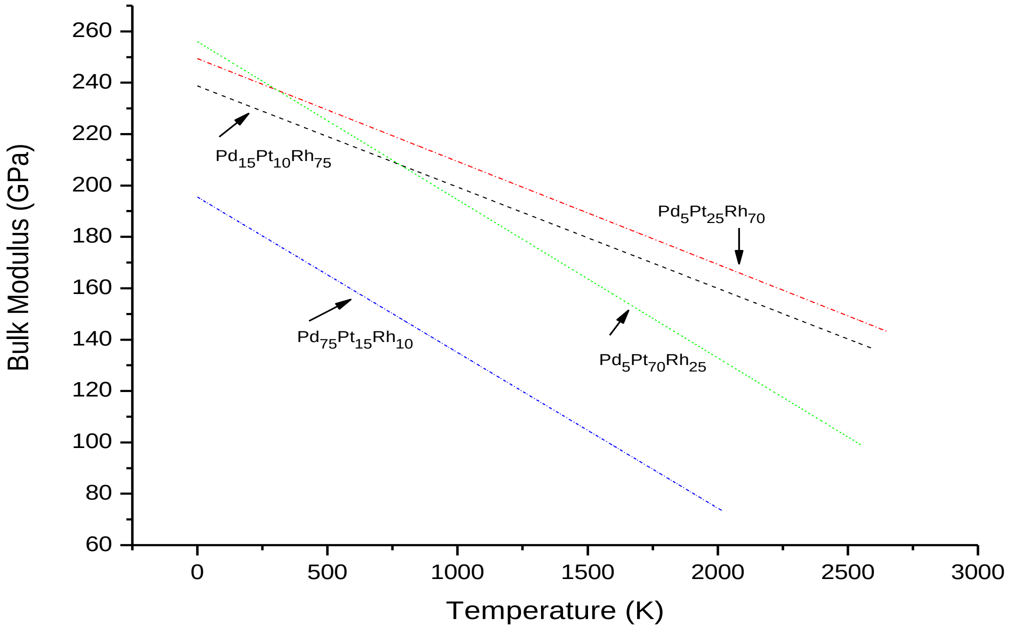

Fig. 7. Bulk modulus B of $Pd_{15}Pt_{10}Rh_{75}$, $Pd_5Pt_{25}Rh_{70}$, $Pd_5Pt_{70}Rh_{25}$, and $Pd_{75}Pt_{15}Rh_{10}$ alloys as a function of temperature for Q-SC potential parameters.

The average atomic bond strengths of $Pd_{15}Pt_{10}Rh_{75}$, $Pd_5Pt_{25}Rh_{70}$, $Pd_5Pt_{70}Rh_{25}$, and $Pd_{75}Pt_{15}Rh_{10}$ alloys based on the calculated bulk modulus (B) by using the Q-SC potential parameters follow the order from largest to smallest as $Pd_5Pt_{70}Rh_{25} > Pd_5Pt_{25}Rh_{70} > Pd_{15}Pt_{10}Rh_{75} > Pd_{75}Pt_{15}Rh_{10}$. The experimental bulk modulus of Pd, Pt, and Rh metals is 181GPa, 278GPa, and 270 GPa [35,36], respectively. It seems that Pt has the highest average atomic bond strength. Thus, the average atomic bond strength of $Pd_5Pt_{70}Rh_{25}$ is larger compared to that of the other alloys, depending on Pt concentration.

The shear modulus (G) is related to the resistance of plastic deformation, while the bulk modulus (B) shows resistance to bond rupture. Therefore, it was reported that the ductile/brittle behavior of materials could be related empirically to their elastic constants by the ratio of G/B or Poisson's ratio. If $G/B > 0.5$ or $\nu < 1/3$, the material is brittle. Otherwise, the material is ductile [37, 38]. It can be concluded from the present study that G/B is smaller than 0.,5 and Poisson's ratio is larger than 1/3 for the alloys studied. It can be seen from the ratio G/B or Poisson's ratio (ν) that all alloys behave in a ductile manner.

Pettifor has suggested that the Cauchy pressure, which reflects the ductile/brittle behaviors of materials, could be used to describe the angular character of atomic bonding in metals and compounds. The Cauchy pressure is positive for metallic bonding, while it is negative for directional bonding. The ductile materials show positive Cauchy pressure; otherwise, the material is brittle [39]. If one looks at the Cauchy pressure of the alloys studied in the present work, it can be seen that all of them are positive. So, all of our simulated alloys are ductile in nature.

4. Conclusion

In this work, we have presented a wide range of properties of $Pd_{15}Pt_{10}Rh_{75}$, $Pd_5Pt_{25}Rh_{70}$, $Pd_5Pt_{70}Rh_{25}$, and $Pd_{75}Pt_{15}Rh_{10}$ alloys. We have tried to understand the agreement of our results with experimental values of their metallic components.

It is seen in Fig. 6 that all of the enthalpy plots of studied alloys are in the negative region. It means that all of the alloys have exothermic behavior. It indicates that all the studied alloys are miscible, although $Pd_{75}Pt_{15}Rh_{10}$ has the least miscibility compared to the others. This information explains why the lattice parameters curve of $Pd_{75}Pt_{15}Rh_{10}$ sharply increases compared to those of other alloys (see Fig. 2).

In this study, we have calculated the bulk modulus (B), Cauchy pressure (C_{12}-C_{44}), Cauchy's ratio (C_{12}/C_{44}), shear modulus (G_v, G_R, and G), G/B ratio, Poisson's ratio (ν), and Young's modulus (Y) by using C_{11}, C_{12}, and C_{44} elastic constants results. Examining these results, we can say that all of the studied alloys are ductile. Depending on the G/B ratio, we can order the ductility of alloys as $Pd_5Pt_{70}Rh_{25} > Pd_{15}Pt_{10}Rh_{75} > Pd_5Pt_{25}Rh_{70} > Pd_{75}Pt_{15}Rh_{10}$.

During the study, we could not identify an eutectic alloy concentration that is possible between noble metal alloys. In our guess, Rh is the compound that prevents the alloys to be formed in eutectic form.

Funding

This work does not receive any funding.

Conflict of interest

The authors declare no conflict of interest.

Acknowledgements

This study is supported by SAÜ BAP 2007-02-02-004 Project of Sakarya University-TURKEY.

References

1 Davis, S., Salisbury, T., Pinson, G., Christianson, R., Berlin, M., Downey, J., Gleason, W., James, R., Rosenberg, E., Gleason, K., Hiebert, R., Mccloskey, J. (2012). Improved Palladium Coatings for Hydrogen Purification Membranes. *Energy Technology 2012: Carbon Dioxide Management and Other Technologies*. ch39, 323-330. DOI: 10.1002/9781118365038

2 James, R., Brenner., Gaurav, B., Pareen, V. (2008). Hydrogen purification with palladium and palladium alloys on porous stainless steel membranes. *Int. J. Oil, Gas and Coal Technology*. 1, 1/2, 1020089-125. DOI: 10.1504/IJOGCT.2008.016734

3 Mycka, L., Lewandowski, D., Anyszkiewicz, J., Charasińska, J. (2022). Analysis of the Possibilities of Including Recycling of Auto-motive Catalytic Converters in the Cu-Pb-Fe Alloy Converting Process. *World of Metallurgy - ERZMETALL*. 75, 5, 266 - 272.

4 Song, Si J., Nguyen, Viet N. H., Lee, M. S. (2024). Separation of Palladium, Platinum and Rhodium from Metallic Mixture by Selective Dissolution with Hydrochloric Acid Solutions Containing Oxidizing Agents. *Mineral Processing and Extractive Metallurgy Review*, 45, 4, 356 - 367, DOI: 10.1080/08827508.2023.2176852

5 Haile J.M. (1992) *Molecular Dynamics Simulation (Book).* A Wiley-Interscience Publication, New York.

6 Davoodi J., Ahmadi M., Rafii-Tabar H. (2010). Molecular dynamics simulation study of thermodynamic and mechanical properties of the Cu-Pd random alloy. *Materials Science and Engineering: A*. 527(16-17), 4008-4013.

7 Ciftci Y.O., Colakoglu K., Ozgen S., Kazanc, S. (2007). The calculation of some thermoelastic properties and pressure-temperature (P-T) diagrams of Rh and Sr using molecular dynamics simulation. *Journal of Physics: Condensed Matter*. 19(32), 326204, DOI: 10.1088/0953-8984/19/32/326204

8 Cagın T., Dereli G., Uludogan M., Tomak M. (1999). Thermal and mechanical properties of some fcc transition metals. *Physical Review B*. 59, 3468, DOI: https://doi.org/10.1103/PhysRevB.59.3468

9 Daw M.S., Baskes M.I. (1984) Embedded-atom method: Derivation and application to impurities, surfaces, and other defects in metals. *Physical Review B*. 29, 6443. DOI: 10.1103/PHYSREVB.29.6443

10 Finnis M.W., Sinclair J.E. (1984) A Simple Empirical N-Body Potential for Transition Metals. *Philosophical Magazine A*. 50, 45. DOI: http://dx.doi.org/10.1080/01418618408244210

11 Ercolessi F., Parrinello M., Tosatti E. (1988). *Phil. Mag.* A, 58, 213.

12 Sutton A.P., Chen J. (1990). Long-range Finnis-Sinclair potentials. *Philosophical Magazine Letters*. 61(3), 139-146. DOI: https://doi.org/10.1080/09500839008206493

13 Ackland G. J., Finnis M.W. (1986). *Philosophical Magazine A*. 54(2), 301.

14 Rafii-Tabar H., Sutton A.P. (1991). Long-Range FinnisSinclair Potentials for Fcc Metallic Alloys. *Philosophical Magazine Letters*. 63(4), 217-224, DOI: http://dx.doi.org/10.1080/09500839108205994

15 Kob W. (1999). *Journal of Physics: Condensed Matter*, 11(10), R85.

16 Cagın T., Qi Y., Li H., Kimura Y., İkeda H., Johnson W.L., Goddard W.A. (1999). *Jr.,MRS Symp. Ser.* 554, 43.

17 Qi Y., Cagın T., Kimura Y., Goddard III W.A. (1999). Molecular-dynamics simulations of glass formation and crystallization in binary liquid metals: Cu-Ag and Cu-Ni. *Physical Review B*. 59, 3527, DOI: https://doi.org/10.1103/PhysRevB.59.3527

18 Qi, Y., Cagın, T., Kimura, Y., Goddard III W. A. J. (2002). *Comp. Aided Mater.* 8, 233-243

19 Lee H.J., Cagın T., Johnson W.L., Goddard III, W.A. (2003). *J. Chem. Phys.* 119, 9858.

20 Kart H.H., Tomak M., Uludogan M., Cagın T. (2005). *Computational Materials Science*, 32, 107-117.

21 Ozdemir Kart S., Tomak M., Uludogan M., Cagın T. (2006). *Turk J. Phys.* 30, 319-327

22 Davoodi J., Moradi J. (2011). *World Academy of Science, Engineering and Technology*. 54, 354-358.

23 Ning Y., Hu X. (2003). *Platinum Metals Review*. 47, (3), 111-119, DOI: https://doi.org/10.1595/003214003X473122122

24 Luyten J., De Keyzer J., Wollants P., Creemers C. (2009). *Computer Coupling pf Phase Diagrams and Thermochemistry*. 33, 370-376.

25 Sakamoto Y., Ohira K., Kokubu M., Flanagan T.B. (1997). *Journal of Alloys and Compounds*. 253-254, 212-215

26 Andersen H.C. (1980). *J. Chem. Phys.* 72, 2384-2393, DOI: https://doi.org/10.1063/1.439486

27 Parinello M., Rahman A. (1980). Molecular dynamics simulations at constant pressure and/or temperature. *Phys. Rev. Lett.* 45, 1196

28 Nosé S. (1984). A unified formulation of the constant temperature molecular dynamics methods. *J. Chem. Phys.* 81, 511-519, DOI: https://doi.org/10.1063/1.447334

29 Hoover W.G. (1985). Canonical dynamics: Equilibrium phase-space distributions. *Physical Review A*. 31, 1695, DOI: https://doi.org/10.1103/PhysRevA.31.1695

30 Cagın T., Pettitt B.M. (1991). Molecular dynamics with a variable number of molecules. *Molecular Physics*. 72(1), 169-175, DOI: https://doi.org/10.1080/00268979100100111

31 Vines R.F., Wise E.M. (1941). *The Platinum Metals and Their Alloys, The International Nickel Comp.* New York, (CP)

32 Cagın T., Ray J.R. (1988). *Phys. Rev.* A 38, 7940

33 Mehl M.J., Papaconstantopolos D.A. (1996). *Phys. Rev. B* 54, 4519

34 Luo F., Chen X.R., Cai L.C., Wu Q. (2011). *J. At. Mol. Sci.* 2, 10-19

35 Simmons G., Wang H. (1971). *Single Crystal Elastic Constants and Calculated Aggregated Properties, MIT Press*, Cambridge

36 Singh N. (1999). *Pramana J. Phys.* 52, 511

37 Baria J.K., (2004). *Czech. J. Phys.* 54 469-484

38 Chen K., Zhao L.R., Tse J.S., Rodgers J.R. (2004). *Physics Letters A*, 331, 400-403

39 Vitos L., Korzhavyi P.A., Johansson B. (2002). Elastic Property Maps of Austenitic Stainless Steels. *Physical Review Letters*, 88(15), 155501-1, DOI: https://doi.org/10.1103/PHYSREVLETT.88.155501

40 Pettifor D. G.(1992). Theoretical Predictions of Structure and Related Properties of Intermetallics. *Materials Science and Technology*, 8, 345-349, DOI: https://doi.org/10.1179/mst.1992.8.4.345

AUTHORS' INFORMATION

Zhangabay Turar - MSc student, Department of Physics, Sakarya University; ORCID iD: https://orcid.org/0009-0004-6202-112X; (e-mail: zhangabay.turar@ogr.sakarya.edu.tr Phone: +905376890526)

Ali Coruh - Prof.Dr, Department of Physics, Sakarya University, Sakarya, Turkey; SCOPUS Author ID: 24460990900 ORCID iD: https://orcid.org/0000-0002-7362-6173 (e-mail: coruh@sakarya.edu.tr Phone: +9053555943390)

Arystanbek Kussainov - Researcher of Protective and Functional Coatings Scientific Center, D. Serikbayev East Kazakhstan Technical University; Institute of Composite Materials LLP, Ust-Kamenogorsk, Kazakhstan; SCOPUS Author ID: 59515031200. (e-mail: arys20055@gmail.com)

Rakhmetova Mairagul - Dr. Department of Plasma Physics and Computer Physics, Al-Farabi Kazakh National University, Almaty,Kazakhstan/ Department of Physics and Technical disciplines, Kh. Dosmukhamedov Atyrau University, Atyrau, Kazakhstan, ORCID iD: https://orcid.org/0000-0003-4529-0999 (e-mail: maira_12_05@mail.ru)

ORIGINAL STUDY

THE EFFECT OF WC-12CO POWDER PARTICLE SIZE ON PROPERTIES OF A HIGH VELOCITY OXYGEN-FUEL SPRAYING COATING

Kussainov A.E.,[1,2] Magazov N.M.,[1] Abizhanova I.K.,[1] Kuanyshbai R.M.[1]

[1]Protectivie and Functional Coatings Scientific Center, Daulet Serikbayev East Kazakhstan Technical University Ust-Kamenogorsk, Kazakhstan
[2]Institute of Composite Materials LLP, Ust-Kamenogorsk, Kazakhstan
*Corresponding author: arys20055@gmail.com

Abstract. *In the petroleum industry, erosion and corrosion of critical components such as valves and seat rings cause serious operational challenges. To minimize these problems, thermal spray coatings are widely used, especially those created using high velocity oxygen flame (HVOF) technology. These coatings are widely recognized for their high wear resistance and ability to perform effectively under extreme conditions. This study investigates the effect of powder particle size distribution on the structural, mechanical and tribological properties of WC-12Co coatings produced by HVOF. Three powder size fractions are considered in the study: 0-20 µm, 30-40 µm and* 40-50 *µm. Stainless steel substrates were coated and the resulting coatings were analyzed for porosity, hardness, wear resistance and microstructure using scanning electron microscopy (SEM), hardness measurements and tribological tests. The results showed that finer powder fractions resulted in denser coatings with lower porosity and higher hardness values reaching 890 HV for the 40-50 µm fraction. Tribological tests showed that coatings from the 40-50 µm fraction exhibited the highest wear resistance. These results emphasize the importance of selecting optimal powder fractions to improve the performance of WC-12Co coatings, making them ideal for aerospace and petroleum applications where durability and wear resistance are critical.*

Keywords: WC-12Co coatings, High-Velocity Oxygen-Fuel Spraying (HVOF), wear resistance, friction coefficient.

1. Introduction

Erosion and corrosion of valves in the oil industry is a serious problem due to the presence of suspended sand particles in the oil and gas flow. This leads to erosion of critical components such as valves and seat rings, which in turn increases operating costs [1]. Advanced thermal spraying techniques have been developed to address this problem in harsh operating environments such as high-pressure subsea operations [2, 3].

These advanced coating technologies significantly improve component wear resistance, reduce the risk of accidents and extend equipment life. The high adhesion and density of the coating provides excellent protection against erosion and corrosion, which is especially important in extreme operating conditions. Thus, the use of thermal spray technology in the oil industry is an effective solution for extending equipment life and reducing operating costs.

HVOF technology is widely used for surface hardening. Compared with other methods, HVOF is characterized by extremely low heat generation, high flame speed and relatively low temperature, which makes it an important technology for obtaining high performance wear and corrosion resistant coatings. It has found wide application in the surface treatment of pumps, valves, impellers and bearings.

Tungsten carbide (WC) based coatings reinforced with a cobalt matrix (WC-12Co) and obtained by high velocity oxyfuel spraying (HVOF) are a promising material for use under high wear load conditions. Studies show that the HVOF technique can produce coatings with high density and low porosity, which improves the mechanical properties and wear resistance of such materials [4, 5]. The specific combination of tungsten carbide hardness and cobalt plasticity creates coatings that can effectively resist abrasive wear and corrosion

---

Received 4 August 2025; revised 17 December 2025; accepted 5 January 2026.

(https:doi.org/……)

even in aggressive environments, making them ideal for use in the aerospace and petroleum industries [6-8]. WC tungsten carbide coatings are widely used in various industries to protect key mechanisms [9], including industrial gas turbines, ball valves, and aircraft landing gear shafts [10]. By optimizing the HVOF spraying process, WC coatings can be achieved that exhibit strong bonding, excellent density, high carbide phase content, corrosion resistance, and excellent wear resistance [11-15]. Among the various WC tungsten carbide coatings, WC-Co coatings, in which cobalt (Co) acts as a bonding component, are the most common. The presence of cobalt Co helps to increase the bond strength between the WC solid phase and the substrate, which significantly affects the performance of the coating. In addition, WC-12Co coatings exhibit high compressive strength and modulus of elasticity, which favors their application in components subjected to high mechanical stresses. An important aspect is also the low coefficient of thermal expansion of this material, which prevents the occurrence of thermal stresses and cracks under changing temperature operating conditions [16]. Thus, WC-12Co coatings obtained by the HVOF method offer an excellent combination of mechanical and physicochemical properties, which confirms their high technological and commercial value.

The purpose of this study is to investigate the effect of the fractions of initial powders on the microstructure, phase composition, hardness and wear resistance of WC-12Co metal-ceramic coatings.

2. Materials and methods

Stainless steel 12X18H10T was used as a substrate material, which was pre-polished and sandblasted with electrocorundum under pressure of 0.6 MPa to increase the adhesion of the coating with the substrate. the chemical composition of the substrate is given in Table 1.

WC-12Co powder produced by XTC company (China), ISO 9001 certification, was used for spraying. The powder was sieved on a Retsch AS 300 sieving machine using sieves with sizes 0-20, 30-40 and 40-50.

Table 1. Chemical composition of 12Cr18Ni10T stainless steel (wt %).

Fe	Cr	Ni	Mn	Ti	Si	Cu	C	P	S
67	17-19	9-11	2	0.4-1	0.8	0.3	0.12	0.035	0.02

WC-12Co coating was deposited on the substrate using a LH-5000 (China) HVOF, the specific parameters and codes of the experiments used in the spraying process are summarized in Table 2.

Table 2. Spraying modes of WC-Co coatings.

Code	A1	A2	A3
Fraction size	0-20	30-40	40-50
Parameter modes on the gas control panel	Optimal values		
Propane pressure	2.9 bar		
Oxygen pressure	5 bar		
Compressed air pressure	3.2 bar		

The HVOF principle is that large volume combustion gases are fed into the combustion chamber. Combustion takes place inside at very high pressure. They are then fed into a long confining nozzle or cylinder through which they exit the device, creating a supersonic gas jet with very high particle velocities. The powder particles are introduced into the stream, heated and directed towards the substrate on which the coating is formed (see Fig. 1). At such a high velocity, the particles have a shorter residence time in the high-temperature gas environment, which makes it possible to obtain coatings with very low porosity, low oxidation coefficient, and high adhesion to the substrate.

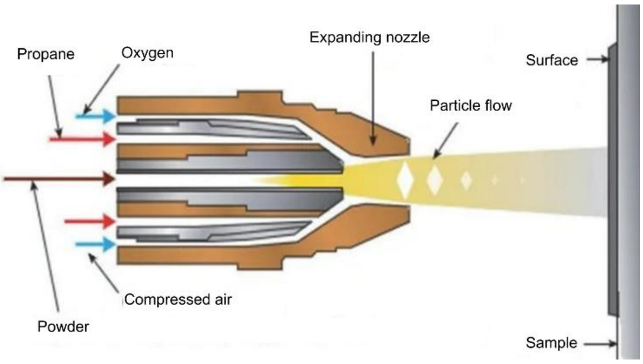

Fig. 1. Schematic representation of the HVOF method.

Structural studies, porosity and microhardness measurements of the coatings were performed on cross-sectional micro-sections. The cross-sectional of the coatings was characterized using TESCAN Vega 4 LMH scanning electron microscopy (TESCAN, Brno, Czech Republic). Measurement of microhardness of samples was carried out on the cross-section of coatings (10 measurements for each type of coatings) on a microhardness tester GOST R ISO 6507-1-2007 Metolab 502 (Metolab, Russia) at load on the indenter m=500 g and dwell time 10s. Tribological tests for friction and wear were performed on a TRB³ tribometer (Anton-Paar, Buchs, Switzerland) according to the standard "ball-disk" method, where a ball with a diameter of 6.0 mm made of 100Cr6 coated steel was used as a counterbody, with a load of 10 N, linear velocity of 3 cm/min and a path length of 100 m.

3. Results and discussion

3.1 Morphology

The microstructure of WC-12Co powder material deposited by gas-thermal spraying is shown in Fig. 2 Two detectors were used: SE (secondary electrons) and BSE (backscattered electrons). The image obtained with the backscattered electron (BSE) detector shows the distribution of WC and Co: lighter areas correspond to tungsten (WC) and darker areas to cobalt (Co).

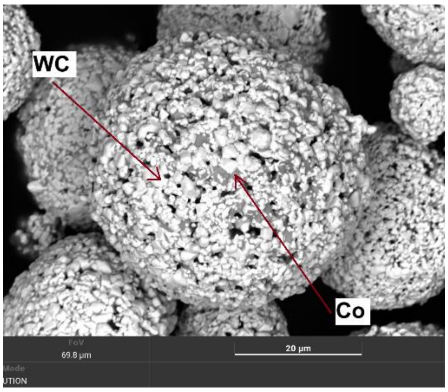

Fig. 2. SEM pictures morphology of WC-12Co powder.

Fig. 3 shows images of the initial WC-12Co powders. The sphericity of the powder indicates its good flowability. Different powder particle size distributions can significantly affect the different physical properties of thermal spray coatings, they can cause non-uniform material distribution which leads to void formation and inhomogeneous geometry of sprayed coatings [17, 18]. Therefore, it is important to select powder raw materials with appropriate particle size distribution when using different thermal spraying processes and process parameters.

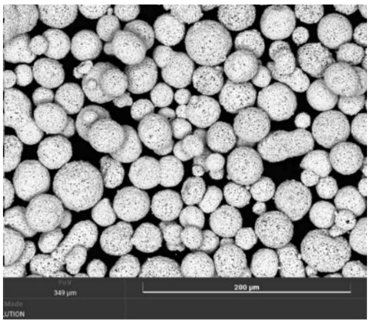

Fig. 3. SEM pictures of-12Co powders before sieving.

In order to ensure reliable and stable comparability of the characteristics of coatings in this study used powder size 5-50 micrometers, which was sieved into three fractions: 0-20 µm, 30-40 µm and 40-50 µm (Fig. 3, 4, 5) all images are made at a field of view equal to 349 µm. This allowed us to conduct comparative studies and evaluate the influence of fractional composition on the properties of coatings obtained by HVOF method.

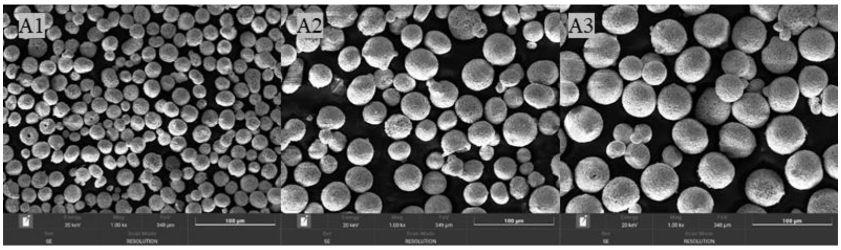

Fig. 4. SEM pictures of powder after sieving.

Fig. 5, 6 and 7 show the surface morphology of the WC-12Co coatings obtained by the HVOF method. The coatings show the presence of both fully melted and partially melted regions, with a small number of fragmented particles.

WC-based ceramic spraying powders have high melting temperatures of about 3000°C. In the HVOF spraying process, most of the metal powder is heated to a temperature close to the melting point [19]. The molten droplets impact the substrate surface at extremely high speed, solidify and are deposited layer by layer to form a dense and cohesive coating.

Fig. 6, 7, 8 also show that the number of unmelted particles decreases significantly with decreasing powder fraction. This contributes to the formation of denser and more homogeneous coatings.

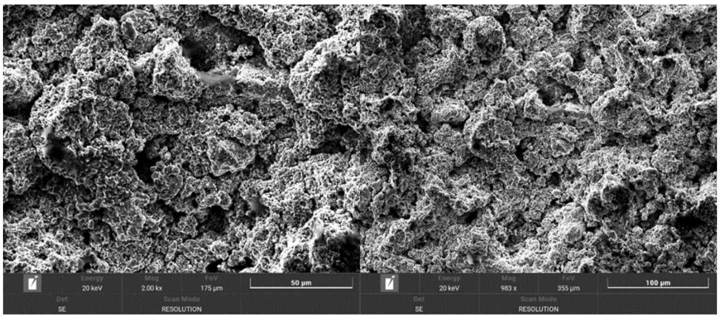

Fig. 5. SEM pictures of WC-12Co coating fraction 0-20 µm.

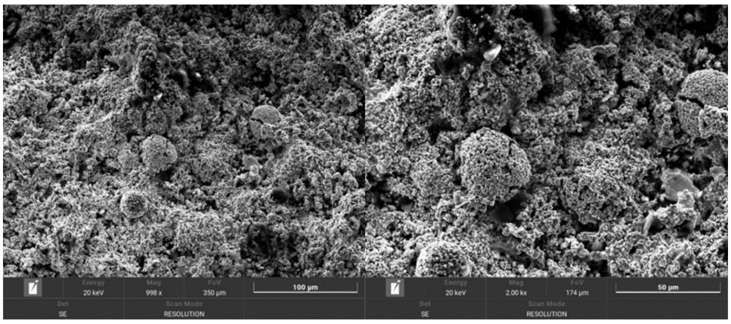

Fig. 6. SEM pictures of WC WC-12Co coating 30-40 μm fraction.

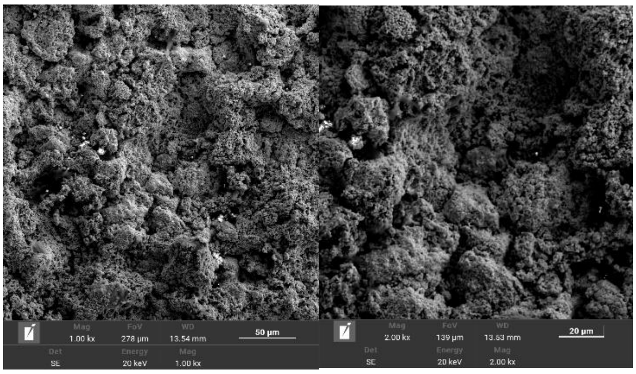

Fig. 7. SEM pictures of WC WC-Co coating 40-50 μm fraction.

The thickness of WC-12Co coatings varies from 700 to 850 μm. The coatings have a rather highly compact structure, which is characteristic of this powder. The indenter prints in hardness measurements show cracks, indicating that the coatings are highly porous.

Comparative analysis showed that the coatings obtained from powder fractions of 40-50 μm and 30-40 μm were more porous than coatings from powder fractions of 0-20 μm. This is probably due to the smaller particle size in the latter case, which contributes to better density and lower porosity of the coating.

3.2 Microhardness

Fig. 8 shows the results of studies of microhardness distribution of coatings obtained by HVOF method with different powder fraction. The studies showed the following results: The microhardness of stainless steel is 2-3 times less than that of coatings applied by HVOF method. The microhardness near the interface between the coating and substrate increased slightly to about 350 HV. This indicates that the exposure during powder particle deposition had some hardening effect on the substrate. The microhardness of the coatings deposited by the HVOF method ranged from 350 to 890 HV. Fig. 9 shows the SEM morphology of the cross section of coatings of different fractions with indenter imprints. As can be seen from the images, coatings with large pores did not crack under loading, however, coatings with small pores developed cracks at the loading points. Fig. 10 also shows the microhardness distribution graph.

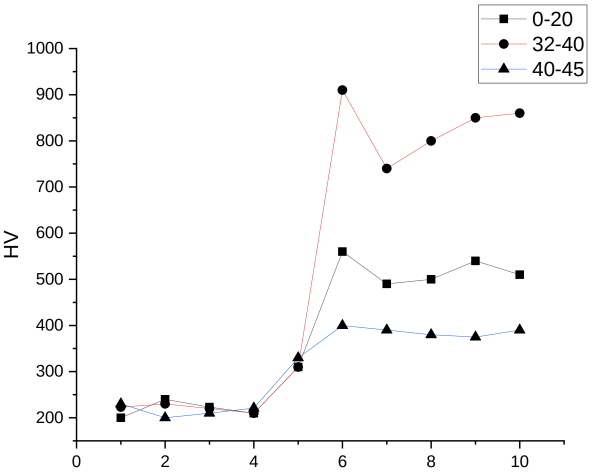

Fig. 8. Microhardness of samples.

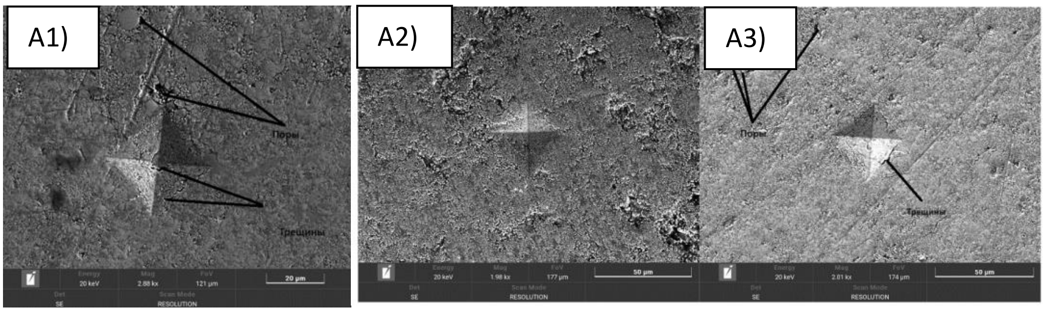

Fig. 9. Images of prints of the coating microhardness study (A1) 0-20 (A3) 40-50 (A2) 30-40.

You can see from the charts that:

- for the powder fraction 0-20 µm, the microhardness varied between 400-500 HV.

- for the powder fraction of 30-40 µm the microhardness was 290-340 HV.

- The optimum coating hardness was achieved at a powder fraction of 40-50 µm, where the microhardness varied between 700-890 HV.

These results emphasize the importance of powder fraction selection to achieve the desired coating performance.

3.3 Tribology

In the section concerning the tribological studies (Fig. 11), it was found that by varying the fractions of the initial powder, the average coefficient of friction of the coatings had the following values:

- µ = 0.552 for 0-20 µm fraction
- µ = 0.516 for 30-40 µm fraction
- µ = 0.510 for 40-50 µm fraction

Thus, the coefficient of friction does not change significantly with changing the powder fraction. However, it was observed that the maximum wear resistance was characteristic of the coating deposited with powder with 30-40 µm fraction (v = 2.789E-005). This is attributed to the increase in the content of WC carbide phase in the coatings [14]. Nevertheless, the difference in wear volume between coatings with fractions of 0-20 µm and 30-40 µm was not noticeable.

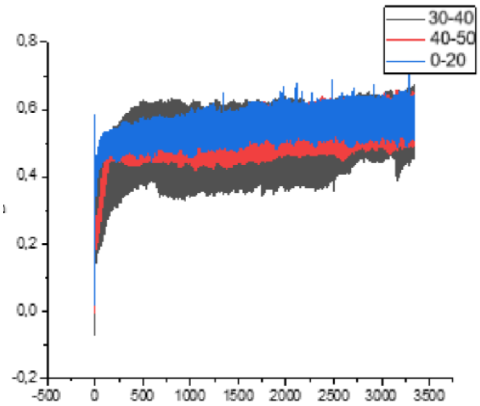

Fig. 10. The microhardness distribution graph.

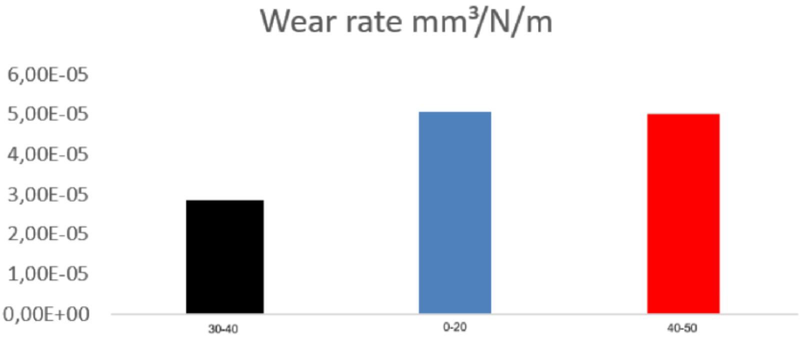

Fig. 11. Graph of friction coefficient versus friction path (a) and wear volume versus initial powder fractions (b).

4 Conclusion

In conclusion, the study demonstrates the significant impact of powder particle size on the microstructure, mechanical properties, and wear resistance of WC-12Co coatings produced by high-velocity oxygen-fuel (HVOF) spraying. Coatings produced from finer powder fractions (0-20 µm) exhibited superior characteristics, including lower porosity, higher density, and enhanced hardness, with values reaching up to 890 HV for the 40-50 µm fraction. The tribological tests revealed that the 40-50 µm fraction had the highest wear resistance, emphasizing the role of powder size in achieving optimal coating performance. These findings highlight the critical importance of selecting the appropriate powder fraction to improve the coating's performance, making WC-12Co coatings ideal for applications requiring high durability, such as in the aerospace and petroleum industries. The study underscores the effectiveness of HVOF spraying in producing coatings with high wear resistance and mechanical strength, contributing to the extension of the service life of components in harsh operating environments.

Funding

This research has been/was/is funded by the Science Committee of the Ministry of Science and Higher Education of the Republic of Kazakhstan (Grant No. BR24992864).

Conflict of interest

The authors declare no conflict of interest.

References

1 Caltaru, M.; Badicioiu, M.; Ripeanu, R.G. Establishing the Tribological Behaviour of HVOF Hardfacing Applied at Petroleum Gate Valves. *Journal of the Balkan Tribological Association* 2013, *19*, 448-460

2 Kengesbekov, A.B.; Rakhadilov, B.K.; Tyurin, Y.N.; Magazov, N.M.; Kylyshkanov, M.K.; Sagdoldina, Z.B. The Influence of Pulse-Plasma Treatment on the Phase Composition and Hardness of Fe-TiB 2 -CrB 2 Coatings. Eurasian Journal of Physics and Functional Materials 2021, 5, 155-162, doi:10.32523/ejpfm.2021050209

3 Rakhadilov, B.; Magazov, N.; Kakimzhanov, D.; Apsezhanova, A.; Molbossynov, Y.; Kengesbekov, A. Influence of Spraying Process Parameters on the Characteristics of Steel Coatings Produced by Arc Spraying Method. Coatings 2024, 14, 1145, doi:10.3390/coatings14091145

4 Katranidis, V.; Gu, S.; Allcock, B.; Kamnis, S. Experimental Study of High Velocity Oxy-Fuel Sprayed WC-17Co Coatings Applied on Complex Geometries. Part A: Influence of Kinematic Spray Parameters on Thickness, Porosity, Residual Stresses and Microhardness. *Surface and Coatings Technology* 2017, *311*, 206-215, doi:10.1016/j.surfco at.2017.01.015

5 Rakhadilov, B.; Muktanova, N.; Kakimzhanov, D.; Satbayeva, Z.; Kassenova, L.; Magazov, N. Investigation of the Influence of Powder Fraction on Tribological and Corrosion Characteristics of 86WC-10Co-4Cr Coating Obtained by HVOF Method. Coatings 2024, 14, 651. https://doi.org/10.3390/coatings14060651

6 Dejun, K., & Tianyuan, S. (2017). Wear behaviors of HVOF sprayed WC-12Co coatings by laser remelting under lubricated condition. *Optics and Laser Technology*, 89, 86-91. https://doi.org/10.1016/J.OPTLASTEC.2016.09.043

7 Baumann, I., Hagen, L., Tillmann, W., Hollingsworth, P., Stangier, D., Schmidtmann, G., Tolan, M., Paulus, M., & Sternemann, C. (2021). Process characteristics, particle behavior and coating properties during HVOF spraying of conventional, fine and nanostructured WC-12Co powders. *Surface & Coatings Technology*, 405, 126716. https://doi.org/10.1016/j.surfcoat.2020.126716

8 Al-Hamed, A., Benyounis, K., Al-Fadhli, H., Yilbas, B., Hashmi, M., & Stokes, J. (2016). Enhancement of conventional WC-Co and Inconel 625 HVOF thermal spray coatings by the addition of nanostructured WC-Co for wear/corrosion applications in the oil/gas industry. *Advances in Materials and Processing Technologies*, 2, 102 - 93. https://doi.org/10.1080/2374068X.2016.1159039

9 Vuoristo, P. 4.10 - Thermal Spray Coating Processes. In *Comprehensive Materials Processing*; Hashmi, S., Batalha, G.F., Van Tyne, C.J., Yilbas, B., Eds.; Elsevier: Oxford, 2014; pp. 229-276 ISBN 978-0-08-096533-8.

10 Vuoristo, P.M. High Velocity Sprays Boost Hardmetal Industrial Coatings. *Metal Powder Report* 2007, *62*, 22-29, doi:10.1016/S0026-0657(07)70063-2

11 Behera, N.; Medabalimi, S.R.; Ramesh, M.R.. Elevated Temperatures Erosion Wear Behavior of HVOF Sprayed WC-Co-Cr/Mo Coatings on Ti6Al4V Substrate. *Surface and Coatings Technology* 2023, *470*, 129809, doi:10.1016/j.surfcoat.2023.129809

12 Eßler, J.; Woelk, D.; Utu, D.; Marginean, G. Influence of the Powder Feed Rate on the Properties of HVOF Sprayed WC-Based Cermet Coatings. *Materials Today: Proceedings* 2023, *78*, 227-234, doi:10.1016/j.matpr.2022.11.120

13 Javed, M.A.; Ang, A.S.M.; Bhadra, C.M.; Piola, R.; Neil, W.C.; Berndt, C.C.; Leigh, M.; Howse, H.; Wade, S.A.. Corrosion and Mechanical Performance of HVOF WC-Based Coatings with Alloyed Nickel Binder for Use in Marine Hydraulic Applications. *Surface and Coatings Technology* 2021, *418*, 127239, doi:10.1016/j.surfcoat. 2021.127239

14 Wei, Z.; Cui, D.; Wei, Z.; Hong, S. Effect of Sulphide Concentration on Corrosion Behaviors of HVOF-Sprayed WC-Cr3C2-Ni and WC-Ni Coatings. *International Journal of Refractory Metals and Hard Materials* 2023, *111*, 106104, doi:10.1016/j.ijrmhm.2023.106104

15 Wu, D.; Cheng, Q.; Yu, Q.; Guan, Z.; Deng, Y.; Liu, Y. Influence of High Hydrostatic Pressure on Tribocorrosion Behavior of HVOF WC-10Co-4Cr Coating Coupled with Si3N4 in Artificial Seawater. *International Journal of Refractory Metals and Hard Materials* 2022, *108*, 105936, doi:10.1016/j.ijrmhm.2022.105936

16 Yu, H., Guo, R., Xia, H., Yan, F., & Zhang, Y. (2013). Study on the Effect of WC Size on the Thermal Expansion Coefficient of WC/Cu Composites. *Applied Mechanics and Materials*, 275-277, 1597 - 1600. https://doi.org/10.4028/www.scientific.net/AMM.275-277.1597

17 Brennan, D., Bacha, T., Tiitma, Ü., Haas, F., & Stanzione, J. (2022). Systematic Study of the Effects of Powder Preconditioning on Flowability and Deposition in Polymer Cold Spray. *International Thermal Spray Conference*. https://doi.org/10.31399/asm.cp.itsc2022p0683

18 Rakhadilov, B.; Muktanova, N.; Kakimzhanov, D.; Satbayeva, Z.; Kassenova, L.; Magazov, N. Investigation of the Influence of Powder Fraction on Tribological and Corrosion Characteristics of 86WC-10Co-4Cr Coating Obtained by HVOF Method. Coatings 2024, 14, doi:10.3390/coatings14060651

19 M., Jalali, Azizpour., Majid, Tolouei-Rad. (2019). The effect of spraying temperature on the corrosion and wear behavior of HVOF thermal sprayed WC-Co coatings. Ceramics International, 45(11):13934-13941. doi: 10.1016/J.CERAMINT.2019.04.091

20 U., Langklotz., Filofteia-Laura, Toma., Anja, Meyer. "Electrochemical Investigations and Corrosion Behavior of HVOF WC-12Co Coatings Obtained from Powder and Aqueous Suspension." Thermal spray, null 2023. doi: 10.31399/asm.cp.itsc2023p0695

AUTHORS’ INFORMATION

Kussainov A.E. - Researcher of Protective and Functional Coatings Scientific Center, D. Serikbayev East Kazakhstan Technical University; Institute of Composite Materials LLP, Ust-Kamenogorsk, Kazakhstan; SCOPUS Author ID: 59515031200. (e-mail: arys20055@gmail.com)
Magazov N.M. - Researcher of Protective and Functional Coatings Scientific Center, D. Serikbayev East Kazakhstan Technical University, Ust-Kamenogorsk, Kazakhstan; SCOPUS Author ID: 57220041350. (e-mail: magazovn@gmail.com)
Abizhanova I.K. - Researcher of Protective and Functional Coatings Scientific Center, D. Serikbayev East Kazakhstan Technical University, Ust-Kamenogorsk, Kazakhstan; *ORCID iD*:. 0009-0006-3218-7246 (e-mail: iabizhanova@gmail.com)
Kuanyshbai R.M. - Researcher of Protective and Functional Coatings Scientific Center, D. Serikbayev East Kazakhstan Technical University, Ust-Kamenogorsk, Kazakhstan; (e-mail: rashidmaratly08@gmail.com)